8-2014

Development and Implementation of an Anthropomorphic Pediatric Spine Phantom for the Assessment of Craniospinal Irradiation Procedures in Proton Therapy

Dana Lewis

DEVELOPMENT AND IMPLEMENTATION OF AN ANTHROPOMORPHIC PEDIATRIC SPINE PHANTOM FOR THE ASSESSMENT OF CRANIOSPINAL IRRADIATION PROCEDURES IN PROTON THERAPY

By

Dana Jannette Lewis, B.S.

APPROVED:

_____

Supervisory Professor – Stephen Kry, Ph.D.

_____

David Followill, Ph.D.

_____

Narayan Sahoo, Ph.D.

_____

Anita Mahajan, M.D.

_____

Francesco Stingo, Ph.D.

_____

Paige Summers, M.S.

(All signatures must be in black ink.)

_____

APPROVED:

_____

Dean, The University of Texas

Graduate School of Biomedical Sciences at Houston

DEVELOPMENT AND IMPLEMENTATION OF AN ANTHROPOMORPHIC PEDIATRIC SPINE PHANTOM FOR THE ASSESSMENT OF CRANIOSPINAL IRRADIATION PROCEDURES IN PROTON THERAPY

A

THESIS

Presented to the Faculty of
The University of Texas
Health Science Center at Houston
And
The University of Texas
M.D. Anderson Cancer Center
Graduate School of Biomedical Sciences
in Partial Fulfillment

of the Requirements

for the Degree of

MASTER OF SCIENCE

by

Dana Jannette Lewis, B.S.
Houston, TX

August 2014

Dedication

To my medical physics mentor,

Without your introduction into this field, I would have not found a career that I love. Thank you for wholeheartedly supporting me and providing your wisdom to help me reach my goals. I am eternally grateful to you and I hope I've made you proud.

Acknowledgements

I would like to thank and acknowledge my Advisory Committee: Stephen Kry, PhD., Paige Summers, M.S, David Followill, PhD., Narayan Sahoo, PhD., Anita Mahajan, M.D., and Francesco Stingo, PhD., for all of their insight and support during this project.

Additionally, I would like to thank John Costales for constructing my phantom; Michael Gillin, PhD., Xiaodong Zhang, PhD., Brad Taylor, Matt Kerr and Charles Holmes for assistance with the treatment delivery; David Lege, for his expertise in proton treatment planning; and the PTC-H radiation therapists for their assistance with imaging the phantom.

I also would like to thank Jessie Huang, Austin Faught, Jacqueline Tonigan and the IROC Houston staff for their help with the phantom analysis.

Lastly, I would like to thank my family and friends for their kind words of support and encouragement through the duration of this project.

Development and Implementation of an Anthropomorphic Pediatric Spine Phantom for the Assessment of Craniospinal Irradiation Procedures in Proton Therapy

Dana Jannette Lewis, B.S.

Supervisory Professor: Stephen F. Kry, Ph.D.

Proton therapy is gaining acceptance as a cancer treatment modality, as it allows for dose deposition to the target volume while sparing the surrounding healthy tissue. This technique is advantageous for craniospinal pediatric patients, as it reduces the radiation side effects that can occur. The purpose of this study is to design an anthropomorphic pediatric spine phantom for use in the evaluation of proton therapy facilities for clinical trial participation by the Imaging and Radiation Oncology Core (IROC) Houston QA Center. It was hypothesized that the designed phantom would evaluate patient simulation, treatment planning and delivery, assuring agreement between the measured and calculated doses within 5%/3mm, with 85% of pixels passing criteria for gamma analysis and also a TLD point dose agreement within 5%. Tissue equivalency was determined by measuring the relative stopping power and Hounsfield unit of potential phantom materials. The materials selected as bone, tissue, and cartilage substitutes were Techron HPV Bearing Grade (RSP 1.3, HU 595.6), solid water (RSP 1.004, HU 16), and blue water (RSP 1.07, HU 86), respectively. The design also incorporates two thermoluminescent dosimeter (TLD)-100 capsules and radiochromic film embedded for dose evaluation. CT images of the phantom were acquired and used to create passive scattering and spot scanning treatment plans. Each plan was delivered three times at a dose of 6 Gy. The following attributes were evaluated: absolute dose agreement, distal range, field width, junction match and right/left dose profile alignment. The hypothesis was accepted for the passive scattering plans, making this phantom and delivery technique suitable for use in IROC Houston proton approval process.

Table of Contents

List of Tables and Illustrations

Abbreviations

CERR: Computation Environment for Radiotherapy Research, 38

CGE: Cobalt Gray Equivalent, 8

CSI: craniospinal, 4

CT: computed tomography, 4

DRRs: digitally reconstructed radiographs, 23

DTA: Distance to agreement, 39

HU: Hounsfield unit, 14

ICRU: International Commission on Radiation Units and Measurements, 1

IMPT: Intensity Modulated Proton Therapy, 11

IMRT: Intensity Modulated Radiation Therapy, 2

IROC-H: Imaging and Radiation Oncology Core Houston QA Center, 1

LET: linear energy transfer, 54

MU: monitor unit, 4

MRI: magnetic resonance imaging, 76

NIST: National Institute of Standards and Technology, 16

NCI: National Cancer Institute, 1

PDD: percentage depth-dose, 6

PTC-H: (U.T.M.D. Anderson) Proton Therapy Center-Houston, 9

QA: quality assurance, 1

RBE: relative biological effectiveness, 8

RPC: Radiological Physics Center, 1

RSP: relative stopping power, 16

SAD: source-to axis-distance, 35

SOBP: spread-out Bragg Peak, 6

TLD: thermoluminescent dosimeter, 5

TPS: treatment planning system, 16

Chapter 1

1 Introduction and Background

1.1 Statement of Problem

1.1.1 General Problem Area

As proton therapy becomes a more widely used modality for cancer treatment, it is important to ensure that treatments at institutions across the country are consistent and comparable. For National Cancer Institute (NCI) funded clinical trials using radiation therapy, a large number of institutions are required to participate and enroll patients in order to accrue sufficient numbers of patients to meet the statistical requirements of the study. Therefore, an independent quality assurance (QA) program is required to assure that the prescribed radiation doses delivered at multiple institutions are clinically equivalent and reliable. Even though proton-beam therapy facilities may already have their own comprehensive quality assurance program in place based on accelerator type, delivery techniques, and recommendations from the International Commission on Radiation Units and Measurements (ICRU)[1], a QA program that ensures comparability from one facility to the next is still needed. The differences in procedures and technologies at each facility can cause challenges in determining the consistency in dose delivered to patients treated at various facilities [2]. Currently, there are very few organizations that are active in the correlation and assessment of QA procedures, along with credentialing across institutions involved in clinical trials using radiation therapy [2].

The Imaging and Radiation Oncology Core Houston QA Center (IROC-H), formerly known as the Radiological Physics Center (RPC), is a QA group housed at MD Anderson Cancer Center in Houston, TX, funded by NCI for the purpose of auditing and credentialing institutions for clinical trial participation [3]. This responsibility includes the assessment of institutional radiation therapy programs to ensure not only that the administered doses and

results from the clinical trial can be reliably interpreted, but also that dose uncertainty is minimized. To achieve this, IROC Houston conducts remote audits of machine outputs, reviews of patient treatment records, on-site dosimetry reviews and credentialing of institutions using anthropomorphic QA phantoms [3]. These anthropomorphic phantoms are used in the remote audit mailable program to verify dose delivery for a variety of advanced technology treatment techniques. The data received is analyzed and used to assist the institution in identifying discrepancies in the beam modeling of their treatment planning system, dose calculation and/or delivery, and to implement resolutions. IROC Houston monitors all conventional radiation therapies and has numerous phantoms for photon and electron therapies, such as the stereotactic radiosurgery head, spine, thorax/lung, pelvic/prostate, intensity-modulated radiation therapy (IMRT) head-and-neck, and liver phantoms [4-6]. In addition to the photon phantoms, there are also a family of phantoms for evaluating proton therapies, such as the prostate, head, spine, and lung phantoms [7, 8]. In an effort to make these anthropomorphic proton phantoms more “proton equivalent” in terms of the tissue simulating plastics, the proton spine phantom was found to have deteriorated significantly over the years such that the bone within was more like air cavities rather than bony material. Because of these issues with the proton spine phantom, a solution had to be found that addressed the problems.

1.1.2 Specific Problem Area

Radiation therapy and the techniques used for controlling cancer have continued to expand over the years. Conditions such as prostate, lung, head and neck, and pediatric cancers are not only a treated with conventional radiation therapies, but also with proton therapy. Facilities nationwide are showing interest in updating their radiation oncology practices to include the use of protons. According to the National Association for Proton Therapy, there are 16 proton centers in operation, 8 centers under construction and 12 centers currently being developed in the United Sates [9]. Therefore, there is an increased need for the evaluation of

the radiation treatments delivered to patients using this form of therapy, especially if the institution wants to be considered for participation in a cooperative study group-sponsored trial.

Currently, IROC Houston has a proton approval process, as mandated by NCI guidelines, that institutions must successfully complete before being allowed to enroll patients in a clinical trial [10]. This process entails completion of a proton facility questionnaire, annual irradiation of dosimeters for verification of proton beam calibrations, verification of the ability to transfer patient treatment plans electronically, irradiation of 2 baseline anthropomorphic proton phantoms (prostate and spine), and completion of an on-site review at least 6-months after routine treatments begin [10]. At this time, IROC Houston has a proton spine phantom that is sent to institutions for irradiation. However, the current physical state of the phantom has caused problems with the analysis. The skeleton inside the phantom is deteriorating, causing air pockets that can lead to inaccurate irradiation conditions associated with matching spine irradiation fields. The design of the current spine phantom also causes curvature of the film when positioned, causing additional difficulties in the dosimetry analysis since the film fell outside of the primary treatment planes (sagittal, coronal and axial). Additionally, the vertebral bodies are much larger compared to a typical pediatric patient. Therefore, the goal of this project is to design a new more realistic anthropomorphic pediatric proton spine phantom based on materials that are tissue equivalent in a proton beam while incorporating the spinal curvature in a manner that does not affect the film dosimetry. This new anthropomorphic spine phantom will benefit proton therapy as an independent auditing and credentialing tool. With institutions proving their ability to successfully irradiate this phantom, it suggests that treatment deliveries to the patient will also be successful.

1.1.3 Importance of Topic

One of the most common cancers in pediatric patients is medulloblastoma, a brain tumor that is known to metastasize through cerebrospinal fluid pathways. While there has been increased survival in patients with this disease, there is still a concern regarding the side effects associated with craniospinal (CSI) treatments [11]. Beam delivery studies comparing CSI treatments have shown that proton beams deliver a more conformal dose to the target compared to photon beams [12]. This advantage does not come without uncertainties in the treatment process, hence the need for QA procedures and approval processes for clinical trials.

Quality assurance programs are designed to verify that the dosimetry conditions determined during beam commissioning have not deviated from their baseline values thus ensuring that the dose prescription and delivery is fulfilled as intended, while minimizing personnel exposure and dose to normal tissue[13]. Recommendations from ICRU 78 for proton QA procedures include daily, weekly and annual/scheduled inspection checks for both passive and scanning beam-delivery systems [1]. Checks for scattered beam-delivery systems include aperture alignment, range, entrance dose, uniformity of range modulation and Bragg-peak width, dose monitor calibration according to TRS-398 protocol, checks of monitor unit (MU) values, beam-line apparatus, computed tomography (CT) Hounsfield number calibration and comprehensive tests of therapy equipment [1]. Additional checks for scanning beam-delivery systems include dose rate and monitor ratios for the pencil beam, depth-dose curve of a pencil beam in a water phantom and checks of the beam characteristics [1]. For multi-institutional clinical trials, one of the key issues is that the QA program vary between proton-beam facilities due to differences in the proton accelerator and beam-delivery techniques. This variation, along with the implementation of new technology, increases the possibility for error in treatments and variability in patient dose delivery between proton facilities if QA checks are not conducted appropriately.

Quality assurance has always been an important aspect in radiation therapy, but media attention has shined a negative light on the field due to radiation therapy accidents. An article in the New York Times in 2010, while exposing a fatal treatment error, reported on the RPC's ability to uncover mistakes that can ultimately affect the treatment delivery [14]. With more proton facilities being constructed, the mission of IROC Houston has become increasingly more important. IROC Houston provides an independent measurement and evaluation of treatment planning and delivery as a second check to internal on-site measurements. This independent end to end QA measurement can be completed using an anthropomorphic QA phantom designed specifically for proton therapy.

1.2 Hypothesis

An anthropomorphic pediatric spine phantom can be designed to evaluate craniospinal proton therapy procedures (patient simulation, treatment planning, and treatment delivery) to assure agreement between the measured and calculated doses within ±5%/3mm, with ≥85% of pixels passing criteria for gamma analysis and a thermoluminescent dosimeter (TLD) point dose agreement within ±5%. To test hypothesis, the following specific aims were developed for this project:

1. Create a suitable spine phantom design based on patient characteristics and appropriate proton tissue equivalent materials for corresponding relevant patient anatomy.
2. Image the spine phantom and create clinically relevant treatment plans for both passive scattered and spot scanned proton beams. After the treatment plans are created, irradiate the phantom using these treatment plans.
3. Measure the delivered dose distributions and dose to designated points in the irradiated phantom.

4. Compare the measured doses and 2D dose distributions to those calculated by the treatment planning system to determine the agreement and/or variability.

1.3 Proton therapy

1.3.1 Background Information on Protons

The advantages of using protons for medical purposes were first shown by Robert Wilson in 1946. Wilson published the idea of using the energy deposition at the end of the proton range, called the Bragg peak, for treating cancer [15]. The Bragg peak, as shown in figure 1.1, is a feature on the proton depth dose curve, which plots the specific ionization of protons, consequently dose, as they penetrate through depths in tissue. The ionization density is relatively low at the surface and also throughout the depth of penetration. However, there is a narrow region where the ionization density increases before sharply decreasing, leaving negligible dose deposited beyond this region [16]. Other characteristics that give rationale for using protons for radiation therapy include: the ability to manipulate the proton range in objects based on the density of a material and the energy of the beam, and achieving a more conformal dose to the target, leading to reduced tissue complications and increased tumor control compared to other conventional therapies [16, 17]. Wilson also introduced the concept of using a modulator wheel of varying thickness between the source and the patient to widen the region of high ionization density, which is now defined as the spread out Bragg peak (SOBP) [15]. This flat dose region still has a rapid fall off in dose beyond the proton range, but the SOBP allows for full coverage of larger targets. Both the Bragg peak and the SOBP in comparison with photon and electron percentage depth-dose (PDD) curves are shown in Figure 1.1.

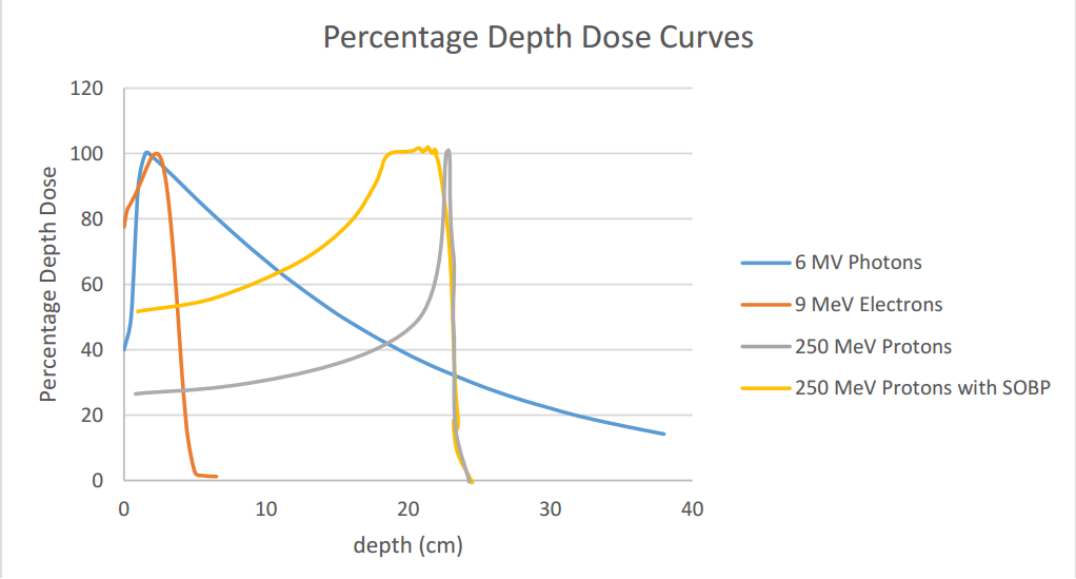

Figure 1.1: Percentage depth dose curves for 6MV photons, 9 MeV Electrons, 160 MeV protons with a pristine Bragg Peak, and 160 MeV protons with a spread out Bragg Peak

Protons mostly interact through collisions with atomic electrons in a medium as they lose energy. The density of the material and the proton beam energy determine the stopping power. The proton mass stopping power describes the amount of energy lost in each interaction and is defined as [18]:

$$\frac{S(E)}{\rho} = \frac{1}{\rho}\frac{dE}{dx}, \qquad \textbf{Equation 1.1}$$

where S is the linear stopping power which is a function of the energy, dE is the mean energy lost as the proton transverses a medium over a distance dx with a known density ρ. The range of the proton can be determined from the linear stopping power and is defined as [18]:

$$R = \int S(E)^{-1}\, dE. \qquad \textbf{Equation 1.2}$$

In the stopping interaction, as more momentum is transferred to the electron, the proton stays in its vicinity as it loses energy and deposits dose. Therefore, the proton range is proportional to the square of the velocity and the stopping power is inversely proportional to the square of the proton's velocity [17].

1.3.2 Radiation Biology of Protons

Protons and other heavy charged particles show an increased biological effect compared to photons and electrons which can be described by the relative biological effectiveness (RBE). The RBE is defined as:

$$RBE = \frac{Dose_{reference\ radiation}}{Dose_{test\ radiation}}. \qquad \textbf{Equation 1.3}$$

Equation 1.3 shows the doses needed between a reference radiation, such as 250 kVp x-rays or ^{60}Co photons, and a test radiation, to achieve the same biological effect. Experimental data is consistent with an RBE of 1.1 for protons [19]. When the RBE is greater than 1, an increase in the amount of biological damage to tumors is observed compared photons and electrons that have an RBE of 1.

To account for the RBE, the weighted proton dose is expressed as Cobalt Gray Equivalent (CGE) and is defined as [19]:

$$D_{RBE} = D \times 1.1, \qquad \textbf{Equation 1.4}$$

where D_{RBE} represents the RBE-weighted absorbed proton dose and D represents the proton absorbed dose. According to NCI guidelines, institutions participating in clinical trials must report dose prescriptions in units of CGE [10].

1.3.3 Proton Therapy Beam Delivery Methods

1.3.3.1 Proton Accelerators

One of the main components of a proton facility is the accelerator used to create the proton beams. There are 2 kinds of proton accelerators: cyclotrons and synchrotrons. Cyclotrons accelerate particles from a hydrogen source through the gap between pole pieces of a large magnet with a fixed magnetic field and a fixed radiofrequency [18]. Classical cyclotrons would only accelerate protons up to 10-15 MeV, due to the relativistic increase in the proton mass causing problems in accelerating past this energy. Isochronous cyclotrons compensate for the relativistic increase by increasing the magnetic field as the radius increases to maintain resonance, allowing for protons to be accelerated to a therapeutic energy of 230 MeV [18]. Because cyclotrons output a fixed energy beam, the range of the beam is shifted by placing absorbers or modulation wheels in the beam path[16].

The MD Anderson Cancer Center Proton Therapy Center-Houston (PTC-H) uses a synchrotron to create the proton beam lines. Synchrotrons accelerate low energy protons that are injected into a ring of magnets. These magnets have a fixed radius, allowing the path of the protons to repeatedly travel the same path while the magnetic field increases to keep a fixed orbit. Unlike cyclotrons, energy variation of the beam can be achieved in addition to range shifting [18]. Relevant parameters for choosing an accelerator include the needed speed of the energy change, the accuracy of the obtained energy (range), and beam intensity, energy spread and beam broadening [17].

1.3.3.2 Passive Scattering

Passive scattering is a method of beam delivery used to spread out near-monoenergetic protons and create dose distributions for targets. To create a uniform distribution, the primary beam is spread laterally using a scattering foil, then degraded to the

appropriate energy using a range modulation wheel and possibly an energy absorber, and laterally conformity to a target is achieved using apertures and compensators. Beams must be double scattered to adequately achieve beam flatness, since a single scattered beam only has appropriate flatness in the center of the distribution [17].

An aperture is a patient-specific device made of brass or cerrobend to shape the beam in the lateral direction and stop protons that lie outside the shape of the target. Additional margins accounting for setup uncertainties and penumbra are also included in its shape. A compensator is placed after the aperture to shape the beam distally by removing variation in depth due to the lateral positioning [17]. To create the compensator, the water equivalent depth at the distal surface is determined and used to determine the range at the deepest point. difference between the deepest point and the respective location is used to determine the compensator thickness at that location. If the depth is large, a small amount of material is added and if the depth is small, a larger amount of material is added to the compensator. The correct amount of compensation is achieved only if there is no misalignment between the compensator and the target [17]. Therefore, smearing, or incorporating a margin to account for compensator misalignment or changes in patient anatomy, must be added to ensure target coverage.

1.3.3.2 Spot Scanning

A second delivery method is spot scanning, where pencil beams are applied in discrete steps at various positions to create a uniform dose distribution over the target [18]. A proton source is applied in a certain position before the beam is terminated and steered to a different location and resumed. While steering the beam, the energy and the depth of penetration are changed so that a uniform dose is delivered. Spots are appropriately spaced to avoid non-uniformity. Unlike passive scattering, patient-specific devices, such as apertures and

compensators are not typically used. Advantages of spot scanning over passive scattering include achieving more dose conformity to the PTV, a reduction in the secondary neutron dose and the ability to use intensity modulated proton therapy (IMPT).

1.3.4 Dose Uncertainties in Proton Therapy

Errors and fluctuations can occur in many steps of treatment that lead to uncertainties in the dose delivery. These uncertainties arise from errors in tumor identification, staging, spatial extent, immobilization, dose distribution, assessment methods, dose calculation algorithms, and other treatment parameters [20]. Uncertainties in the proton range are of particular importance because an incorrect estimate in range translates to inaccurate dose delivery, resulting in an under dose of the target or overdose to the adjacent normal tissue. Range straggling, or an energy spread at the stopping location, is produced by both the patient and the energy absorbers. This can decrease the sharpness of the distal fall off of the proton depth dose curve. To account for variations, the treatments at PTC-H incorporate a range uncertainty of 3.5% of the proton beam range plus an additional 3mm [21]. The additional margin of 3mm is added to further account for uncertainties in the distal fall off gradient. With many opportunities for a mistake, the need for comprehensive QA programs and additional audits is apparent.

1.3.5 Beam Monitoring Devices

Subsystems to the main components of treatment delivery are contained in the nozzle. The nozzle, or treatment head, contains components through which the proton beam traverses before being delivered to the patient. This element in the treatment delivery monitors beam uniformity, alignment and other physical parameters of the treatment beam. There are many devices that intercept the beam as it passes through the nozzle, such as the beam profile and reference dose monitors that help control treatment delivery [22]. The beam also intercepts two ionization chambers that act as primary and secondary dose monitors to measure the number

of MUs delivered and terminate the beam after the prescription MU have been delivered. The snout is the part of the nozzle that is closest to the patient and holds the aperture and compensator. There are variations between the nozzle components used for passive scattering and spot scanning due to the difference in treatment delivery. However, both types of nozzles have essential components that are important for ensuring a safe treatment delivery. Other essential components in the passive scattering delivery system include: range modulation wheel combined with first scatter to create the SOBP, second scatterer, range shifter to finely degrade the range, and Faraday cup to measure the energy spectrum [18]. Essential components of the spot scanning delivery system include: scanning magnets in the x and y directions to steer the spot position, spot position monitor, and energy absorber to control the penetration of the beam if needed [18].

1.3.6 Proton Therapy in Craniospinal Treatments

As mentioned previously, pediatric CSI is used for treating patients with medulloblastoma. This treatment can be performed using conventional photon and electron radiation therapies, in addition to proton therapy. There is currently a debate in the radiation oncology community regarding how ethically appropriate proton CSI treatments are, as a balance between the clinical, geographical and financial conflicts of this treatment must be determined[23]. Research has shown proton CSI as superior to photon CSI after comparison of treatment plans and of dosimetric data for pediatric patients [11,12, 24]. Treatments using photon therapy have the potential to induce late effects as a consequence of out-of-field and/or exit dose being delivered to non-target organs such as the heart, lung, and cochlea. Late effects that can occur include impaired growth, hearing loss, neuropsychological dysfunction, cardiac diseases and secondary cancers [24]. The properties of protons allows the dose to the non-target organs to be significantly reduced. Because using protons for CSI is still novel, it will

take many years before published data confirms the proposed reduction in late effects and secondary cancer incidence compared to photon therapy [25].

Chapter 2

2 Methodology

2.1 Research Approach

The methodology that will be used to accomplish each specific aim is as follows:

1. The Hounsfield units and stopping power will be determined for phantom materials and compared to known values of corresponding human anatomy used for proton therapy.
2. Images of the phantom will be acquired and used to design one passive scattering treatment plan and one spot scanning treatment plan with the Eclipse proton planning system, according to MD Anderson's clinical practice. The development of the plans will be based on clinical constraints for CSI patients at the Proton Therapy Center-Houston (PTC-H) and a radiation oncologist will confirm that constraints have been met.
3. Radiochromic film and TLD will be placed inside the phantom and will be irradiated a minimum of three separate times according to the designed treatment plan.
4. The 2-D dose distributions and absolute point doses determined from the film and TLD measurements will be compared to the calculated points, dose profiles and dose distributions from the treatment planning system to determine the dose differences and agreement.

2.2 Phantom Design

2.2.1 Previous Phantom Design

IROC Houston has a variety of anthropomorphic phantoms used as dosimetric QA tools in the remote audit QA program. These phantoms consist of plastics that mimic biologic

tissues, or a plastic shell that is filled with water. All phantoms contain tissue inserts that mimic tumors and critical structures in both physical and anatomical compositions. Heterogeneous phantoms are an advantage when monitoring institutions, as they increase the level of difficulty of treatment planning and delivery while simulating a patient. IROC Houston currently has five phantoms used during the proton approval process or credentialing: an anthropomorphic head phantom, spine phantom, prostate phantom, liver phantom and thorax phantom [3].

The current proton spine phantom used by IROC Houston contains skeletal vertebrae cast in a muscle-equivalent material and is a tool for testing beam range verification, along with the institution's ability to properly match two proton fields at a junction [3, 26]. The main disadvantage to using actual vertebrae in anthropomorphic phantoms is that, over time, crevices and air pockets begin to form within the bone. Additionally, the vertebral bodies in the current spine phantom are much larger than pediatric vertebral bodies and are not appropriate to evaluate CSI treatments. Therefore, the new spine phantom design was developed to overcome these three existing problems: to contain 1) durable biologically equivalent materials that will not degrade over time 2) size-appropriate vertebrae for a pediatric patient, and 3) did not require bending of the film. These improvements removed the major factors that previously lead to difficulties in the use of and dosimetric assessment of proton CSI treatments at institutions.

2.2.2 Phantom Design Considerations

Materials that simulate tissue when placed in a photon beam may not simulate tissue when placed in a proton beam. Plastics that are considered photon equivalent are determined by the Hounsfield unit (HU) and electron density of the material. In proton therapy, a material's proton equivalency is determined based on the HU and proton stopping power. A material must fall within 5% of the HU-stopping power calibration curve of the treatment planning system [27].

Therefore, the phantom should be designed using materials that have been tested and confirmed to be accurately mimic a patient in a proton beam. These materials should be durable and not only remain intact over time, but also be easily transportable by mail to various institutions. Materials chosen should be discernable on a CT image to ensure accurate treatment planning. The phantom should be designed to include minimal air gap at the interfaces between the bone, cartilage and soft tissue substitutes to avoid introducing additional range uncertainty. The phantom should be designed to accommodate placement of both TLD and film for dosimetric measurements. The simulated spine curvature should be designed to avoid arching in the film. The dimensions of the phantom should be designed to accurately represent the spinal column of a pediatric patient and to accommodate the beam divergence when using a junction.

Clinically, CSI junctions are placed in the thoracic region of the spinal column during treatments when needed. Therefore, the thoracic region was selected for simulation in the phantom design. The design should incorporate 3 materials that simulate bone, cartilage and soft tissue. The inclusion of multiple tissue substitutes increases the treatment planning difficulty, resulting in a more realistic patient simulation. Institutions capable of planning and conducting a successful treatment using this heterogeneous spine phantom suggest to IROC Houston that the institution can appropriately deliver a proton CSI treatment that would require junction matching of the two proton fields.

2.1.3 Determination of Bone Equivalent Material

Because no suitable bone-equivalent material was known to IROC-Houston, potential bone substitutes were tested for bone-equivalency in a proton beam. The main characteristic considered when determining possible materials was density, as this parameter would largely affect the range of the proton beam during irradiations and the HU. The density of bone can

vary depending on its location and marrow content. Dense bone has a density of 1.85 g/cm^3, according to National Institute of Standards and Technology (NIST) [28]. The density of the bone in the vertebral column was reported as 1.33-1.42 g/cm^3 in a study by Schneider et. al [29]. Therefore, a range in density of approximately 1.3-1.8 g/cm^3 was used to compile a list of materials for testing. A total of 11 materials were tested as a potential bone substitutes and three of the materials were described as photon bone-equivalent by a manufacturer (Gammex, Inc., Middleton, WI). A list of tested materials and corresponding densities is shown in Table 2.1.

Material Name	Density (g/cm^3)
Gammex Inner Bone	1.12
Gammex Cortical Bone	1.82
Gammex B200 Bone	1.15
Boedeker Techron HPV Bearing Grade	1.43
Boedeker Ketron PEEK GF30	1.51
Boedeker Polyester PETP Ertalyte TX	1.44
Boedeker Ketron HPV Bearing Grade	1.44
Boedeker Polyester PETP Ertalyte	1.41
Boedeker Duratron T4301 PAI	1.45
Crayola Clay	0.11
Concrete block	1.78

Table 2.1: Composite list of materials tested for bone tissue substitutes

After obtaining the HU and relative stopping power (RSP) for each potential material, this data is plotted along the PTC-H calibration curve. As previously mentioned, to determine if a material is patient equivalent for proton therapy, the HU and RSP of a material are compared against the treatment planning system's (TPS) calibration curve. This bilinear calibration curve is created using a stoichiometric method, where the measured HU of animal tissues and tissue substitutes are used as predictors for the HU corresponding to human anatomy [29, 30].

A CT image of each material sample was acquired on the GE LightSpeed RT16 CT scanner (GE Healthcare, Waukesha, WI) at PTC-H using an scan protocol of 120 kVp, 120 mAs, 48cm diameter field of view and a slice thickness of 5mm [31]. The images were then

imported into the Eclipse TPS to determine the HU. The mean HU and standard deviation were calculated based on a series of 10 measurements from each sample. Next, depth dose curves with each material in the proton beam path were acquired on the fixed passive scatter beam line at PTC-H using a modified technique described in Moyers et. al [31]. Each material was placed in front of the Zebra multi-layer ionization chamber detector, (IBA, Schwarzenbruck, Germany) a device used to measure the depth dose curve. A reference curve was also completed without any material present in the beam. All scans were performed with an 18 x 18 cm field and a SOBP of 10cm to 50 MU. The data from the depth dose curves was used to calculate the RSP, described by:

$$RSP = \frac{R_{80,w} - R_{80,m}}{t_m} \qquad \textbf{Equation 2.1}$$

where $R_{80,\,w}$ represents the depth to the distal 80% dose without material present in the beam, $R_{80,\,m}$ represents the depth to the distal 80% dose with material present in the beam, and t_m represents the thickness of the material sample. The relative stopping power was calculated at energies of 160 MeV and 250 MeV. Because most craniospinal treatments use a 160 MeV beam, the stopping powers corresponding to this energy were used for determining proton equivalency. Results from Grant et. al were used to select the cartilage and soft tissue substitutes [27].

2.2.3.1 RSP Error Analysis

A total of 10 HU measurements were conducted and used to calculate the mean and standard deviation for each material to assess the uncertainty of the HU for each sample. The uncertainty in each variable from Equation 2.1 was used to determine the uncertainty in the relative stopping power calculations. The equation used to calculate the uncertainty in the stopping power is given as [31]:

$$dRSP = \frac{dR_{80,w}}{t_m} + \frac{dR_{80,m}}{t_m} + \frac{|R_{80,w} - R_{80,m}| dt_m}{{t_m}^2} \quad \textbf{Equation 2.2}$$

where $dR_{80,\,w}$ represents uncertainty in the depth to the distal 80% without material present in the beam, $dR_{80,\,m}$ represents uncertainty in the depth to the distal 80% with material present in the beam, and dt_m represents the uncertainty in the thickness of the material sample. The Zebra specifications state that the range accuracy is ±0.5mm and the uncertainty in the measured thickness is ±0.1mm.

2.2.4 Phantom Design

The phantom was designed with the considerations described in Section 2.2.2, based on the anatomical dimensions of pediatric patients treated with proton therapy at the PTC-H. Data was collected from treatment plans of five craniospinal patients, ages 5-11 years old. The measurements of the vertebral length, vertebral thickness in the sagittal plane, cartilage thickness, distance from the spinous process to the transverse processes on the left and right sides, along with the diameter of the vertebral foramen and HU of the various anatomical components, were averaged to determine the internal characteristics of the phantom. The maximum difference in the distance from the skin to the distal end of the vertebral body was used for determining the amount of simulated spinal curvature. Image of the preliminary phantom design in the sagittal and coronal planes with corresponding dimensions are shown in Figures 2.1 and 2.2.

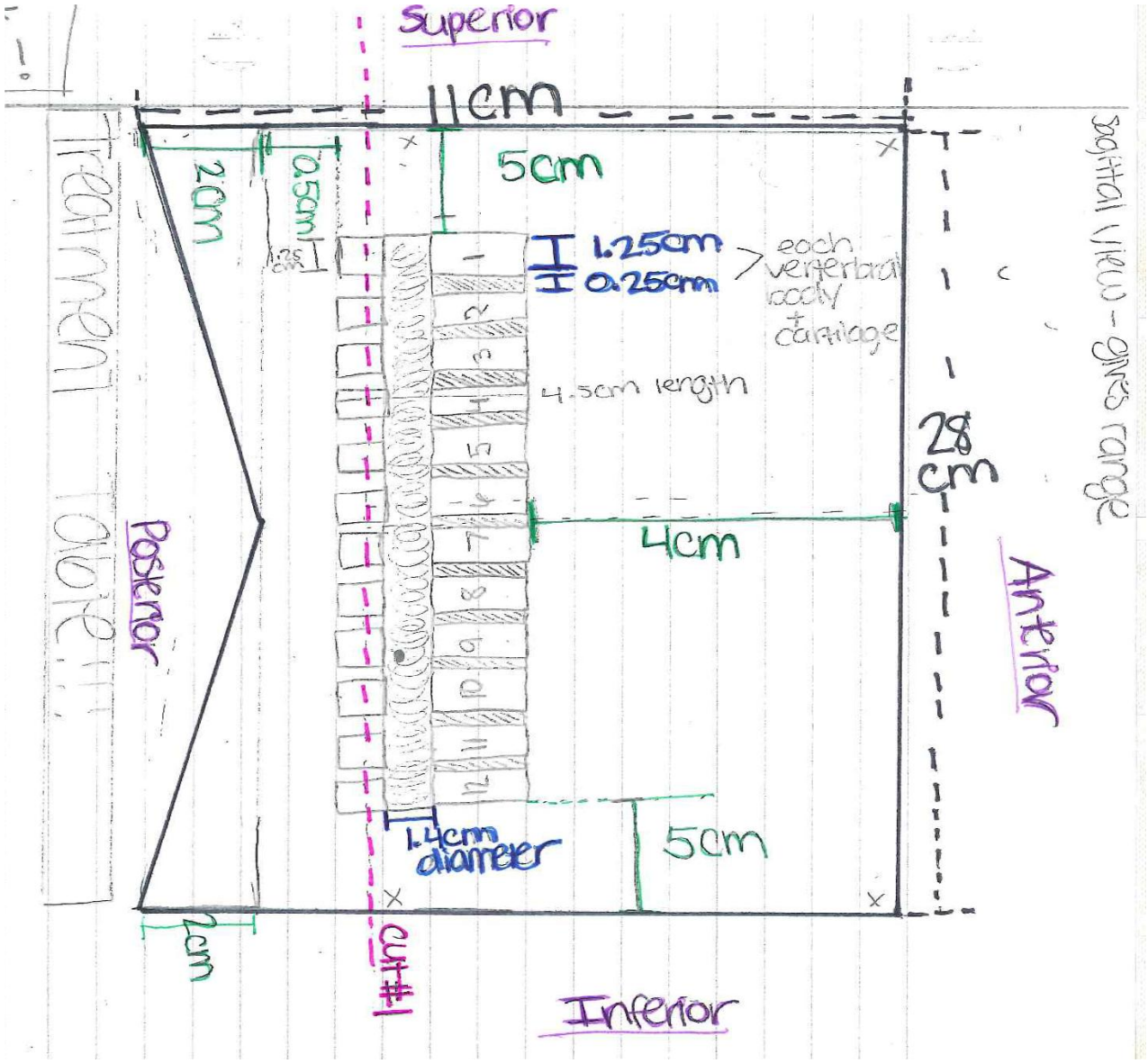

Figure 2.1 Sagittal View Diagram of the Phantom Design

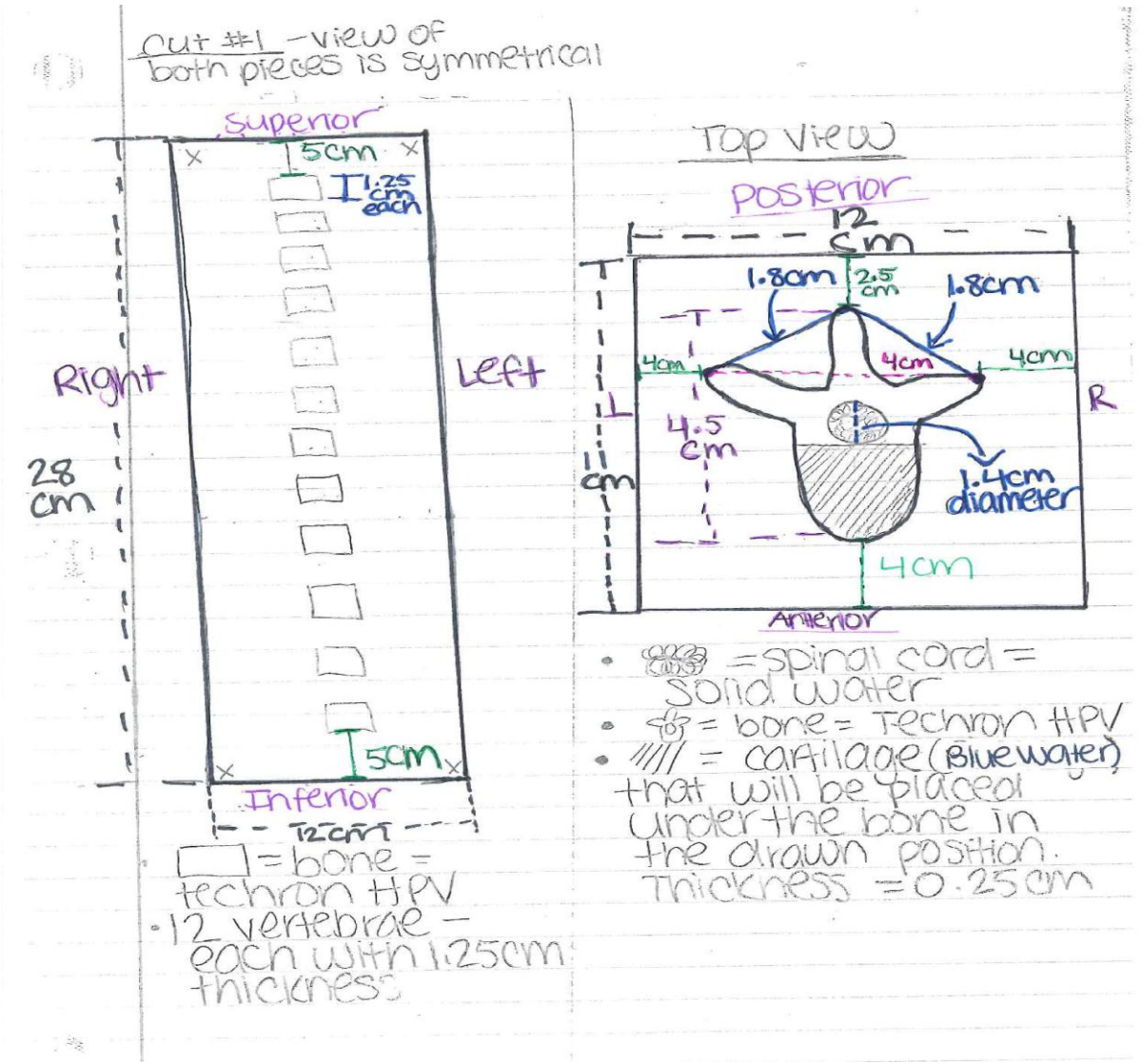

Figure 2.2 Coronal and Top views of the Phantom Design

2.3 Phantom Experiment

2.3.1 CT Simulation

All simulation images were acquired using the GE LightSpeed RT16 CT scanner at the PTC-H following the clinical pediatric spine CT protocol. Two double-loaded TLDs, along with two film dosimeters in the sagittal and coronal planes, were placed inside the phantom. Because these dosimeters would be in place for imaging and treatment, four single-loaded TLDs were placed on the exterior of the phantom to measure background radiation signal to be subtracted from the interior TLDs. The phantom was placed on the CT table in the supine position. The lasers were aligned to exterior marks delineating the isocenter. Once the scan was obtained, these images were then transferred to the Eclipse treatment planning system, where the CT couch was removed. The proton treatment couch was inserted into the images by a certified medical dosimetrist using in-house DICOM algorithm software. Images of the phantom in the axial and sagittal planes are shown in figures 2.3 and 2.4.

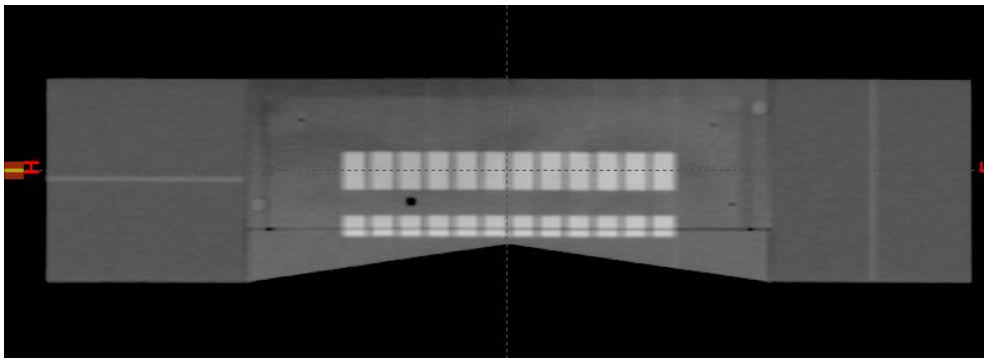

Figure 2.3: Sagittal CT image of the phantom showing locations of the vertebral bodies, cartilage and right superior TLD

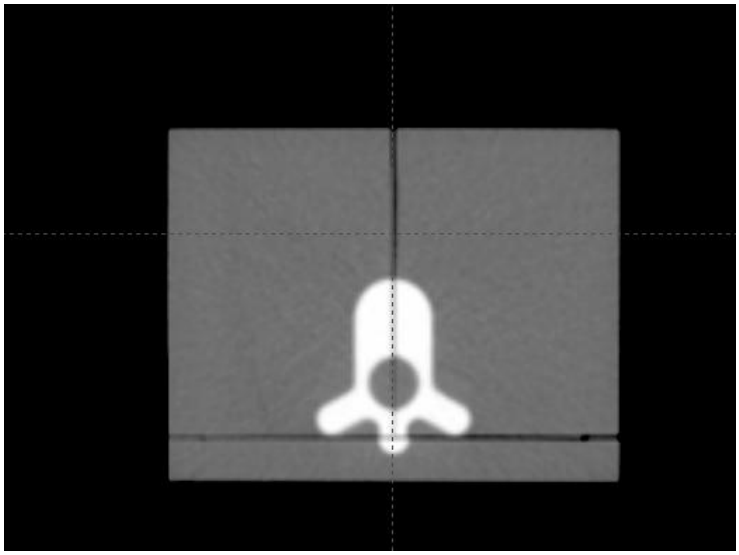

Figure 2.4: Axial CT Image of the phantom. The film planes are visible as the orthogonal black lines through the phantom.

2.3.2 Treatment Planning

The following structures were contoured on the CT images: spine, spinal cord, and body contour (including the treatment couch to account for the proton range). The vertebral body was designated as the CTV in both the passive scattering and spot scanning treatment plans and also used to determine the field parameters. Proton planning is not based on the PTV like in photon planning, as it can cause an incorrect dose estimation in the CTV [32]. Proton therapy adds additional margins not only in a direction perpendicular to the beam path, but also along the direction of the beam path. Because the margin is calculated based on the beam range, each field would have different volumetric margins, making the use of a PTV very complex.

A typical dose prescription delivered to the spine during craniospinal treatments and can range from 18-36 Gy CGE, but PTC-H uses a prescription of 23.4 Gy CGE [33]. However, based on typical IROC Houston requirements, a single dose of 6 Gy CGE was delivered to the phantom, to maintain the dose in a range appropriate to be measured with the film. As IROC

Houston does not yet have dose constraints for this phantom, the dose constraints for patients treated at the PTC-H were used. Specifically, the 6 Gy isodose line was required to cover ≥95% of the CTV, and all hot spots must be ≤107%.

Treatment plans were created with the assistance of a PTC-H medical dosimetrist and a medical physicist. Digitally reconstructed radiograph (DRR) images were also created to assist with localization during the treatment setup. A PTC-H radiation oncologist confirmed that the plan was appropriate and clinical constraints were met.

2.3.2.1 Passive Scattering Treatment Plan

Two equally weighted, posterior-anterior beams were used to create the superior and inferior spine fields of the passive scattering plan. The junction was placed in the middle of the phantom near the center of the vertebral column, with a 0.5cm gap between the fields at the surface of the phantom and a match at approximately 2cm depth in the middle of the phantom. The junction was shifted by 1 cm to create a second junction plan. For each field, brass apertures and acrylic compensators (Figures 2.5 and 2.6, respectively) were created at the PTC-H machine shop. The plan sum of the two junction plans composed the final plan.

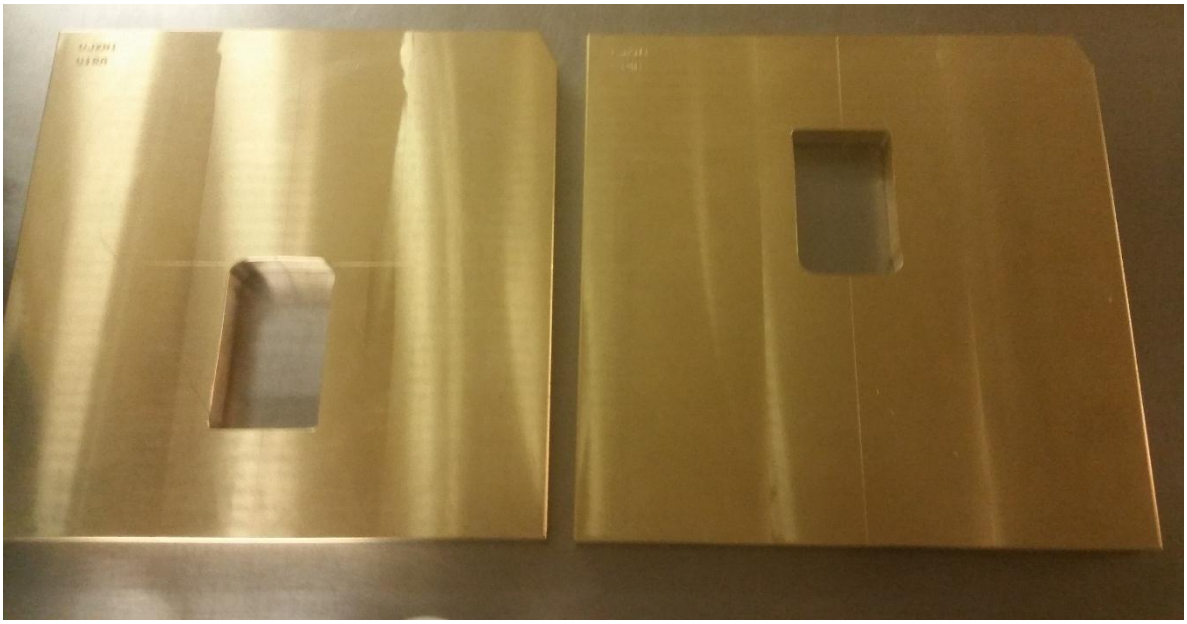

Figure 2.5: Passive Scattering Brass Apertures

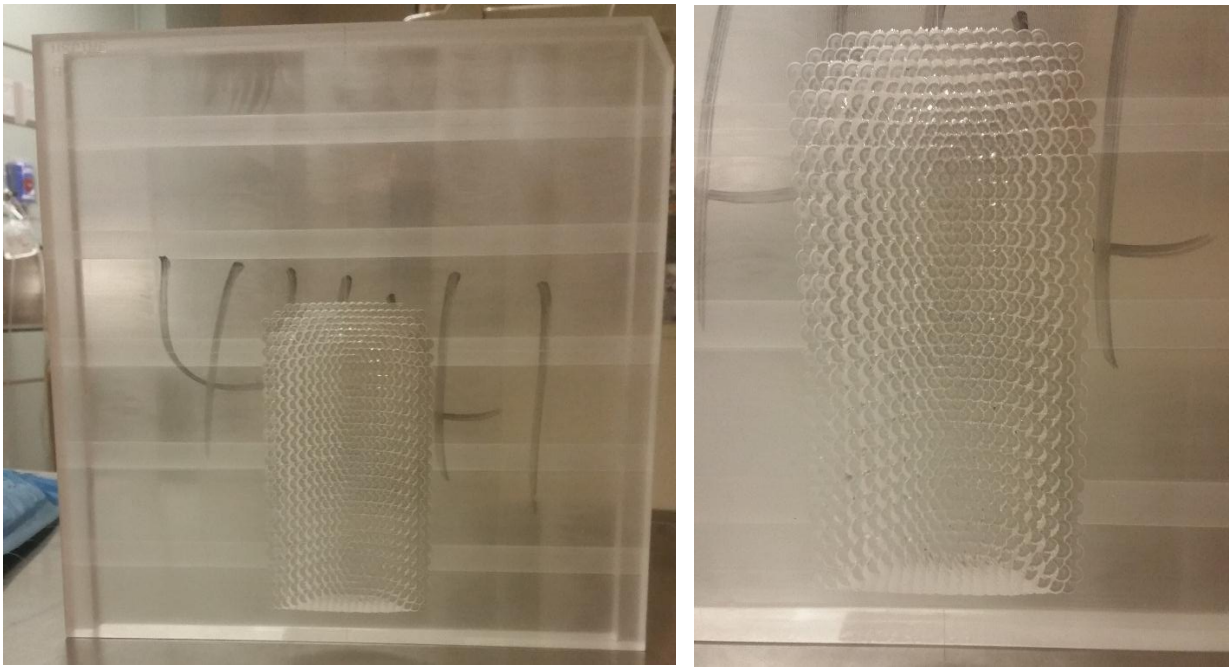

Figure 2.6: Passive Scattering Acrylic Compensators

Listed in Table 2.2 are the treatment parameters for the passive scattering plan. Figure 2.7 shows the isodose distributions in the axial, coronal and sagittal planes.

Passive Scatter Treatment Plan				
Prescribed Dose: 600 cGy				
Beam	A	B	C	D
Beam Name	Superior Spine-Jxn1	Inferior Spine-Jxn1	Superior Spine-Jxn2	Inferior Spine-Jxn2
Beam Energy (MeV)	160	160	160	160
Gantry Angle	180	180	180	180
Couch Angle	0	0	0	0
Snout Position	25	25	25	25
SOBP Width	7	7	7	7

Table 2.2: Passive Scatter Planning Parameters

a)

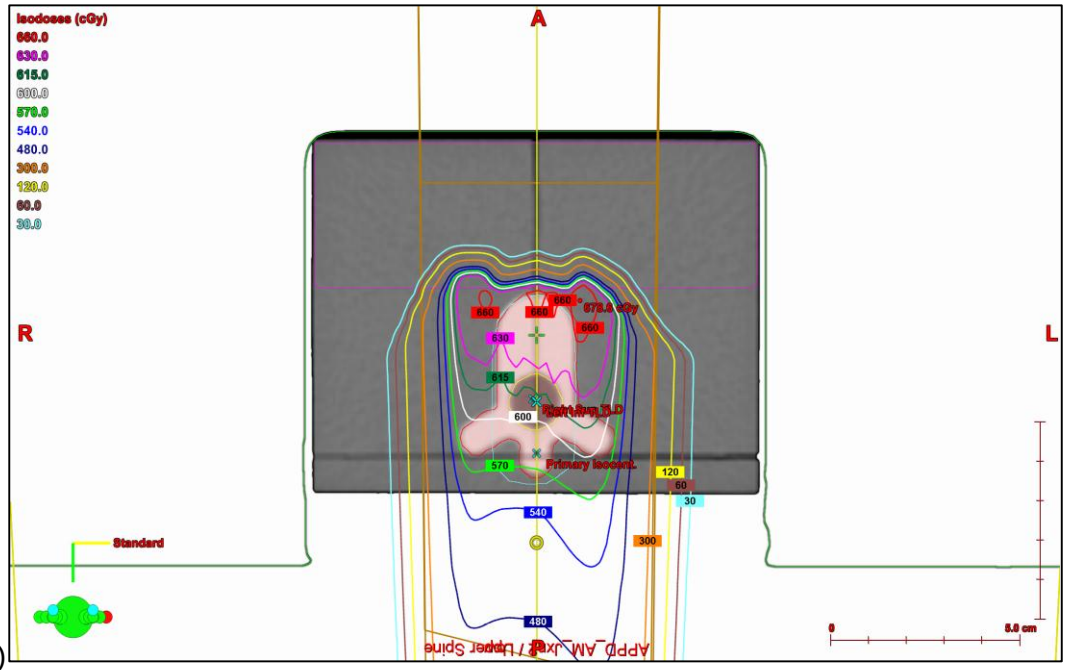

b.)

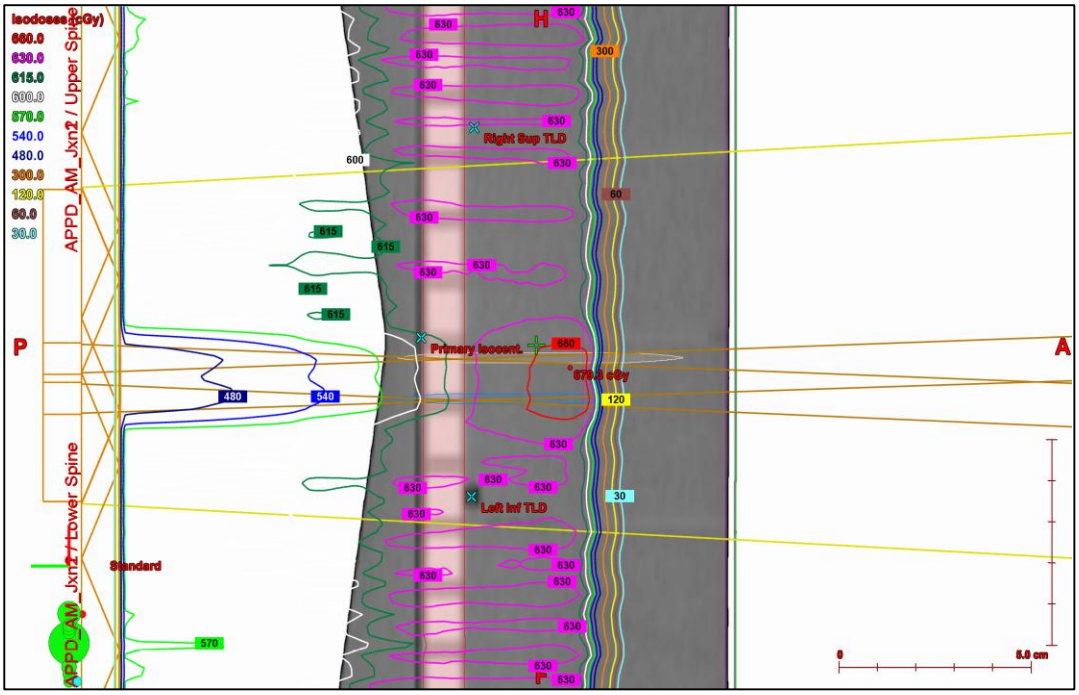

c.).

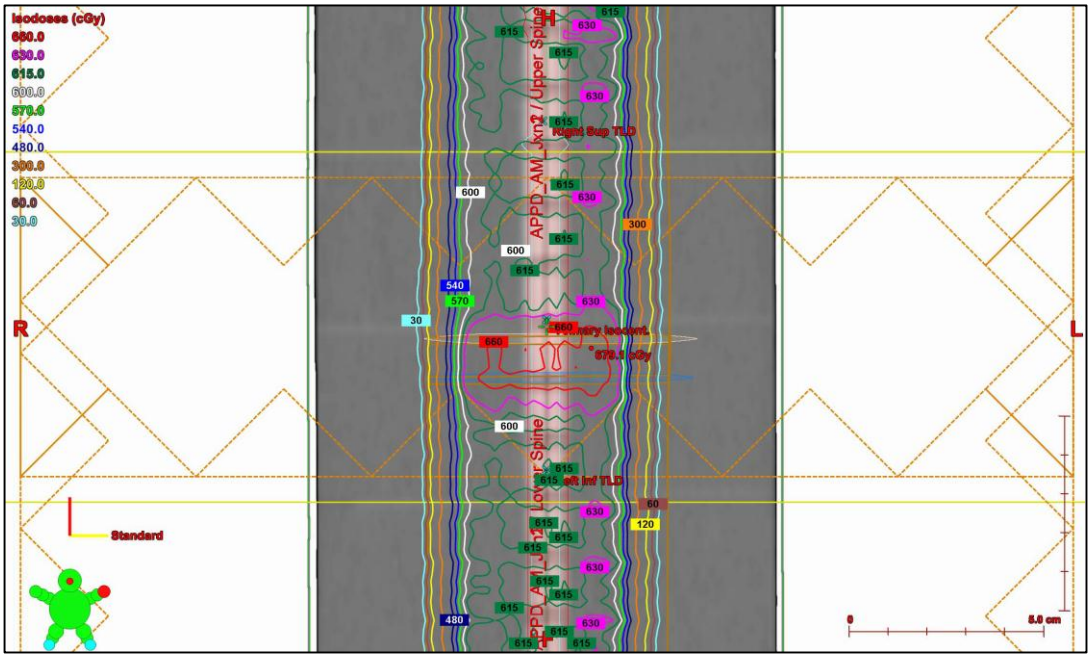

Figure 2.7: Passive Scattering Treatment plan views in the (a) axial, (b) sagittal, and (c) coronal planes.

The gantry was planned and irradiated using the G2 gantry at PTC-H. The monitor units for each field were calculated using the following equation:

$$MU = \frac{Physical\ Dose}{Relative\ Output\ Factor * Range\ Shift\ Factor * SOBP\ Output\ Factor}$$ **Equation 2.3**

The parameters used to calculate the MU are listed in Table 2.3. In the treatment plan, each field isocenter was located in the penumbra of the field, which is an insufficient position for a dose calculation point due to the high dose gradient. Therefore, a verification plan was created to determine the dose to the center of the field with the aperture in place. The dose from the verification plan was used for the dose calculation.

Passive Scatter Treatment Plan				
Prescribed Dose: 600 cGy				
Beam	A	B	C	D
Beam Name	Upper Spine-Jxn1	Lower Spine-Jxn1	Upper Spine-Jxn2	Lower Spine-Jxn2
Relative Output Factor	0.827	0.827	0.827	0.827
Range Shift Factor	0.89	0.89	0.89	0.89
SOBP Factor	1.162	1.162	1.162	1.162
Dose to Center of Field cGy-RBE (from verification Plan)	313.4	313.4	313.4	313.4
Physical Dose in cGy	284.9	284.9	284.9	284.9
MU Calculated	333.1	333.1	333.1	333.1

Table 2.3: MU Calculation Parameters for Passive Scatter Plan

2.2.2.2 Spot Scanning Treatment Plan

Similar to the passive scattering plan, two equally weighted, posterior-anterior beams were created for the spot scanning plan. This treatment plan was created for irradiation on G3, the designated spot scanning gantry at PTC-H. The junction occurs in the middle of the phantom with a field overlap of approximately 6cm. Unlike passive scattering, a hand calculation of the monitor units was not needed, as the treatment planning system conducts

this calculation. Table 2.4 contains the spot scanning treatment delivery parameters and figure 2.8 displays the isodose distributions for the spot scanning treatment plan.

Spot Scanning Treatment Plan		
Prescribed Dose: 600 cGy-RBE		
Beam	A	B
Beam Name	Upper Spine	Lower Spine
Beam Energy (MeV)	146.9	146.9
Gantry Angle	180	180
Couch Angle	0	0
Snout Position (cm)	38	38
Number of Spots (post-processed)	9012	8019
SOBP Width	7.03	7.08
MU Calculated by TPS	353.92	314.73

Table 2.4: Spot Scanning Planning Parameters

a.)

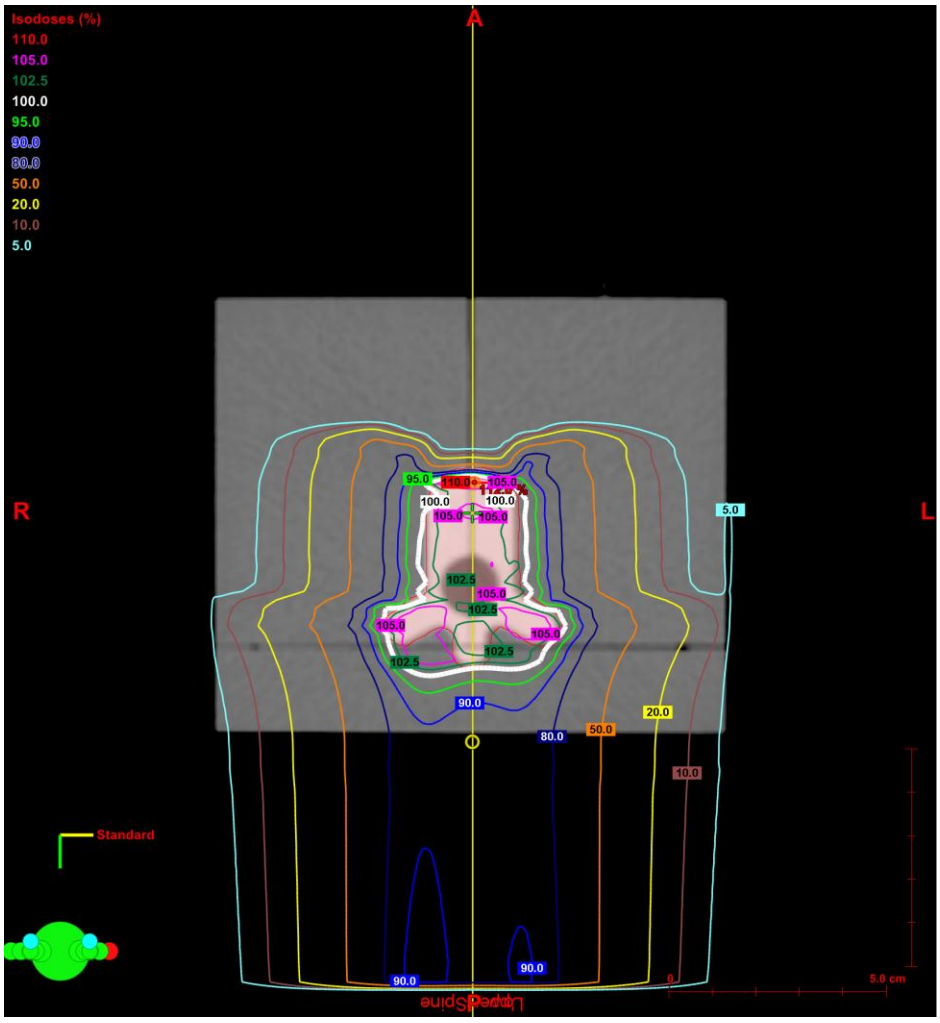

b.)

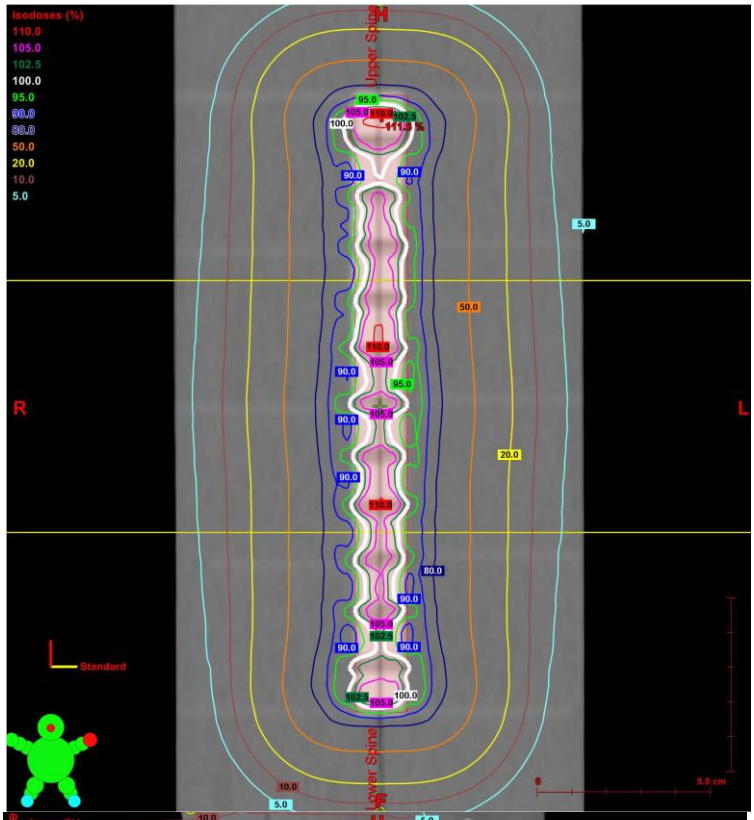

c.)

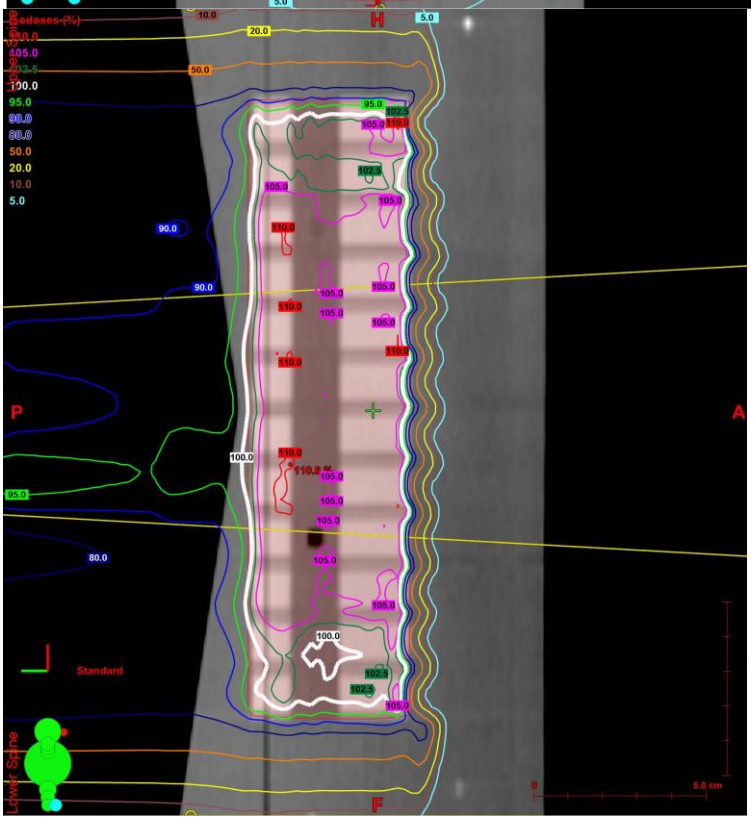

Figure 2.8: Spot Scanning Treatment plan views in the (a) axial, (b) coronal, and (c) sagittal planes.

2.3.3 Treatment Deliveries

The phantom was set up on the treatment couch and aligned to the primary isocenter placed in the middle of the phantom using the lasers. A manual couch shift was used to move the phantom to the respective superior and inferior field isocenters. X-ray images of both fields were acquired and compared to the digitally reconstructed radiographs (DRRs) from the treatment plan as an assessment and confirmation of the phantom alignment. For the passive scattering plan, additional x-ray images were taken with the apertures in place to further verify the phantom setup. Tape markings were placed on the phantom and the couch post-alignment to assist with repositioning between the disassembly and reloading of the phantom dosimeters. Both treatment plans had gantry angles of 180º and couch angles of 0º for all fields. The superior spine field was delivered first, followed by the inferior spine field. For the passive scatter irradiation, a second junction plan containing both a superior spine field and inferior spine field was delivered directly after the first junction plan. The summed dose for these passive junction plans was considered as one passive scattering treatment delivery. A biologically effective dose of 6 Gy CGE was delivered during each irradiation. Three complete phantom irradiations were conducted per treatment technique (passive scattering or spot scanning) as a part of a reproducibility study. Once the first irradiation was complete, the irradiated film and TLD inside the phantom were removed and the phantom was reloaded with unirradiated dosimeters. The phantom was repositioned based on the tape markings and x-ray images were quickly acquired to verify the alignment before the next treatment delivery began. This process was completed until all three irradiation trials were complete.

2.2.4 TLD

2.2.4.1 Point Dose

TLD is good for remote dosimetry as it is a passive detector that can be used as an absolute dosimeter. The TLDs measure the dose delivered at their respective locations in the

right superior and left inferior positions of the phantom spinal canal. Thermoluminescent materials contain trapping (F) centers that collect a charge proportional to the dose deposited. As the radiation interacts with the TLD, electron-hole pairs are created and may become trapped in the F centers between the conduction band and valence band. Heating the TLD can cause the release of electron-hole pairs from the traps to conduction and finally, the release of the signal as electrons migrate from the conduction band and recombine with holes in the valence band [34]. This signal is captured by a photomultiplier tube that counts the amount of charge collected. This charge, along with a series of correction factors, is used to calculate the delivered dose.

IROC Houston uses TLD-100 (Harshaw Chemical Company, Solon, OH), a lithium fluoride TLD powder doped with Mg and Ti to create the trapping centers. Approximately 25 mg of powder is placed into polyethylene capsules allowing for easy placement into the phantom. A previous study has determined that using TLD-100 as a dosimeter for protons with energies of 100 to 250 MeV produced accurate dose measurements within 5% of the expected dose [35]. This conclusion, along with studies by former RPC physicists allows for confidence use of TLD-100 as a dosimeter for this proton phantom [36].

The delivered dose to the TLD is calculated using the following equation:

$$\boldsymbol{Dose = \left(\frac{TL}{mass}\right) x\, S\, x\, K_F\, x\, K_L\, x\, K_E\, x\, 1.1} \qquad \textbf{Equation 2.4}$$

where TL represents the TLD signal in nC, mass is the mass of the TLD powder in mg, S is the system sensitivity, K_F represents the fading correction factor, K_L is the linearity correction factor and K_E is the energy correction factor. Because TLD measured the physical dose delivered to the phantom, the RBE correction of 1.1 must be included in the dose calculation to give the biological effective dose.

The signal of the TLD was normalized to the mass of the powder during the readout so that differences in the mass were not factored into the dose calculation. The system sensitivity factor (dose/signal) is the considered the calibration factor, to account for the dose response and change from ^{60}Co reference conditions to proton conditions. This calibration factor is most critical, as it accounts for any variation between readout sessions, such as days since irradiation and reader variability, and also relates the charge collected to the dose measured. The system sensitivity is calculated by

$$S = \frac{Dose}{K_F \, x \, K_L \, X \left(\frac{TL}{mass}\right)_{AVG}} \qquad \textbf{Equation 2.5}$$

The system sensitivity calculation uses the calculated fading, linearity and expected dose of the TLD standards.

Fading occurs when trapped electrons are unintentionally released before the readout session occurs. The fading correction for the phantom TLD is calculated using Equation 2.6:

$$K_F = \frac{N}{ae^{-bx} + ce^{-dx}} \qquad \textbf{Equation 2.6}$$

where N, a, b, c, and d are coefficients that were determined based on the fading characterization previously conducted by IROC Houston. The values of these coefficients will be stated in a later subsection. TLD should be read out no sooner than 10-14 days post-irradiation due to the instability of and rapid change in the fading process.

The linearity correction factor accounts for the non-linearity in the TLD response over the range of doses used for readout. It is important that the standards are irradiated in a dose range comparable to the phantom TLD so that the linearity correction is minimized. Equation 2.7 states the linearity correction factor equation:

$$K_L = ax^2 + bx + c \qquad \textbf{Equation 2.7}$$

where a, b, and c are variables determined by IROC Houston during the TLD batch characterization, and x is raw dose as determined by multiplying the normalized TLD reading by S and $K_{F.}$

TLD has an energy dependence and the change in response due to energy must be corrected for if the calibration and experimental TLDs are irradiated at energies different than the ^{60}Co reference energy. IROC Houston irradiates the TLD standards using ^{60}Co as the reference beam and also has compared the TLD response to the response of TLD at all proton energies. The proton energy correction factor, $K_{E,}$ has been determined to be unity (within 4%, with a standard deviation of 2%).

In order to properly determine the correction factors previously listed, a set of standards was irradiated to a known dose as a calibration. The standards were irradiated to a known dose of 800 cGy on a Co-60 machine. By irradiating a set of TLD to a known dose, the reference conditions needed to determine the correction factors was established.

During the TLD readout session, first, a set of standards were read, followed by a set of controls. Then, 6 irradiation TLD can be read before another set of controls must be read. This process of alternating between the readings of irradiation TLDs and controls was repeated until all irradiation TLD had been read. The session was closed out by the reading of controls followed by standards.

The TLD batch B11 was used for the phantom. Previous batch characterization by IROC Houston staff was completed before the start of this project. Table 2.5 lists the fading and linearity corrections factor constants introduced in Equations 2.6 and 2.7, respectively.

Fading Correction Constants			Linearity Correction Constants	
N	1.3493		a	2.552065E-08
a	1.2815		b	-2.221104E-04
b	0.00010885		c	1.064337
c	0.067810			
d	0.071908			
x	# days from irradiation date to reading date			

Table 2.5 Fading and Linearity Correction Factor Constants

The TLDs for the passive scatter and spot scanning irradiations were read out 10 days and 22 days post-irradiation, respectively. The point dose criteria, as stated in the experiment hypothesis, was agreement within ±5%. Therefore, the ratio between the measured TLD dose and the calculated TPS dose would have to fall within the range of 0.95-1.05 to meet the agreement. To calculate the reproducibility of the experiment, the coefficient of variation was calculated and hypothesized to be less than 3%.

2.3.5 Film Planar Dosimetry

Radiochromic film, specifically GAFchromic® EBT2 film (Ashland Inc., Covington, KY), was used as the passive detector to observe the dose distribution in the coronal and sagittal planes of the phantom. Characteristics of radiochromic film including high spatial resolutions, a weak energy dependence over the dose range and radiation beam quality, near tissue equivalence, minimum sensitivity to visible light, and the development of film in real time without processing makes this a suitable detector for remote dosimetry [37]. The lot number used for the entirety of this study was #07301301 with an expiration date of July 2015. A diagram of the cross-sectional components of the film from the GAFchromic® EBT2 film specifications is shown in Figure 2.9.

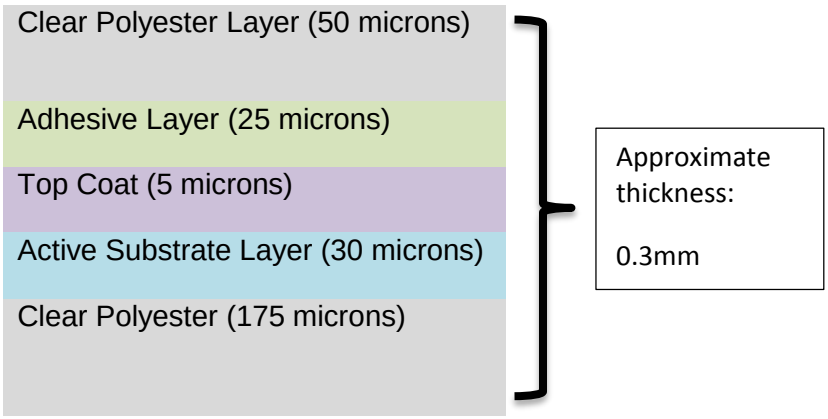

Figure 2.9 Cross-Sectional Layer Diagram of GAFchromic® EBT2 film

2.3.5.1 Film Calibration

The film batch was calibrated using a passive scatter irradiation technique at PTC-H. The irradiation conditions were as follows: medium snout size, 4 x 4 cm aperture field size, 160 MeV beam energy, SOBP of 10cm, and 8cm of buildup material above and below the phantom. The film was cut to a size of 7 x 7cm^2 prior to the calibration irradiation. Care was taken to ensure that each film was irradiated in the same manner, as EBT2 has a known orientation sensitivity and there are inhomogeneities in the scanner [38]. Based on the irradiations from previous film calibrations by IROC Houston, the doses chosen for irradiation were: 50, 100, 150, 200, 300, 400, 500, 600, 700, and 800 cGy. The MU used to irradiate the film at each dose level was calculated using Equation 2.3. RBE was not included in this set of MU calculations, since the film dose distribution were eventually normalized to the TLD which included the RBE.

The film was placed between slabs of acrylic, with the center of the film set up at isocenter, or 270 cm source-to-axis-distance (SAD). The film was irradiated with 160 MeV protons, as this is the energy used by our institution to treat pediatric craniospinal patients. The dose is specified at the center of the SOBP, which was at a depth of 8cm for a 160 MeV beam in a proton snout. The same amount of material was placed behind the film to ensure that the beam did not extend beyond the phantom. Figure 2.10 shows a picture of the setup.

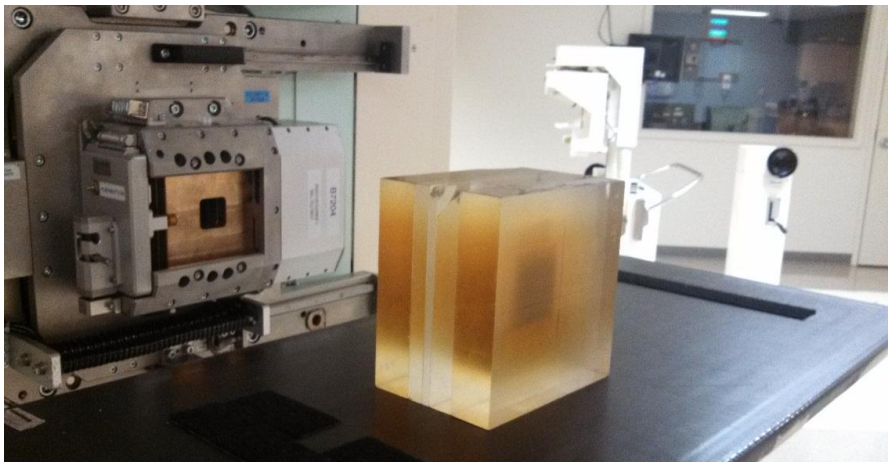

Figure 2.10 Film Calibration Irradiation Setup at PTC-H.

The films needed to be analyzed to determine the optical density (OD) for the creation of the dose response (dose vs. OD) curve. Studies have shown that, conservatively, film should sit for at least 48 hours before readout to account for any possible fading changes of the film [38]. The calibration films in this study were scanned 5 days after irradiation using the CCD Microdensitometer for Radiochromic Film Model CCD100 (Photoelectron Corporation, Lexington, MA) at IROC Houston. A spatial calibration and flat field adjustment was conducted using a blank piece of film from the same batch prior to the scanning of the other films. Three OD measurements were taken using the software ImageJ (Rasband 1997-2011) and averaged for each dose. A third degree polynomial was fit to the dose vs. OD plot to create the film calibration curve. This dose response curve was used for both passive scattering and spot scanning irradiations, since studies have shown that the calibration curve for spot scanning systems is similar to the curve for passive scattering systems [39, 40].

2.3.6 Dosimetric Analysis

2.3.6.1 CT, Film and TLD Registration

IROC Houston uses a MATLAB®-based, in-house developed software, to register the scanned film images with the CT structures, images and the composite dose information from the treatment plan. The orientation of the film and the TLD locations also need to be registered with the data from the treatment planning system. The pin locations in the phantom dictate the spatial orientation of the film in both planes relative to the phantom structures. These pin points were used as registration locations for the software.

To determine the coordinates of the pin pricks relative to the primary isocenter (in the middle of the phantom), the distance from isocenter to the respective locations of the pin pricks and the TLD placeholders must be determined. This was done using a ruler and a pricked piece of grid paper. These coordinates were input into an excel spreadsheet used by the program. The CT images were registered to these coordinates after selecting the isocenter to be in the middle of the phantom and measuring the distance to all 6 pins. Additionally, the coefficients from the OD-dose calibration curve were entered into the spreadsheet so the proper dose conversion can be applied.

Once the registration information was properly input, the scanned film images can be opened in the software. The physical locations of the pin pricks on the film were identified to complete the 2D-registration (see Figure 2.11). The error in registration was calculated by the software and displayed as root mean square (RMS) to determine the goodness of fit. Next, the proper OD-dose curve was selected and the TLD doses in Gy CGE were entered. A correction was applied to the film image to convert the displayed OD to displayed dose and to scale the dose grid of the film to the measured TLD dose. An example of the selected registration points, the OD-to dose conversion and the RMS error is shown in figure 2.15. The composite file containing the CT images, contour structures and dose information was then opened with

Computation Environment for Radiotherapy Research (CERR). Within CERR, the locations of the pins on the CT images were again identified and selected. The in-house software then used CERR to complete a 3D-registration of the film and CT images for comparison purposes. This is a standard procedure used by IROC Houston to register films from anthropomorphic phantoms. The software also calculates an RMS error for 3D registration, which should be less than 2mm.

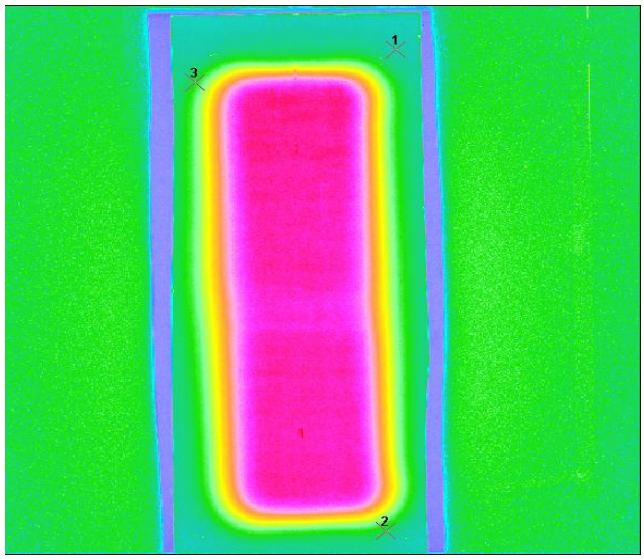

Figure 2.11 Selection of the pin prick registration points on a scanned coronal film

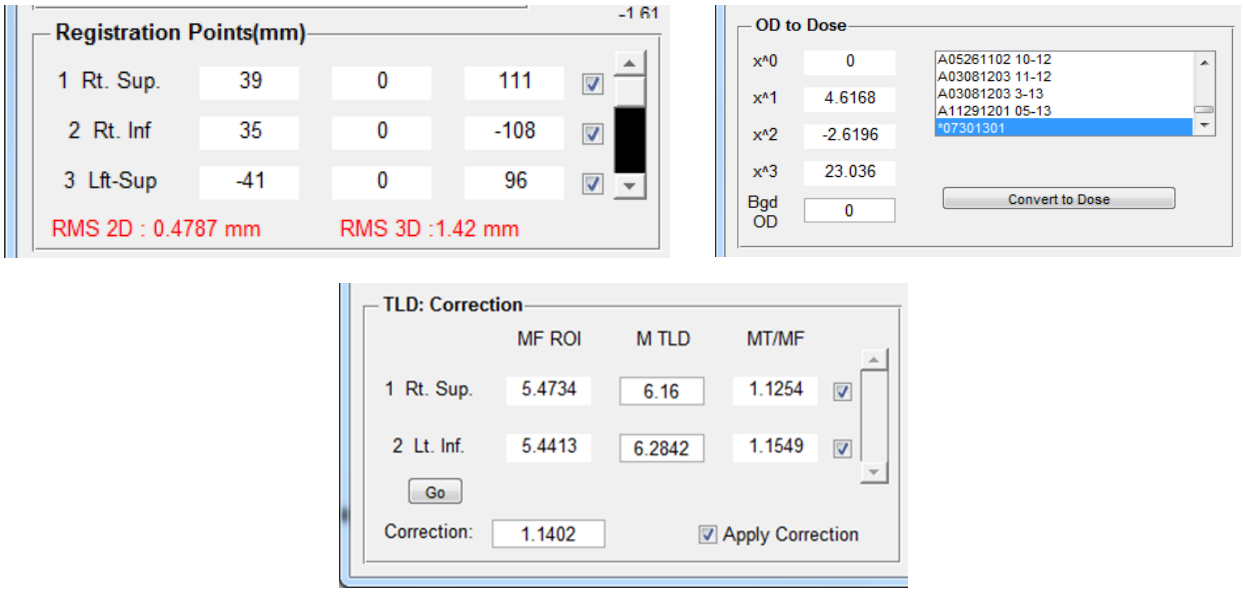

Figure 2.12: The displayed RMS error, OD to Dose Conversion and TLD correction in MATLAB®

2.3.6.2 Gamma Analysis

To evaluate the agreement between the 2D dose distributions of the film and TPS, a gamma analysis calculation was performed in the in-house software [41]. A dose and distance to agreement criteria of ±5%/3mm and ±5%5mm were both used in the comparison. For each film plane, a rectangular region of interest was designated for inclusion of the entire dose distribution in the calculation. A mask was applied to regions of the image that should not be included in the calculations, such as blank regions of 0 dose acquired by the densitometer and regions of high OD values from the pin pricks. As stated in the hypothesis, an 85% pixel pass rate was used as part of the gamma analysis criterion.

2.3.6.3 Distance to Agreement

Dose profiles were also created in the MATLAB® software program in the right-left, anterior-posterior, and superior-inferior directions. A set of the profiles was taken in both the superior and inferior spine fields on both film planes. In the anterior-posterior direction, the superior field profile is acquired through the bone, while the inferior field profile is acquired through the cartilage. This is done for comparison of profile discrepancies between the two materials. The junction matching profiles were acquired in the superior-inferior directions of both planes. The cold spot profile was taken in the center of the coronal film, while the hot spot profile was acquired toward the anterior edge of the sagittal film. Because the phantom was set up supine, the cold spot appeared near the surface of the phantom, while the hot spot occurred at depth.

These profiles were used to determine the distance to agreement (DTA) between the film and the TPS and also the junction match agreement. The DTA measurements were calculated in the distal-fall off regions in the right, left and anterior directions. A linear

regression was fit to the TPS and film data between the 75% dose and 25% dose thresholds. Comparison points of the displacement between the TPS and film were taken at 25%, 50% and 75% of the dose, in the steep dose fall off region at the edge of the CTV. These displacements were averaged on both sides of the profile to determine the DTA. To correlate with the gamma analysis criteria, an acceptable DTA would be less than or equal to 5mm. In the superior-inferior profiles, the spatial shift and dose difference at the junction was evaluated. To determine the junction shift at the peaks, the user estimated the peak center location on the graph. A function determined in the profile data the closest distance to the user-selected value and the corresponding dose at this point. This process was done for both the film and TPS profiles. Based on the determined peak centers, the percent difference between the film and TPS doses along with the spatial shift between their respective locations is calculated. To be deemed acceptable, there should be no more than a 5mm shift. Additionally, the percent dose difference between the hot/cold spot peaks should be less than 7%. The percent dose difference was chosen to correlate with the criteria from the gamma analysis and TLD, with additional margins to account for the increased dose variation at the junction.

3 Results/Discussion

3.1 Phantom Materials

3.1.1 Relative Linear Stopping Power

The goal during the phantom design was to incorporate materials that simulated the thoracic spinal column of a pediatric patient. A total of eleven potential bone substitute materials were tested to determine the relative proton stopping power and Hounsfield unit values. Table 3.1 contains the potential materials with their corresponding HU and RSP at 160 MeV and 250 MeV. Because most craniospinal treatments use a 160 MeV beam, the stopping powers corresponding to this energy were used for determining patient proton equivalency.

Material Name	HU ± SD	RSP at 160 MeV	RSP at 250 MeV	Mean RSP	Percent Difference (160 vs 250 MeV) (%)
Gammex Inner Bone	70 ± 30	1.61	1.60	1.61	1.0
Gammex Cortical Bone	843 ± 87	1.09	1.08	1.09	1.3
B200 Bone	250 ± 17	1.10	1.09	1.10	0.9
Techron HPV Bearing Grade	596 ± 14	1.30	1.28	1.29	1.3
Ketron PEEK GF30	604 ± 5	1.41	1.39	1.40	1.4
Polyester PETP Ertalyte TX	332 ± 20	1.36	1.34	1.35	1.7
Ketron HPV Bearing Grade	298 ± 21	1.35	1.33	1.34	1.6
Polyester PETP Ertalyte	272 ± 10	1.30	1.28	1.29	1.8
Duratron T4301 PAI	287 ± 19	1.36	1.34	1.35	1.3
Concrete	933 ± 169	N/A	1.86	1.86	Incalculable
Crayola Clay	1029 ± 15	1.61	1.61	1.61	0.0
Human Vertebrae	(Average) 650			1.3	
Human Cartilage	(Average) 110			1.1	

Table 3.1 Comparison of HU and measured RSP at 160 MeV and 250 MeV for each phantom material

The largest percent difference between the stopping powers at the two proton energies was less than 1.8%. This agreement indicates that the potential phantom materials can be used as anatomical substitutes for proton beam energies between 160 MeV and 250 MeV, as the stopping power does not vary with energy significantly. The RSP and percent difference at 160 MeV was incalculable for concrete. The thickness of the sample in this beam path was 9cm. The proton beam at this energy was unable to fully penetrate the slab and acquire an accurate depth dose curve.

In order to be considered patient-equivalent in a proton beam for this study, the HU needed to fall within the range measured in actual pediatric patients. Additionally, the error between the measured RSP and the calculated RSP from Eclipse should be minimal (within 5%), as this introduces range uncertainties [27]. Based on the measured data in Table 3.1, Techron HPV Bearing Grade (Boedeker Plastics, Inc., Shiner, TX) was selected as the bone substitute material for the phantom, with a measured HU and RSP of 596 and 1.3, respectively. Previous IROC Houston experiments contained data for two materials that closely simulated the patient characteristics of cartilage: blue water and PRESAGE®. The error in the proton range was calculated to determine the appropriate candidate for the cartilage substitute. This calculation was also completed for the Techron HPV Bearing Grade and for Gammex B200, another potential bone substitute whose (HU, RSP) point was also in the close proximity to the calibration curve.

To determine the range error, a linear equation was formulated between 2 points on the calibration curve surrounding the material point. The measured HU of the material was used to determine the ideal RSP that corresponded to the material point lying directly on the curve. A percent error was calculated between the measured and calculated RSP. This error was translated into mm based on the material thickness when used in the phantom. An example of the linear equation formulation is shown in Figure 3.1. The results of this error calculation for the selected phantom materials are shown in Table 3.2.

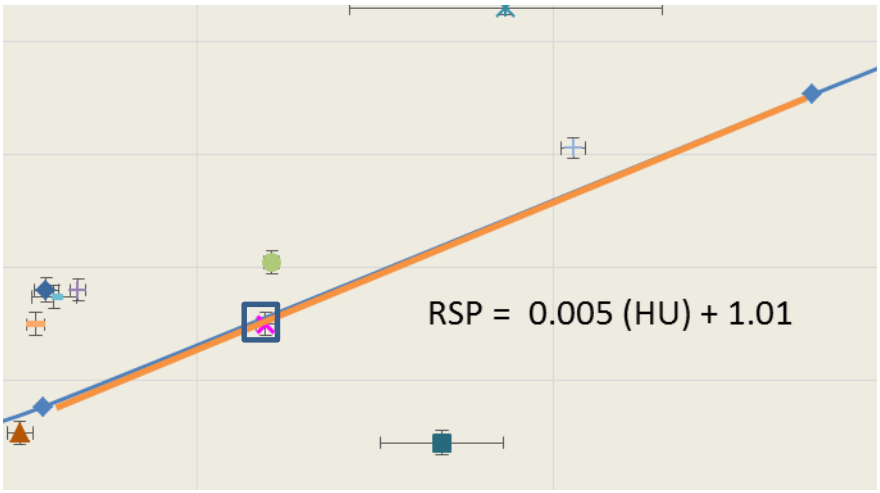

Figure 3.1 Formulation of Linear Equation between 2 (blue) points on HU-RSP Calibration curve surrounding a material point (highlighted). The equation is represented by the orange line.

Material Name	Theoretical RSP at 160 MeV	Measured RSP at 160 MeV	Percent Error (%)	Material Thickness in Phantom(cm)	Error (mm)
PRESAGE®	1.1	1.1	0.04	2	0.0
Blue Water	1.1	1.1	0.3	2	0.1
Techron HPV Bearing Grade	1.3	1.3	1.2	4.5	0.6
Solid Water	1.0	1.0	0.6	11	0.6
B200	1.1	1.1	5.1	4.5	2.3

Table 3.2 Comparison between measured RSP measurements for phantom tested at 160 MeV to the RPS calculated by Eclipse for a given HU.

PRESAGE® was not determined to be a feasible cartilage substitute for the phantom. It would have been difficult to ensure that the batch used in the phantom would have an identical composition to the sample tested in Table 3.2. Therefore, blue water, which was determined to have an HU of 86 and a RSP of 1.1, was chosen as the cartilage material. An error of 5.1% was observed between the measured and calculated RSP for B200. Although this error only translates to a 2mm range uncertainty, the HU of B200 also falls slightly outside the range observed in patients. The sub-mm range error and appropriate HU value observed with Techron HPV Bearing Grade made this material be the most suitable as the proton bone substitute.

Figure 3.2 shows the Eclipse TPS HU-RSP stopping power curve with the data for each bone equivalent material tested. The standard deviation of the HU is shown in Figure 3.2 as horizontal error bars and the RSP uncertainty at 160 MeV is shown as the vertical error bars for each material tested. For the concrete sample data point, the RSP uncertainty at 250 MeV was used. The bone material selected shows good accuracy and precision compared to the materials that were deemed inadequate for use as proton bone substitutes in the phantom. The Techron HPV Bearing Grade material has a 2.3% and 1.9% uncertainty for the measured HU and RSP, respectively.

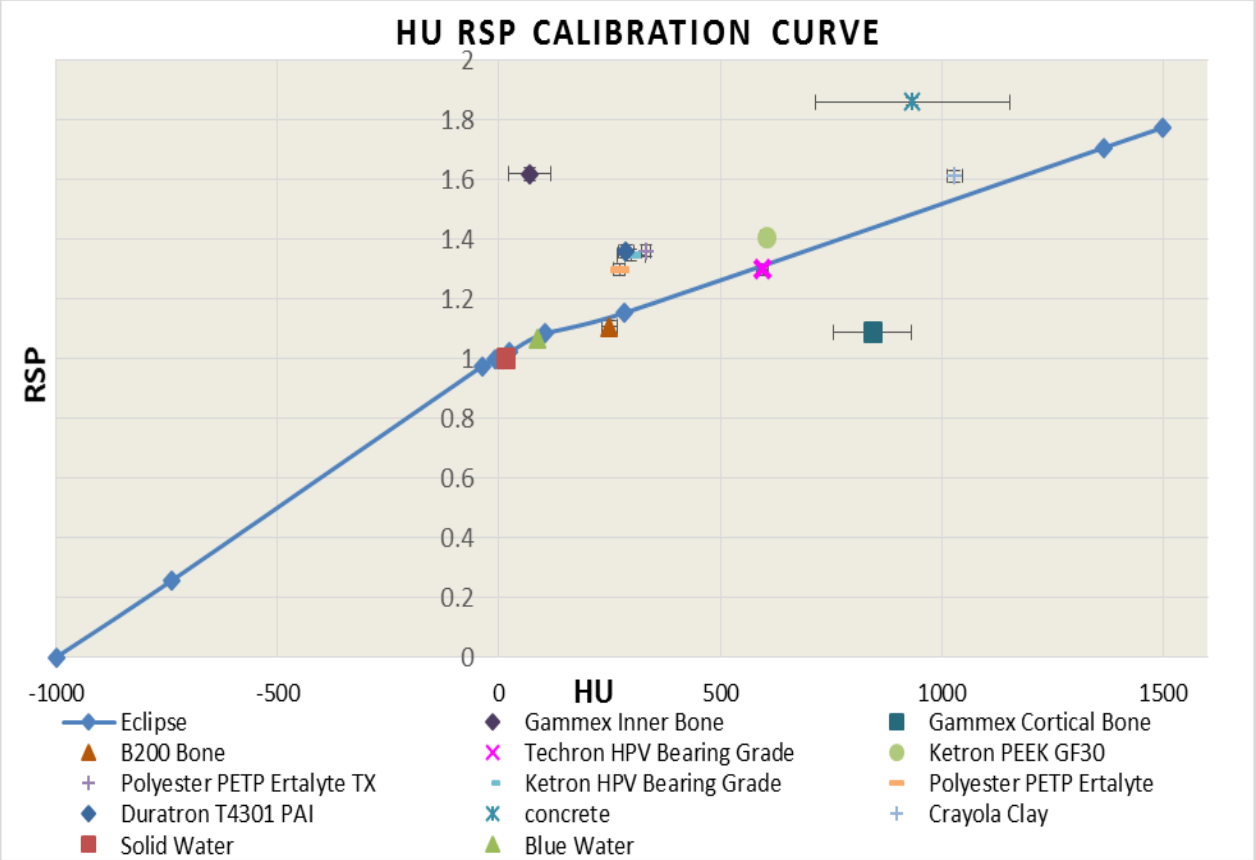

Figure 3.2: Relative Stopping Power vs Hounsfield unit calibration curve comparing tested materials with the Eclipse treatment planning system.

3.1.2 RSP Error Analysis

The uncertainty in the measured RSP for each material was computed using Equation 2.2 for both proton energies. The results are listed in Table 3.3. The percent uncertainty was ranged from 1.8-2.0% for all materials tested and the uncertainty for Techron HPV Bearing Grade was 1.9%. As previously mentioned, the largest percent difference between the stopping powers at 160 and 250 MeV energies was less than 1.8%.This variation was less than the uncertainty in the measurement of Techron HPV Bearing Grade.

Material Name	% Uncertainty at 160 MeV	% Uncertainty at 250 MeV
Gammex Inner Bone	2.0	2.0
Gammex Cortical Bone	2.0	2.0
B200 Bone	2.0	2.0
Techron HPV Bearing Grade	1.9	1.9
Ketron PEEK GF30	2.0	1.9
Polyester PETP Ertalyte TX	1.8	1.8
Ketron HPV Bearing Grade	1.9	1.9
Polyester PETP Ertalyte	1.9	1.9
Duratron T4301 PAI	2.0	2.0
Concrete	N/A	1.1
Crayola Clay	1.8	1.9

Table 3.3: Percent Uncertainty in Relative Stopping Power Measurements at 160 MeV and 250 MeV

3.2 Phantom Design

The results from the patient measurements acquired from the Eclipse TPS are shown in Table 3.4. This information was used to design the internal dimensions of the phantom. A portion of this data was also used for determining the HU range when analyzing potential phantom materials.

Parameter	Measurement
Vertebral body thickness (sagittal cut)	1.25 cm
Cartilage Thickness	0.25 cm
Vertebral length	4.5 cm
Distance from skin to end of vertebral body	6.2 cm
Distance from Spinous Process to transverse process -Left	1.75 cm
Distance from Spinous Process to transverse process -Right	1.85 cm
Diameter of vertebral foramen	1.4 cm
Skeleton Hounsfield Unit Range	300-1000 HU
Spinal Cord Hounsfield Unit Range	30-70 HU
Cartilage Hounsfield Unit Range	80-140 HU

Table 3.4: Summary of anatomical parameters averaged from five craniospinal patients

Figure 3.3 shows the sagittal diagrams of the patient right and left pieces of the phantom design. Figure 3.4 is an actual image of these pieces post construction. In the diagram, the maroon color represents the soft tissue substitute, while the lighter blue represents the cartilage substitute and the dark blue represents the bone substitute. The red holes are the TLD in the right superior and left inferior positions. The concentric rectangular pattern represents an indentation of 0.25mm, or the thickness of the GAFCHROMIC® film. This indentation is more clearly seen in the physical image of the phantom and ensures a sealed closure when the sagittal film is placed. What is not visible in the diagram, but visible in Figure 3.4 are the pen pricks in anterior superior, anterior inferior and posterior inferior positions.

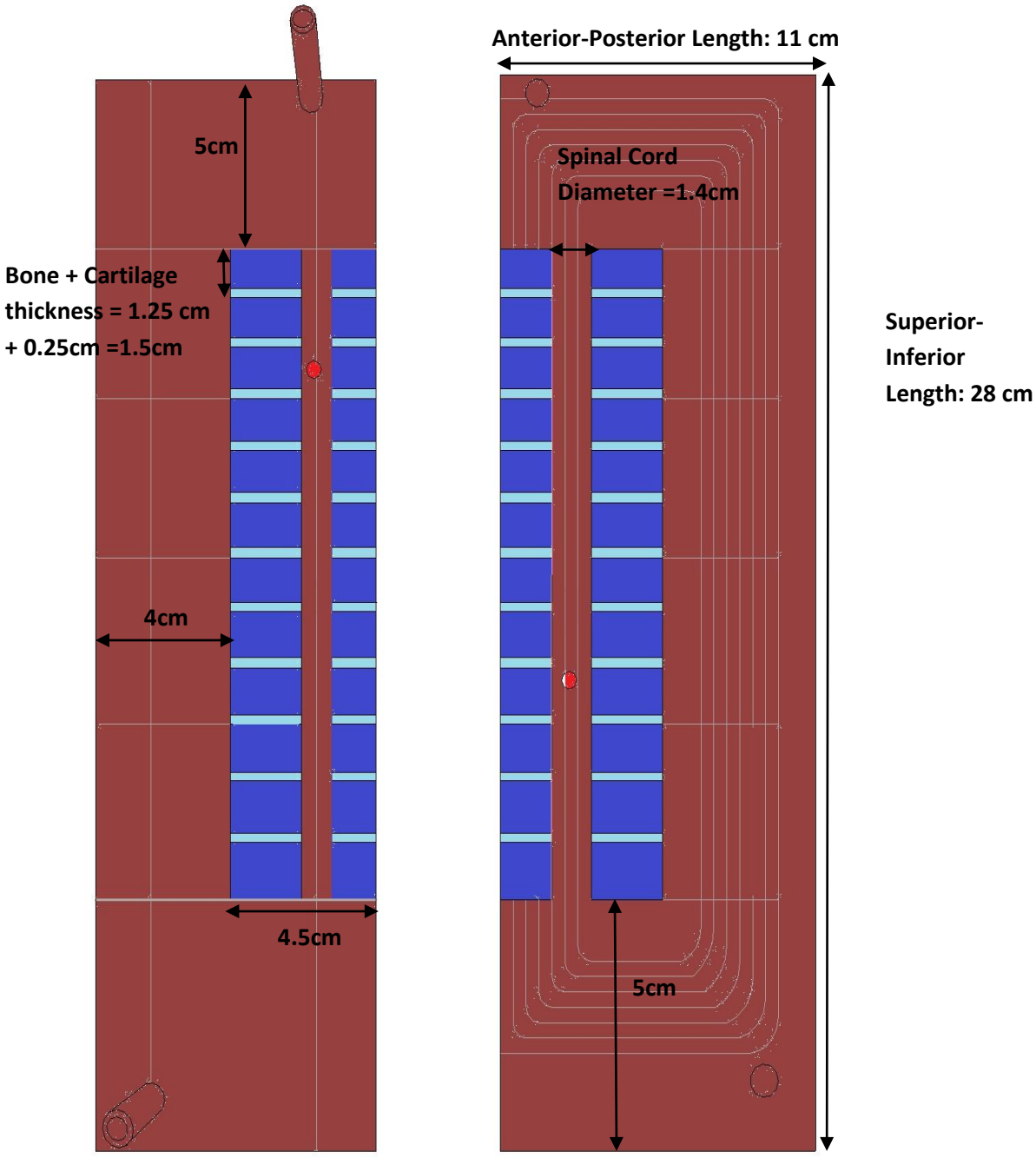

Figure 3.3: Sagittal Diagram of the Phantom showing the TLD (red), soft tissue (maroon), bone (dark blue) and cartilage (light blue) substitute dimensions.

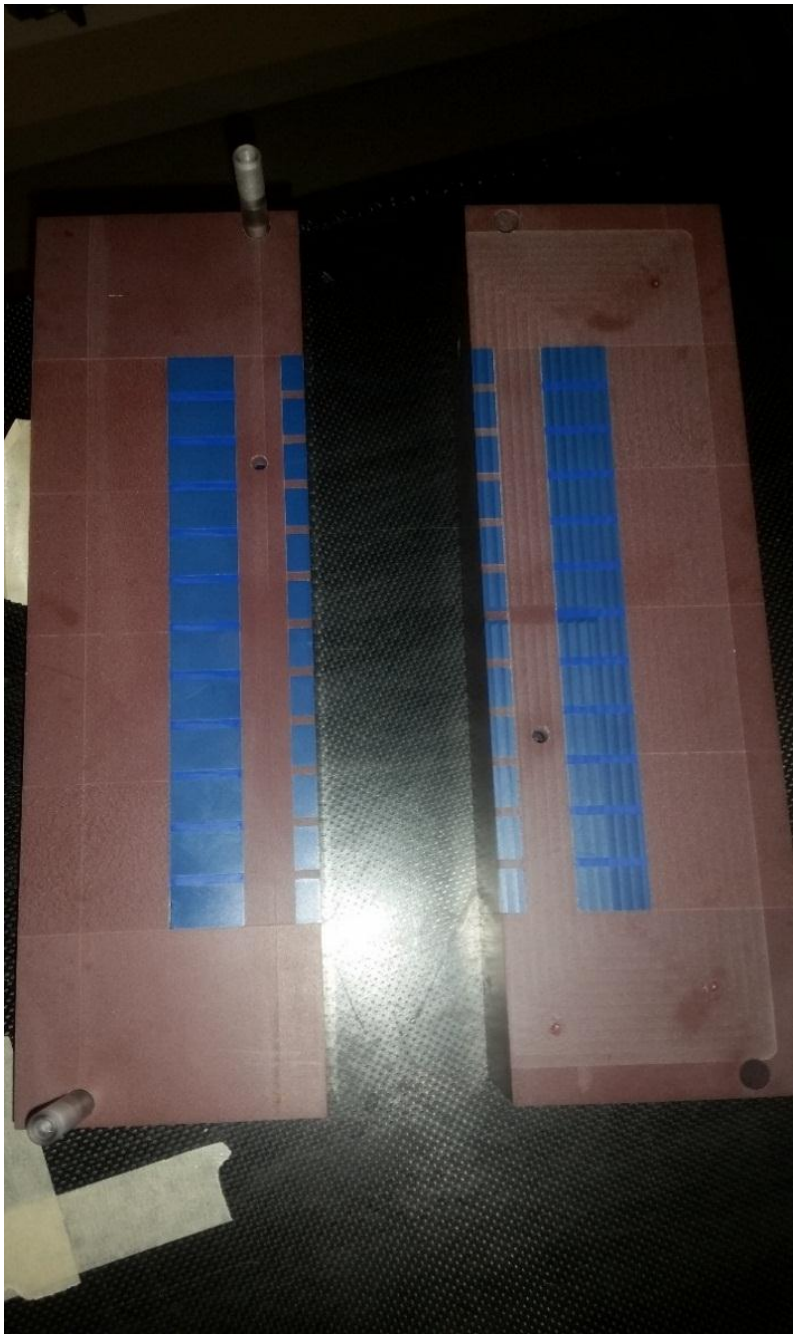

Figure 3.4: Patient Right and Left Pieces of the Phantom

Figure 3.5a shows the coronal diagram of the phantom, representative of the posterior portion of the phantom. This piece only contains the transverse process of each vertebra and also has a varying thickness to simulate patient spinal curvature. Figure 3.5b shows an actual image of this piece and displays the pen pricks in the right superior, left superior and right inferior

positions. Figure 3.6 highlights the diagram and image of the posterior wedged piece of the phantom with corresponding maximum dimensions.

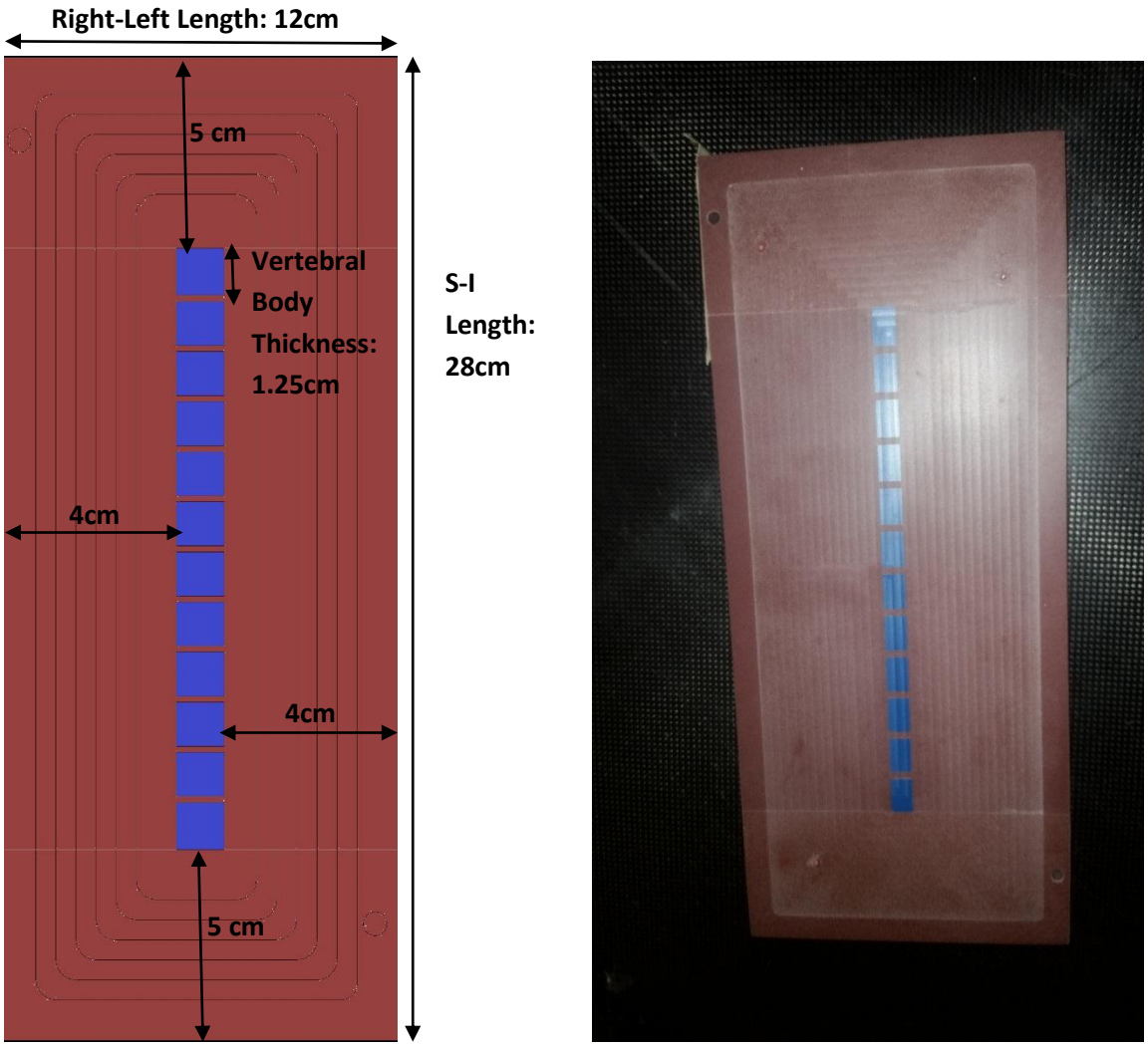

Figure 3.5 Coronal a) Diagram and b) Photo of the Phantom showing the soft tissue (maroon) and bone (dark blue) substitute dimensions.

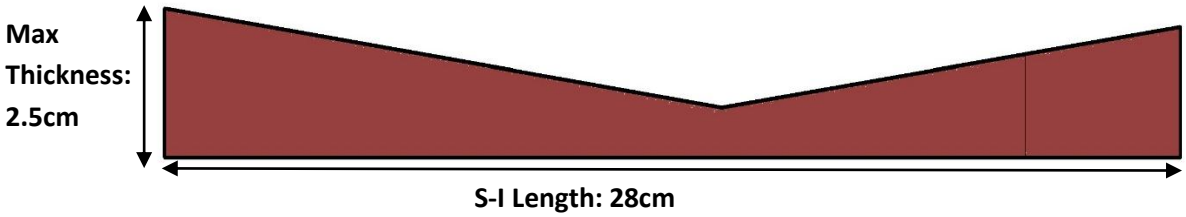

a)

b)

Figure 3.6: Posterior Wedged Piece a) Diagram with Dimensions and b) Photograph

3.3 Film Calibration

The film calibration curve is shown in Figure 3.7.

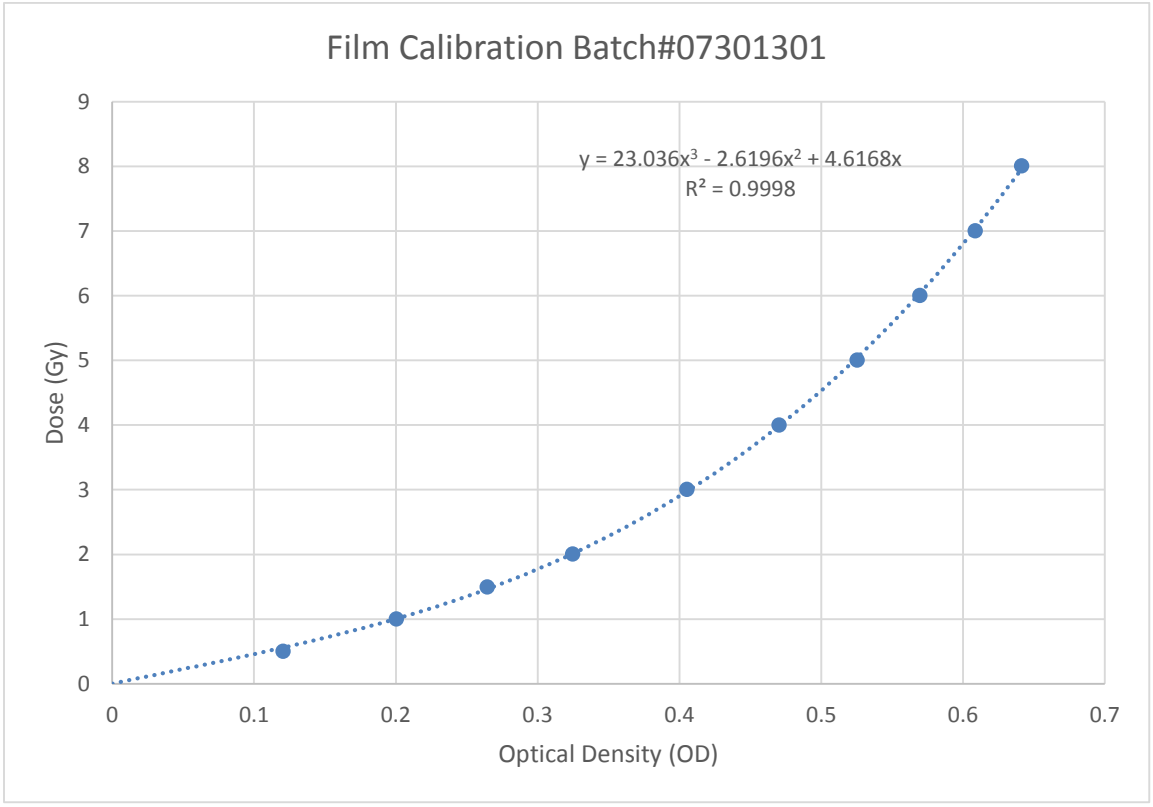

Figure 3.7 Film Calibration Curve for Batch #07301301

The equation used for the optical density to dose conversion in CERR is:

$$Dose = 23.036\,(OD)^3 - 2.6196\,(OD)^2 + 4.6168\,(OD) \qquad \textbf{Equation 3.1}$$

The optical density used to determine the points on the curve was an average of three measurements. The largest standard deviation observed between OD measurements was approximately 1.2%.

3.4 Passive Scattering Dosimetric Analysis

3.4.1 Absolute Dose

The measured TLD dose was compared to the dose calculated by Eclipse. The calculated dose to each TLD location was determined based on the mean dose to a contour of the TLD capsule in the TPS and used for all absolute dose calculations. The expected dose to the right superior TLD and left inferior TLD was 610.2 cGy CGE and 617.9 cGy CGE, respectively. The values for the measured and calculated absolute doses, along with the ratio between the two dose values are listed in Table 3.4.

Passive Scatter TLD Absolute Dose Results				
Irradiation Trial #	TLD Location	Calculated TPS Dose (cGy-RBE)	Measured TLD Dose (cGy-RBE)	Measured/ Calculated
1	Right Superior	610.2	616.0	1.009
1	Left Inferior	617.9	628.4	1.017
2	Right Superior	610.2	612.9	1.004
2	Left Inferior	617.9	625.2	1.012
3	Right Superior	610.2	618.9	1.014
3	Left Inferior	617.9	629.4	1.019

Table 3.5 Passive Scatter Irradiation Absolute Dose Results

The evaluation criterion for the TLD point dose was that the measured dose should be within ±5% of the expected dose. The measured TLD results were all within 2%, successfully passing this evaluation segment.

The coefficient of variation was calculated as a part of a reproducibility study. Three irradiations of the same plan and setup were conducted to determine whether this phantom experiment could be easily recreated. The measured physical dose from this was averaged over 3 trials and the mean divided by the standard deviation of these measurements was compared to the tolerance value. The reproducibility results were less than 0.5%, passing the 3% tolerance criterion. This suggests that if institutions correctly setup the phantom per IROC Houston instructions, the irradiations should produce similar results.

Coefficient of Variation Calculations		
TLD Location	Right Superior	Left Inferior
Average TPS Calculated RBE Dose	610.2	617.9
Average Measured RBE Dose	615.9	627.7
Measured/Calculated Ratio	1.009	1.02
Standard Deviation	3.0	2.2
COV (%)	0.5	0.4

Table 3.6 Passive Scatter Irradiation Reproducibility Study Results

3.4.2 2D Gamma Analysis

The dose distributions from the film and the treatment planning system were compared for analysis after the 2D and 3D registrations were complete. The 2D RMS error for the film was in the range of 0.5-1.0 mm, while the 3D RMS error was in a range of 1.3-1.6 mm. A 2D gamma analysis was formed on each trial data set. The hypothesis used a passing criterion of ±5%/3mm. Additionally, a second analysis was performed using a ±5%/5mm for comparison. An example of the gamma analysis color map produced by CERR is shown in Figure 3.8. A blue or green pixel returns a gamma value less than 1 and is considered a passing pixel.

Yellow, orange and red pixels return gamma values greater than 1, which is considered not meeting the criteria. The results from the 2D gamma analysis for the passive scatter irradiations are listed in Table 3.7.

a) 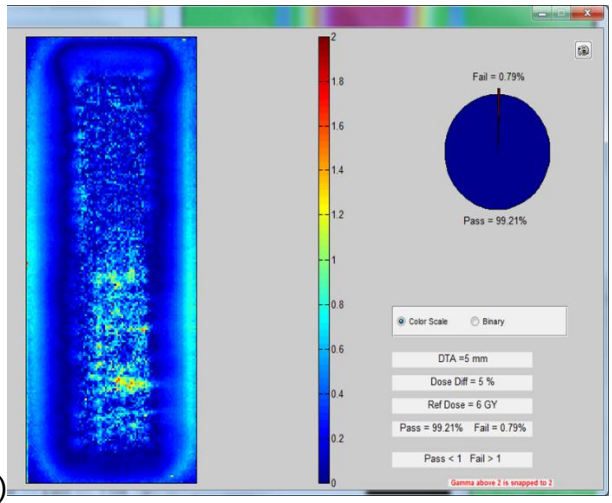

b) 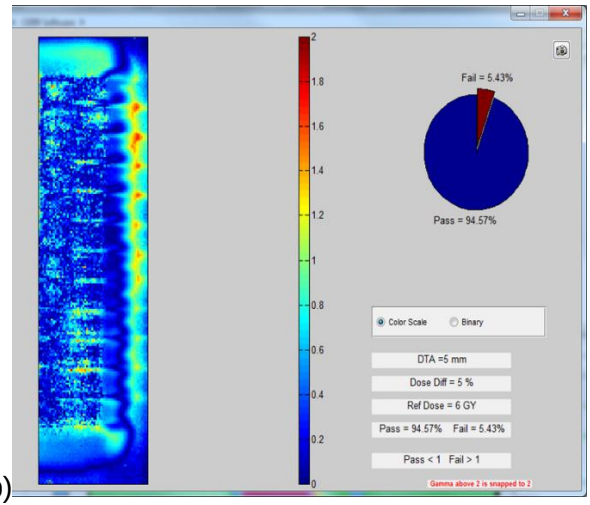

Figure 3.8 2D Gamma Analysis Color Maps from Passive Scattering Trial 2 data in the a) coronal and b) sagittal planes for the 5%/5mm criteria

5%/5mm Passing Criteria			5%/3mm Passing Criteria		
Trial	Coronal	Sagittal	Trial	Coronal	Sagittal
1	99%	81%	1	96%	67%
2	99%	95%	2	99%	85%
3	99%	94%	3	95%	90%

Table 3.7 2D Gamma Analysis Passing Rates for Passive Scattering Trials

Following the stated passing pixel rate in the hypothesis of 85%, each coronal plane passed the 5%/5mm and the 5%/3mm criteria. Trials 2 and 3 in the sagittal plane also passed both criteria successfully. Trial 1 in the sagittal plane failed both criteria. It is expected that the 5%/5mm criteria would show a higher pass rate compared to the stricter criteria, as this allows for more disparity between the compared distributions; this was observed. For both sets of criteria, the coronal plan had better passing rates compared to the sagittal plane. This could be due to this film being placed parallel to the beam axis, making it a harder plane to pass as the

linear energy transfer (LET) increases in this direction. Additionally, on the sagittal films, there was consistent failure seen in the distal fall off region and in the superior and inferior directions outside the CTV, possibly due to the increase in LET at the end of the range and scatter from the field edges of the aperture, respectively. For the coronal films, most failure is observed in the lower spine field in the CTV and on the right film edge. Based on these results, the 5%/5mm gamma analysis is the more suitable criteria for this phantom. This criteria is partially consistent with the criteria used for the current anthropomorphic proton spine phantom at IROC-H.

3.4.3 Profile Analysis

The dose profiles at various positions were plotted in all three directions of the phantom. The coronal film is used for the right-left alignment profiles and for the cold spot peak profile. The sagittal film not only verified the range, hot spot location and determined how conformal the dose delivered was, but also allowed for observation (through the anterior-posterior profiles and DTA measurements) of dose matching at the heterogeneous interfaces. The sagittal plane films clearly show the extended proton range at each individual cartilage disk due to the change in the stopping power between the three tissue substitutes. An example of the coronal and sagittal films, along with the respective locations of the profiles is shown in Figure 3.9.

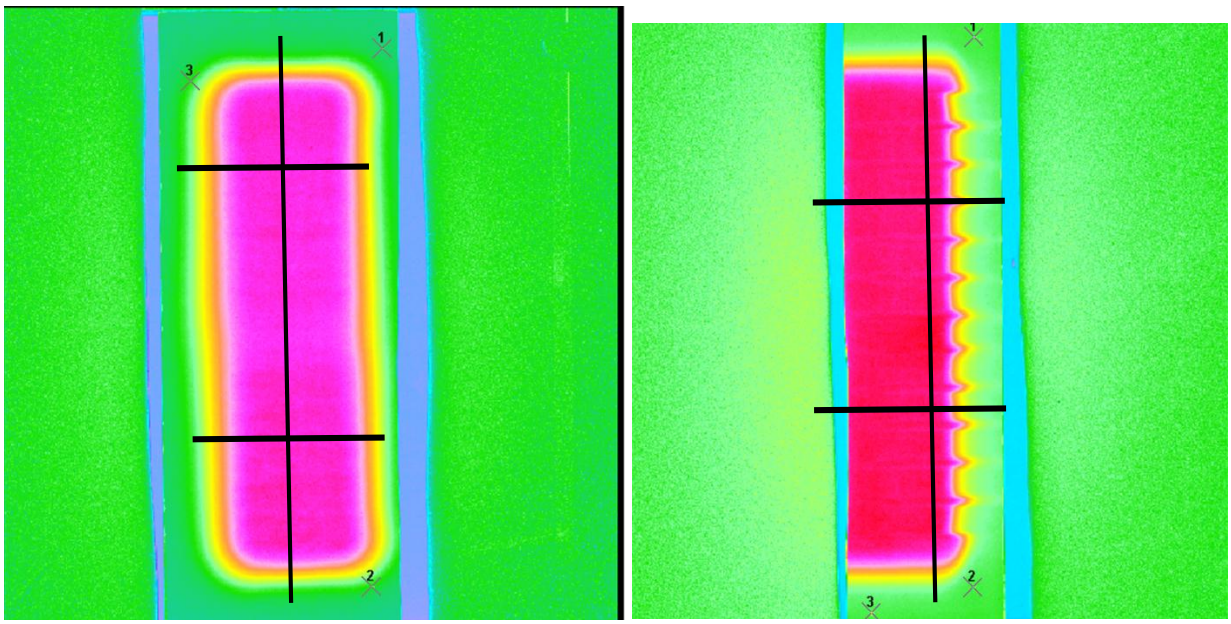

Figure 3.9: Images of the digitized film in the a) coronal and b) sagittal planes for Passive Scattering Trial 3. The black lines represent the locations where dose profiles were acquired.

The average data from the distance to agreement measurements and percent dose differences at the hot/cold spot peaks is shown in Table 3.8. An example of the right-left, anterior-posterior, and superior-inferior profiles for Trial 3 are shown in Figures 3.10-3.15. For the field displayed in Figure 3.9, more disagreement is displayed on the left gradient region. In Figure 3.10, more disagreement is displayed in the right gradient region. Observed in the anterior-posterior film profiles (Figures 3.12 and 3.13) are under-responses in the distal fall off region and over-responses past the end of the range. Possible explanations for these phenomena will be explored in Section 3.5.

Film Plane	Avg. Distance to Agreement	SD (mm/%)	Criteria
Coronal R/L Agreement-Sup.	2.1 mm	0.2	5mm
Coronal R/L Agreement-Inf.	1.0 mm	0.3	5mm
Sagittal A/P Agreement-Sup.	1.3 mm	0.8	5mm
Sagittal A/P Agreement-Inf.	1.0 mm	0.3	5mm
Coronal S/I Junction Shift	1.8 mm	1.7	5mm
Sagittal S/I Junction Shift	3.0 mm	0.3	5mm
% Dose Difference-Coronal	2.0%	1.5	7%
% Dose Difference-Sagittal	1.2%	0.9	7%

Table 3.8 Passive Scattering Trials Average Distance to Agreement Results

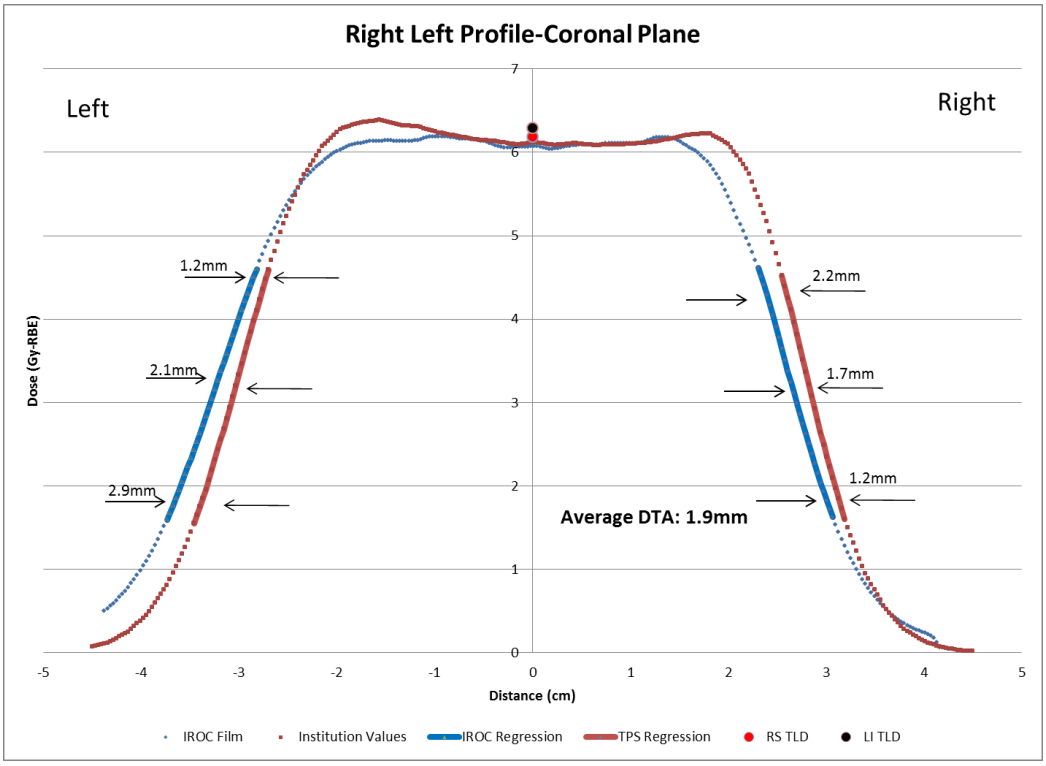

Figure 3.10 R-L Dose Profile for the passive scattering trial 3 upper spine field, measured in the coronal Plane

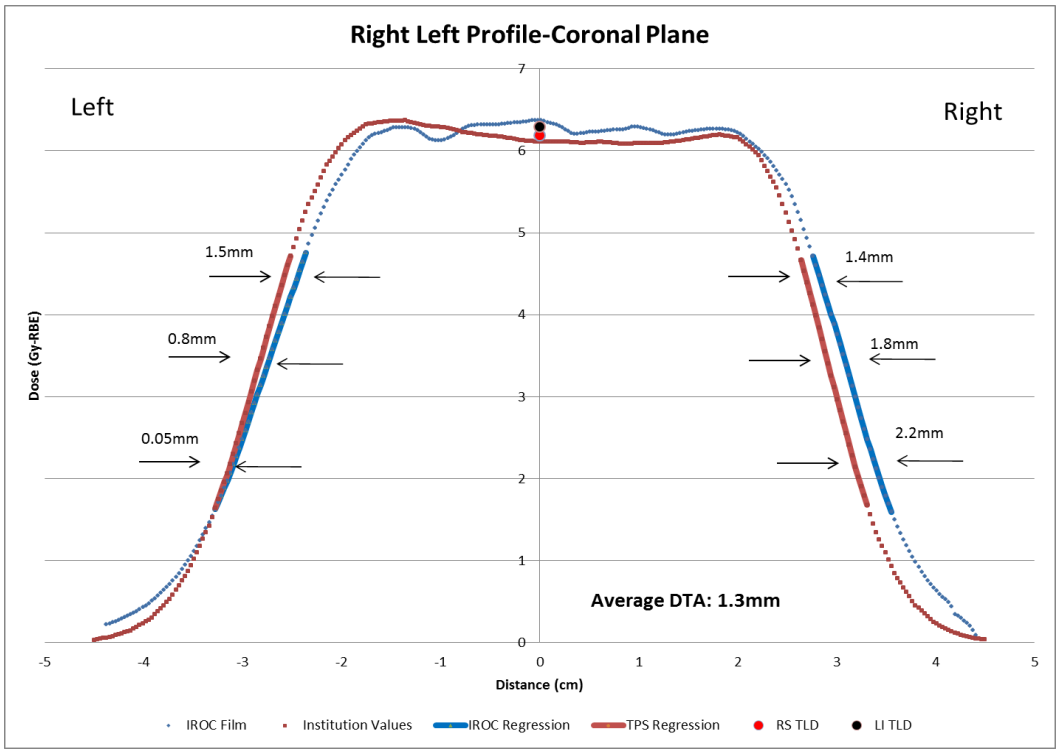

Figure 3.11 R-L Dose Profile for the passive scattering trial 3 lower spine field, measured in the coronal Plane

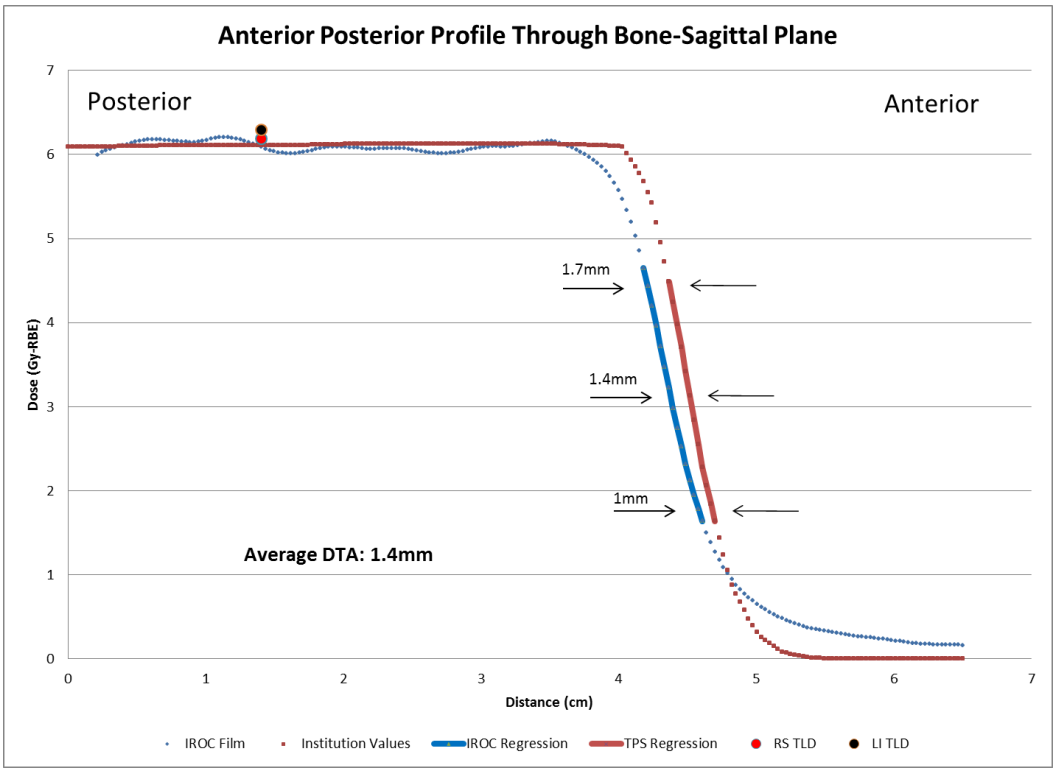

Figure 3.12 A-P Dose Profile for the passive scattering trial 3 upper spine field, measured in the Sagittal Plane

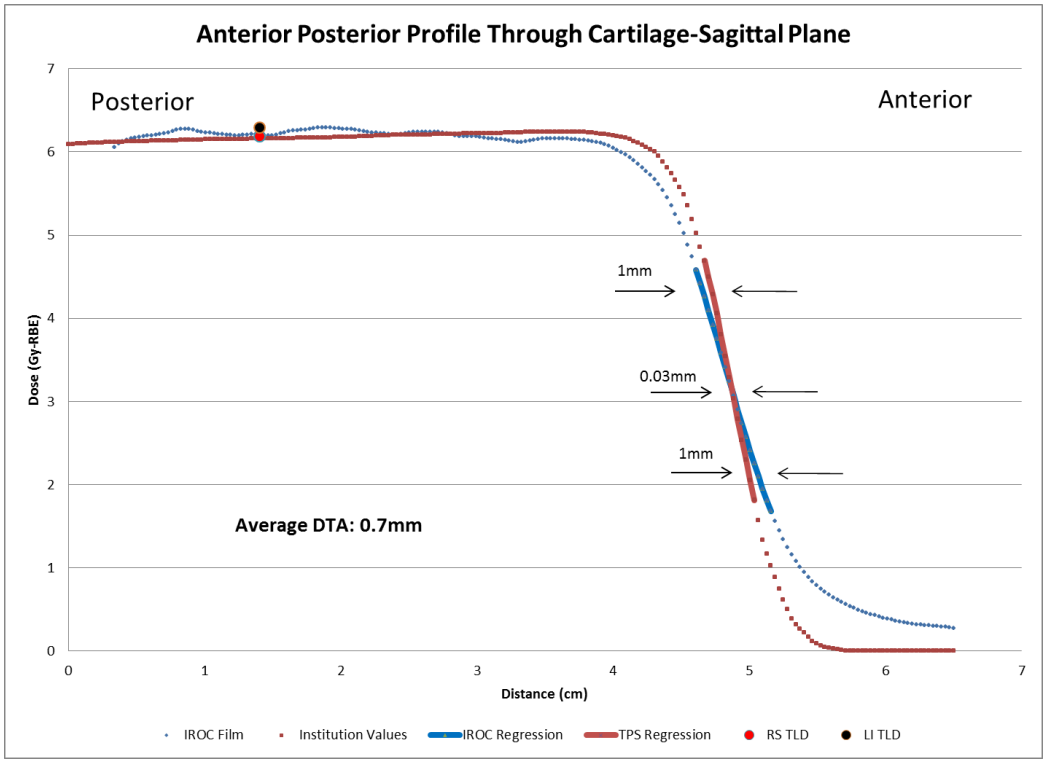

Figure 3.13 A-P Dose Profile for the passive scattering trial 3 lower spine field, measured in the sagittal Plane

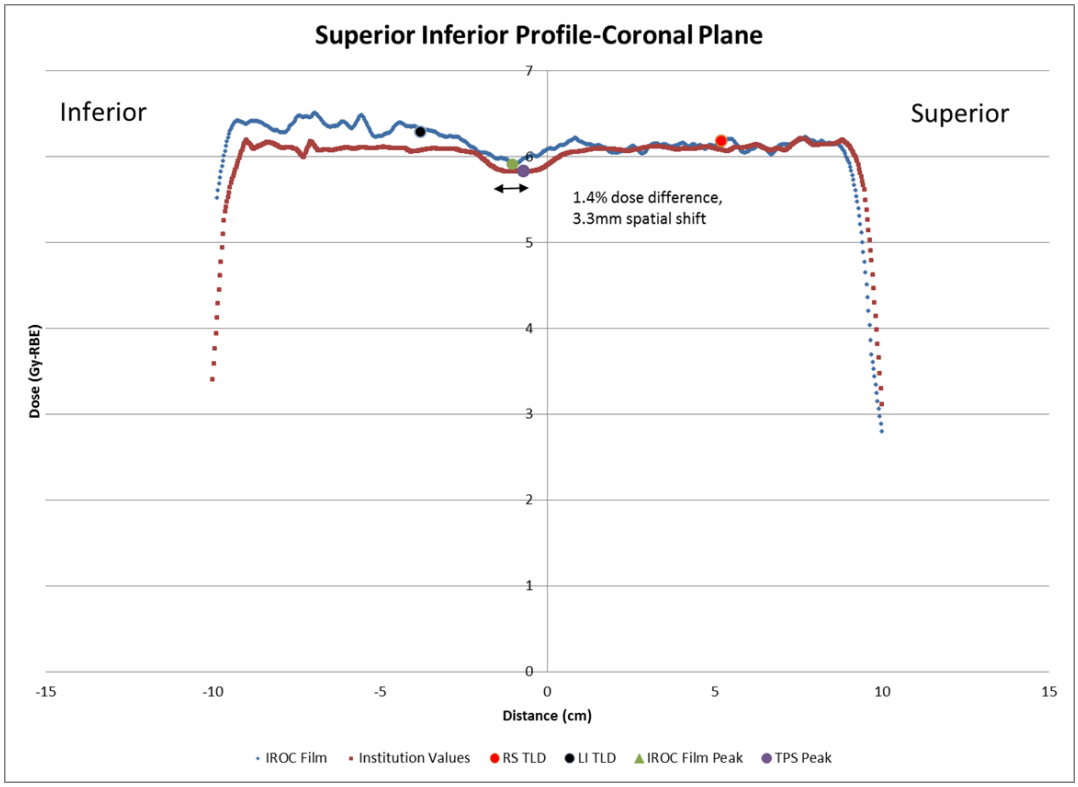

Figure 3.14 S-I Dose Profile for the passive scattering trial 3 measured in the coronal Plane

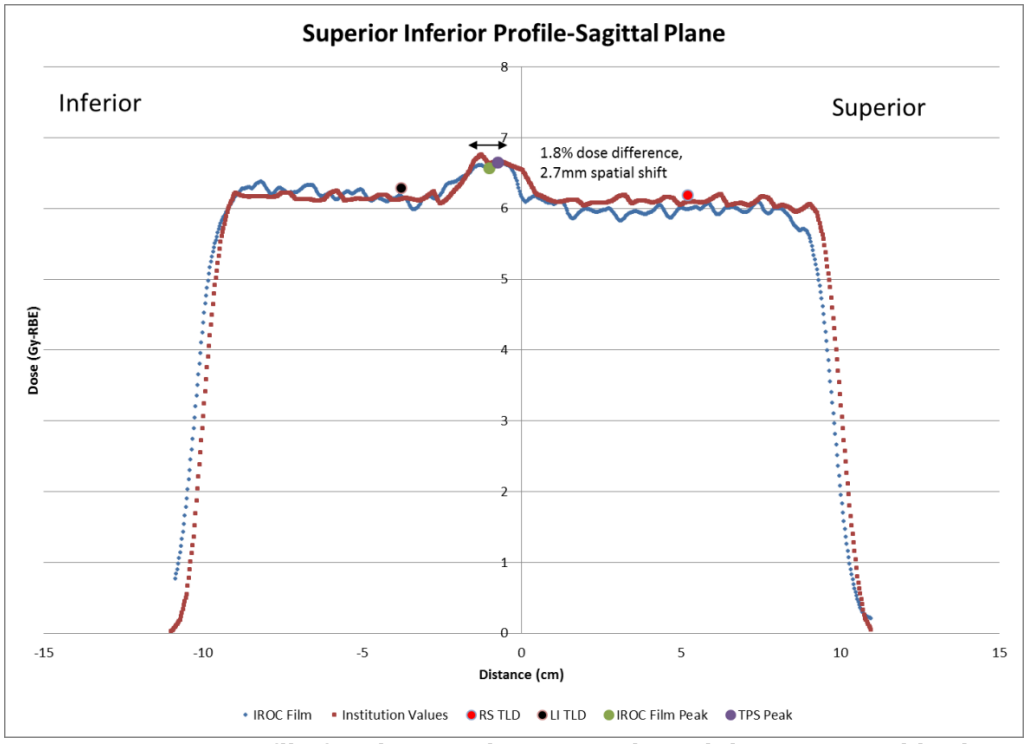

Figure 3.15: S-I Dose Profile for the passive scattering trial 3 measured in the sagittal Plane

Based on the average data presented above, the phantom passed all criteria for the experimental evaluation. Individually, all profiles acquired in the coronal and sagittal planes passed criteria. The remaining profiles acquired from the coronal and sagittal planes are shown in the appendix.

The standard deviations for the junction shift DTA measurements are largest, with a maximum over 3mm. All other deviations are between approximately 1-2mm, suggesting that the DTA trends were consistent over all profiles.

3.5 Spot Scanning Dosimetric Analysis

3.4.1 Absolute Dose

The dose measured in the TLD irradiated using a spot scanning beam was compared to the TLD dose calculated by Eclipse. The calculated dose to each TLD was averaged in the same manner as the passive scatter irradiations. The expected dose to the right superior TLD and left inferior TLD was 611.4 cGy CGE and 604.6 cGy CGE, respectively. The values for the measured and calculated absolute doses, along with the ratio between the set of measurements is listed in Table 3.9.

Spot Scanning TLD Absolute Dose Results				
Irradiation Trial #	TLD Location	Calculated TPS Dose (cGy CGE)	Measured TLD Dose (cGy-CGE)	Measured/ Calculated
1	Right Superior	617.4	629.2	1.019
1	Left Inferior	617.3	577.5	0.935
2	Right Superior	617.4	628.5	1.017
2	Left Inferior	617.3	574	0.929
3	Right Superior	617.4	628.5	1.017
3	Left Inferior	617.3	577.1	0.934

Table 3.9 Spot Scanning Irradiation Absolute Dose Results

The evaluation criterion for the TLD point dose was that the measured dose should be within ±5% of the expected dose. The measured right superior TLD results were consistently higher than the planned doses and all results are within 3%, successfully passing. The measured left inferior TLD results were lower than the planned doses and did not pass criteria.

The coefficient of variation results for the spot scanning irradiations are listed in Table 3.10. The reproducibility results were less than 0.5%, suggesting that correct setup of the phantom will yield accurate results, regardless of the beam delivery technique.

Coefficient of Variation Calculations		
TLD Location	Right Superior	Left Inferior
TPS Calculated RBE Dose	617.4	617.3
Measured RBE Dose	628.4	575.9
Measured/Calculated Ratio	1.018	0.933
Standard Deviation	0.4	1.9
COV (%)	0.1	0.3

Table 3.10 Spot Scanning Irradiation Reproducibility Study Results

3.5.2 2D Gamma Analysis

The spot scanning dose distributions from the film and TPS were compared for analysis. The 2D RMS error for the film was in a range of 0.5-1.0mm, while the 3D RMS error was in a range of 1.3-1.4 mm. The gamma analysis was performed for the passing criteria of 5%/5mm and 5%/3mm. The spot scanning gamma analysis color map with criteria of 5%/5mm is shown in Figure 3.16. The results from the 2D gamma analysis for the spot scanning irradiations are listed in Table 3.11.

a) 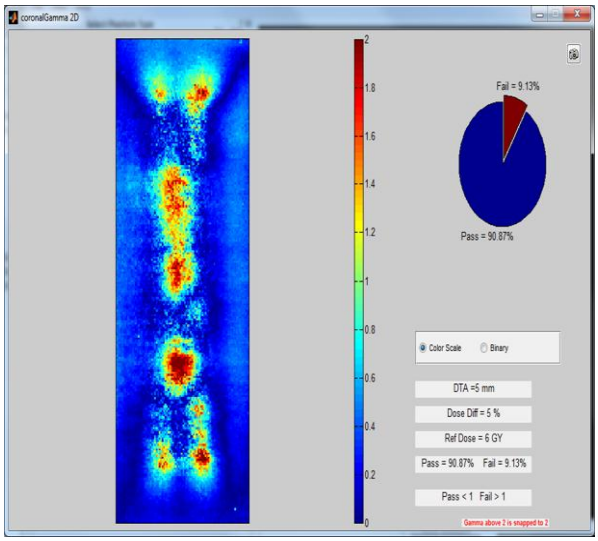

b) 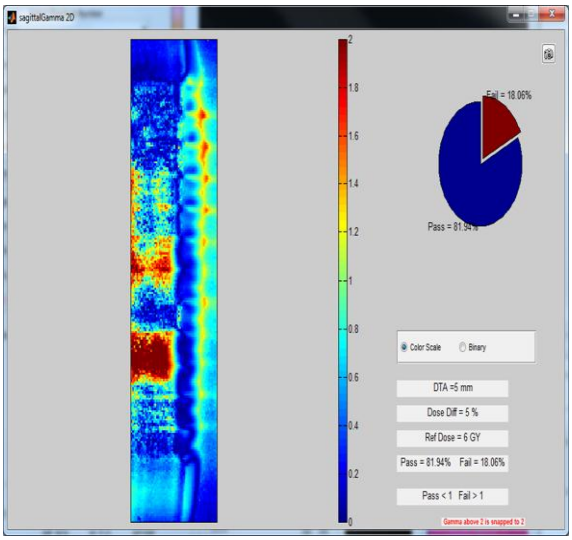

Figure 3.16 2D Gamma Analysis Color Maps from Spot Scanning Trial 1 data in the a) coronal and b) sagittal planes for 5%/5mm criteria

5%/5mm Passing Criteria			5%/3mm Passing Criteria		
Trial	Coronal	Sagittal	Trial	Coronal	Sagittal
1	91%	82%	1	86%	72%
2	91%	82%	2	88%	73%
3	91%	84%	3	79%	77%

Table 3.11 2D Gamma Analysis Passing Rates for Spot Scanning Trials

Following the stated passing pixel rate in the hypothesis of 85%, only the coronal plane had all three trials meet this objective for the 5%/5mm criteria. Trial 3 of the coronal planes failed the 5%/3mm criteria. None of the six gamma analyses calculated in the sagittal plane passed for either criteria. Failure is observed in the middle of the CTV for all the spot scanning gamma color maps. Additionally, the same failure at the end of the range observed during the scattered beam analyzes is observed for spot scanning. As seen in the passive scattering irradiations, the 5%/5mm criteria showed a higher pass rate as expected. For both sets of criteria, the coronal plan had better passing rates compared to the sagittal plane.

3.5.3 Profile Analysis

The dose profiles were plotted in all directions of the phantom and most were acquired approximately in the same locations as those for the passive scattering irradiations. The superior-inferior profile on the sagittal plane was moved slightly away from the edge of the range. An example of the coronal and sagittal films, along with the respective locations of the profiles is shown in Figure 3.17.

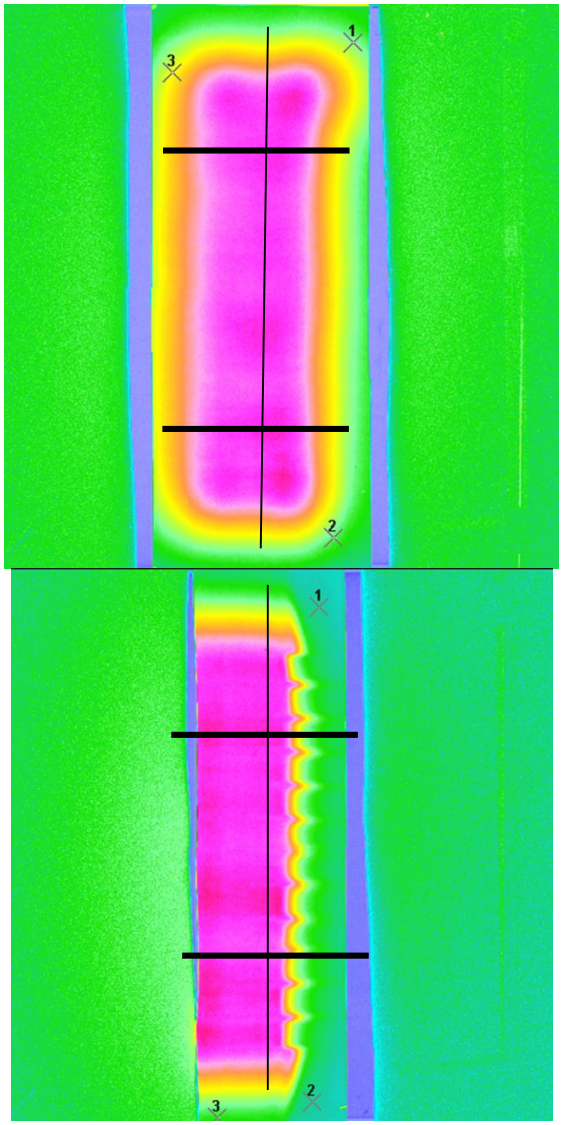

Figure 3.17 Images of the digitized film in the a) coronal and b) sagittal planes for Spot Scanning Trial 3. The black lines represent the locations where dose profiles were acquired.

The average DTA measurements are shown in Table 3.12. Figures 3.18-3.22 shows the profiles acquired for trial 3, which had an average performance over all measurements. Figures 3.18 and 3.19 display a more gradual fall off in the high dose region compared to the scattered beam profiles. Also, there is more disagreement on the right side compared to the left side for both profiles. Figure 3.20 not only displays a similar under response in the distal fall off region and over response past the target volume for the film profile, but also displays a large under response in the SOBP region. Each profile acquired through the cartilage substitute exhibited this discrepancy (see Appendix), with up to a 10% response lower compared to the TPS. This effect was not as prominent for A-P profiles acquired through the bone. All profiles passed the DTA criteria, but the spot scanning plan junction could not be evaluated in the same manner as the passive scattering plan junction.

Film Plane	Avg. Distance to Agreement (mm)	SD (mm)	Criteria
Coronal R/L Agreement-Superior Field	2.0	0.7	5mm
Coronal R/L Agreement- Inferior Field	2.4	0.7	5mm
Sagittal A/P Agreement-Superior Field	0.4	0.3	5mm
Sagittal A/P Agreement-Inferior Field	0.7	0.2	5mm
Coronal S/I Junction Shift	N/A	N/A	5mm
Sagittal S/I Junction Shift	N/A	N/A	5mm
% Dose Difference-Coronal	N/A	N/A	7%
% Dose Difference-Sagittal	N/A	N/A	7%

Table 3.12 Spot Scanning Trials Average Distance to Agreement Results

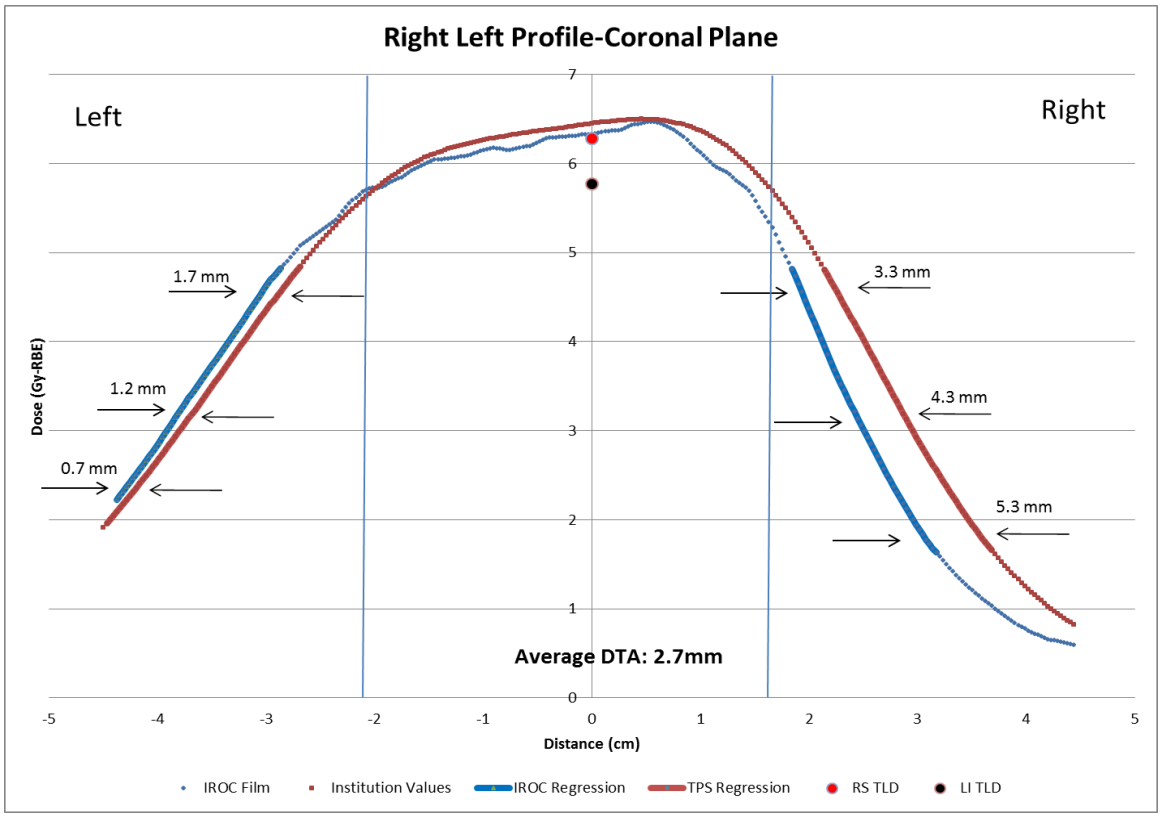

Figure 3.18 R-L Dose Profile for the Spot scanning trial 3 upper spine field, measured in the coronal Plane

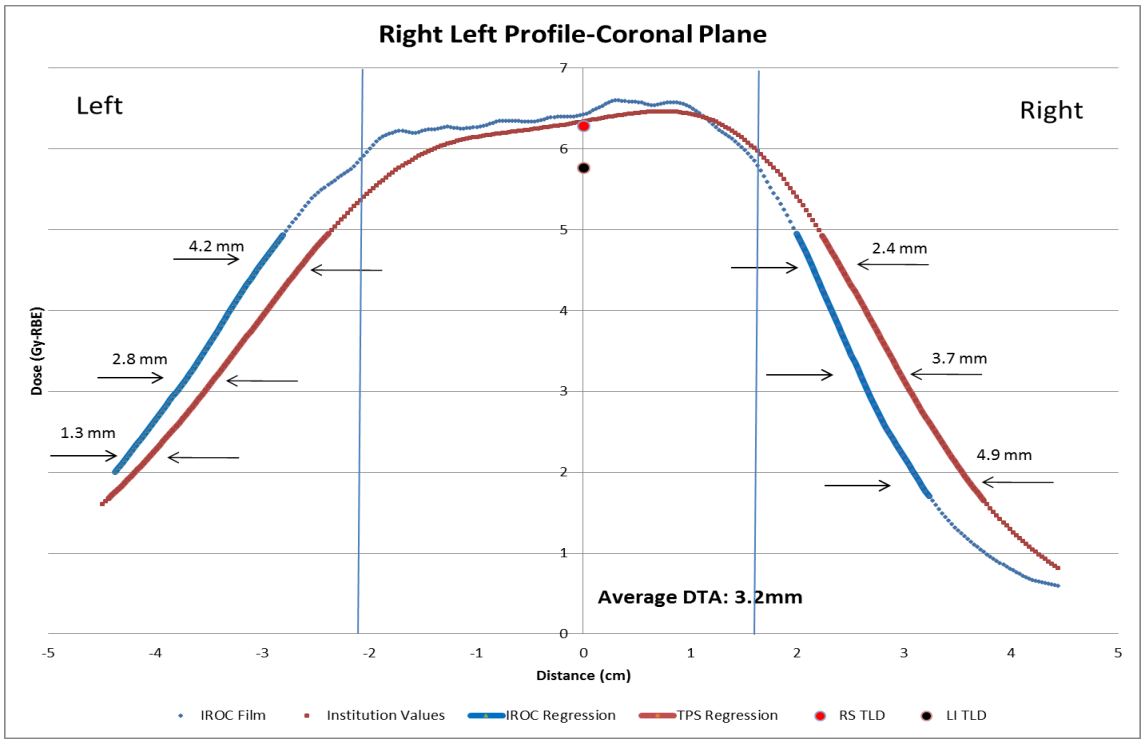

Figure 3.19 R-L Dose Profile for the Spot scanning trial 3 lower spine field, measured in the coronal Plane

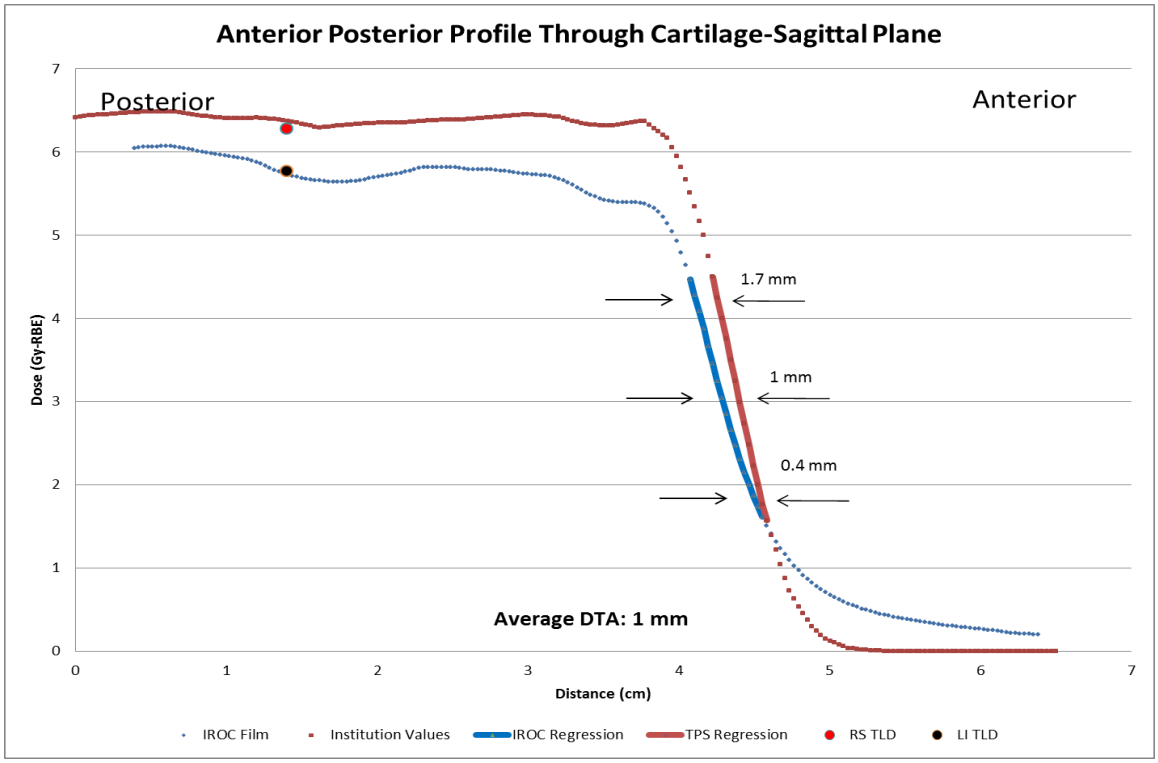

Figure 3.20 A-P Dose Profile for the Spot scanning trial 3 lower spine field, measured in the Sagittal Plane

Quantitative evaluation of the junction shift was unable to be determined. Spot scanning junctions do not have gaps at the patient surfaces and matches a certain depth like traditional junctions, so the TPS profile data doesn't show a comparison peak. Additionally, the substantial variation in the film dose distribution does not reveal any defined peaks, further increasing the difficulty for junction analysis. The variations in the film profile explain the gamma analysis failure regions on the sagittal film, especially in the inferior direction (See Figure 3.21). This clearly shows a discrepancy in the predicted dose by the planning system and the measured dose.

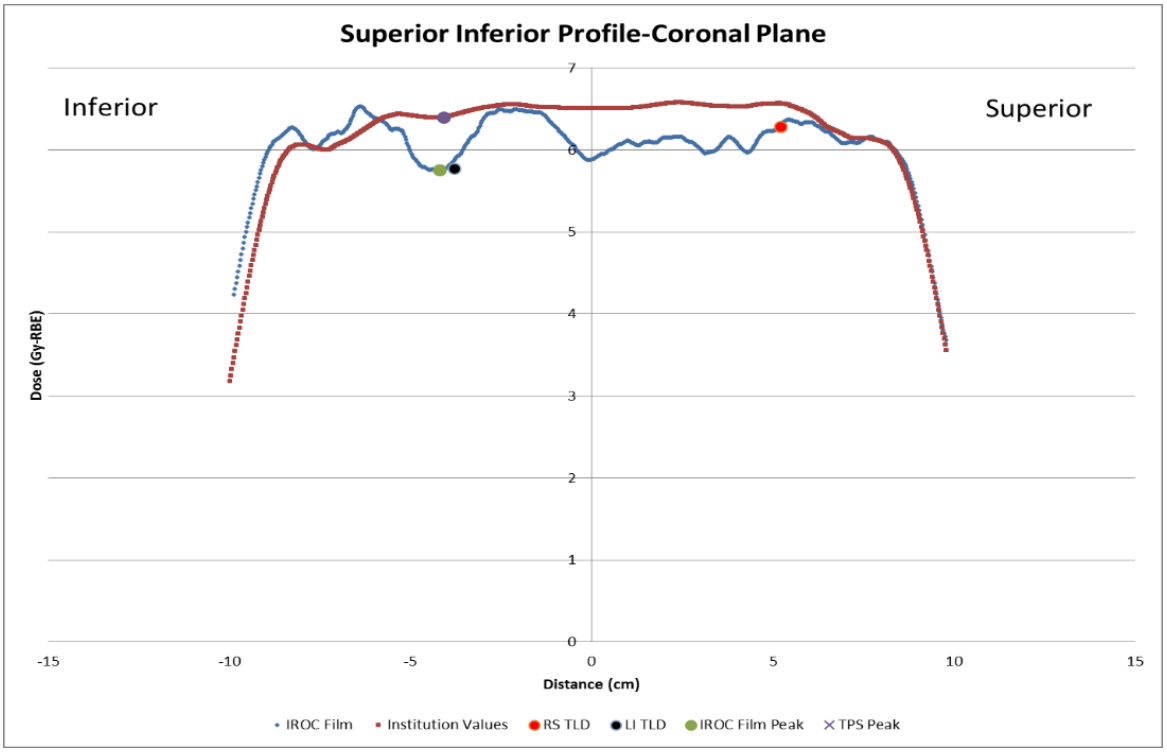

Figure 3.21 S-I Dose Profile for the Spot scanning trial 3, measured in the coronal Plane

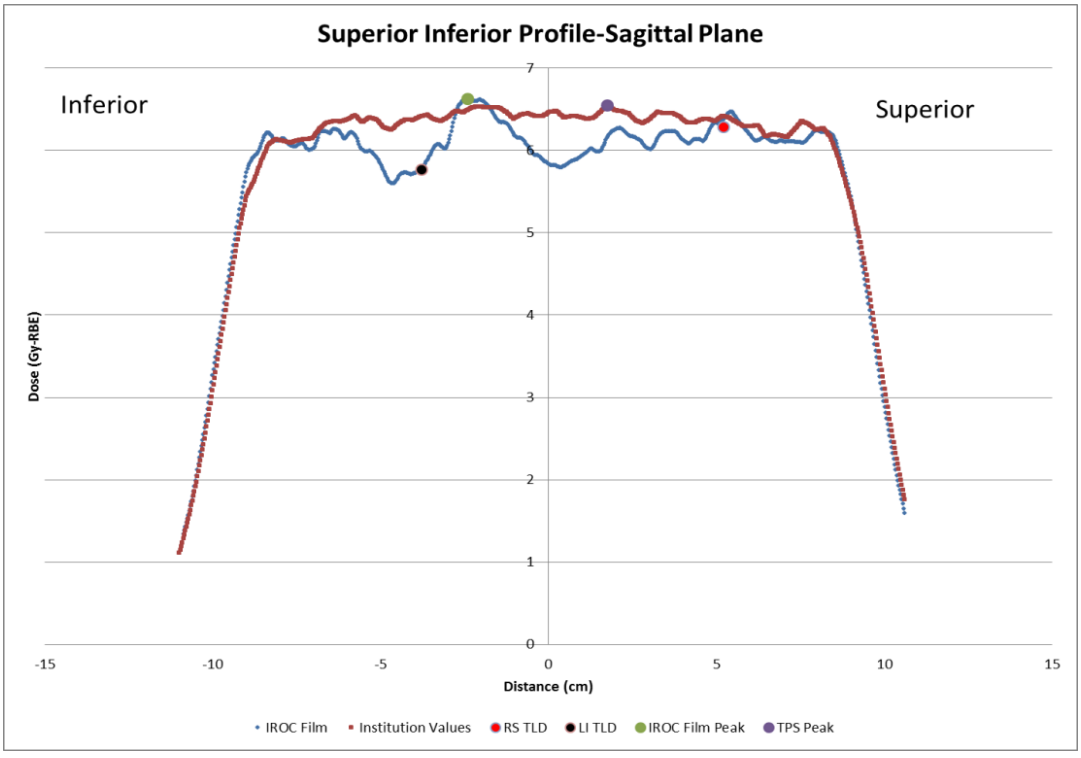

Figure 3.22 S-I Dose Profile for the Spot scanning trial 3, measured in the sagittal Plane

Based on the average data presented above, the phantom quantitatively passes all DTA criteria for the experimental evaluation, despite the qualitative issues observed. The standard deviations are less than 1mm, suggesting that the DTA trends were similar over all profiles.

3.6 Beam Delivery Dosimetric Analysis Comparison

Quantitatively, the DTA results from the passive scattering and spot scanning irradiations are comparable. However, it is very apparent that the passive scattering irradiations produced better results. Two of the 12 total gamma calculations conducted from the passive scattering irradiations failed, while 7 of the 12 calculated failed for the spot scanning measurements. The measured/calculated TLD ratios for passive scattering were all within 2%. The ratios for the right superior TLD from the spot scanning technique did pass the 5% tolerance, but the results for the left inferior TLD did not. The average distance to agreement in the right, left, anterior and posterior directions was comparable between both beam delivery techniques. Overall, the DTA was less than 3mm in these directions with a standard deviation of less than 1mm for all measurements. As previously mentioned, the junction was not able to be quantitatively evaluated from the spot scanning irradiations. Therefore, no dosimetric comparison between the techniques can be completed. A summary of the all phantom evaluation results is listed in Table 3.13.

	Passive Scattering		Spot Scanning	
	Average	Worst	Average	Worst
Right Superior TLD	1.009	1.014	1.028	1.029
Left Inferior TLD	1.016	1.019	0.932	0.929
5%/5mm Gamma Analysis	95%	81%	87%	82%
5%/3mm Gamma Analysis	89%	67%	79%	72%
Right/Left DTA (mm)	2.1/1.0	2.3/1.0	2.0/2.4	2.7/1.3
Anterior/Posterior DTA (mm)	1.3/1.0	2/1.1	0.4/0.7	0.6/1.0
Coronal/Sagittal Junction Shift	1.8/3.0	3.3/3.3	N/A	N/A
% Dose Difference-Coronal	2.0	3.6	N/A	N/A
% Dose Difference-Sagittal	1.2	1.8	N/A	N/A

Table 3.13 Comprehensive Summary of Phantom Experiment Results

Two characteristics seen in the right, left, anterior and posterior profiles were the under-estimation of dose in the SOBP and the over-estimation of the tail energy. An example of these effects is shown in Figure 3.23.

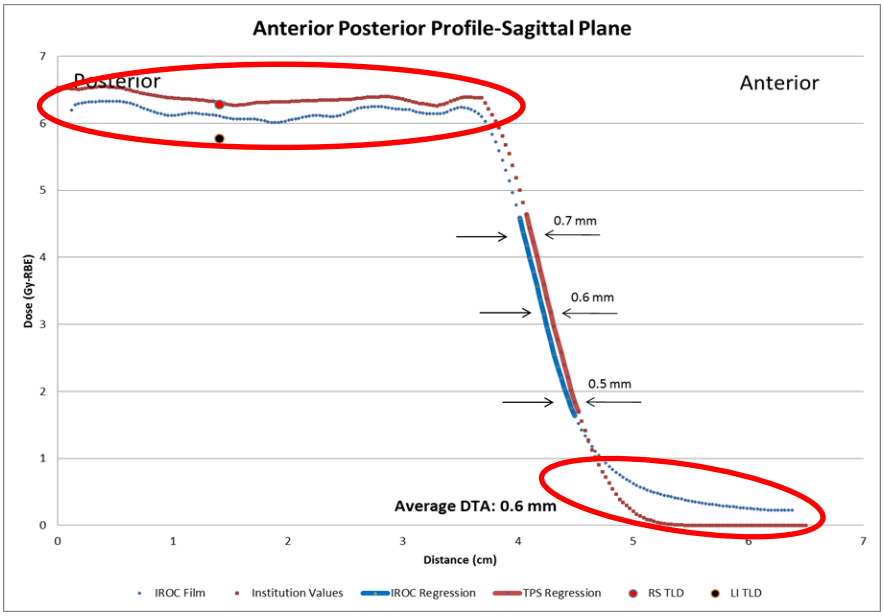

Figure 3.22: A-P Spot Scanning Dose Profile for upper spine field in Trial 3, highlighting the under response in the SOBP and the over response in the low dose region

These responses were seen for both delivery techniques, possibly due to the film's sensitivity to high LET radiation [42]. With the increase in the LET in the SOBP at the end of the range, a quenching effect occurs. Darkening of the film saturates and the increase in LET does not lead to an increase in the dose response. This under-response in the SOBP ranges anywhere from 5-40% in previous studies for a variety of radiochromic films types [43, 44]. Additionally, residual energy is observed in the film profiles at the end of the range due to secondary neutrons from nuclear interactions. These secondary particles also have a high LET that causes variation in the film profiles, leading to dose deposition outside the target [18].

The passive scattering results deemed it acceptable for send-off to an institution that conducts similar beam deliveries. Based on the results, it is best to use the 5%/5mm gamma analysis criteria with 85% of pixels passing. The DTA criteria of 5mm in all directions, along with no more than a 5mm spatial shift or a 7% dose difference at the junction were shown to be suitable criteria for the passive scattering deliveries. Some of these criteria, such as the DTA criteria and the percent dose difference at the junction, could be stricter than what was evaluated.

More testing will need to be conducted on the phantom with spot scanning before the phantom can be used as an auditing tool for this technique. It has been determined that the junction area cannot be evaluated in the same manner as for passive scattering. Therefore, new methods and evaluation metrics need to be explored. Because no trial passed the gamma analysis for both film planes, the possibility of using a different criteria may also need to be explored based on resolution regarding the observed dose variations.

3.7 Investigation of Spot Scanning Delivery Results

With discrepancies more prominently observed for the spot scanning profiles, it was suggested that an issue occurred with the treatment planning system calculations or with the treatment delivery system. In addition to quenching, the dose past the end of the range and problems in the dose calculation algorithms were investigated.

It was suspected that the dose deposited past the target was due to secondary particles that were produced in the phantom from nuclear interactions. Figure 3.24 shows the percent absorbed dose due to secondary particles produced [45]. The dose deposited past the end of the range is less than 0.1% of the total absorbed dose. This percentage would be higher for bone, as it yields the generation of more secondary particles. The profiles from this study showed that the dose deposit outside the target was about 8-10% of the reference dose. So although nuclear fragments may contribute to this over response in the tail, its contribution is rather small.

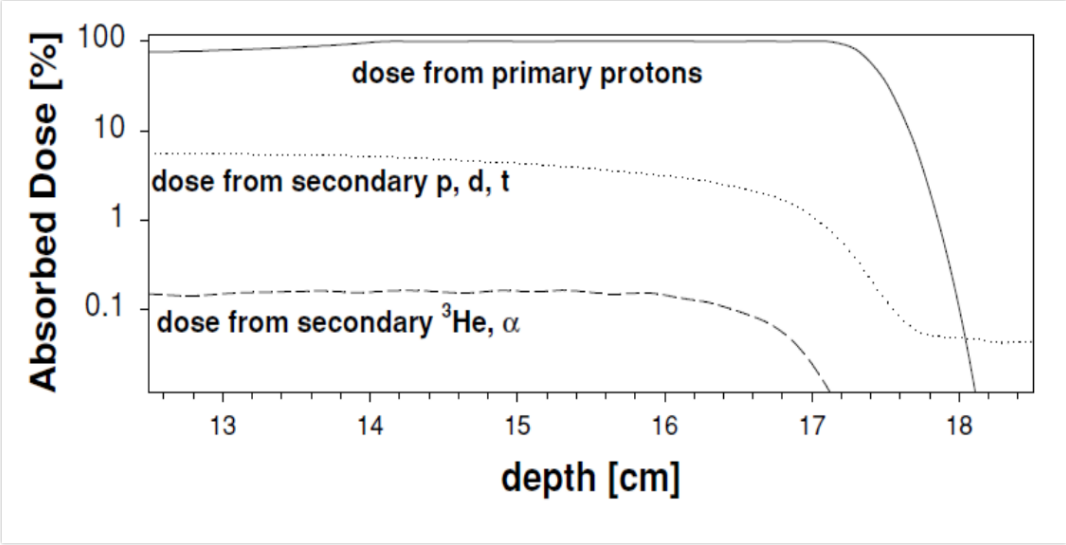

Figure 3.24: (from Paganetti et. al) Percent Dose contributions of secondary particles for a 160 MeV proton beam

Next, the optimization techniques were explored. For multi field optimization, the spots used to create the dose from the 2 fields were simultaneously optimized. Due to differences in the spot intensities, the dose distribution per beam can be very inhomogeneous. And because there are no smearing margins to account for misalignment like with scattered deliveries, the range and setup uncertainties can have a large effect on the dose that is actually delivered.

This effect has been shown in patient cases. Figure 3.25 shows dose distributions comparing the PTV-Based, or non-robust optimized plan, to the robustly optimized plan [46] for a head and neck case. The top row shows the distributions without any uncertainties accounted for in the planning. The bottom row shows how the dose distributions will appear the patient setup was off by 3mm. Comparing the non-robust plans, the bottom image has a very inhomogeneous dose due to the introduced shift in the patient. The robust plans have some changes between the 2 distributions, but there is still adequate target coverage. This possibly relates to the dose variation seen in the spot scanning profiles. But there may be inaccuracies in the dose calculation in the presence of inhomogeneous media which may also have an effect on the results.

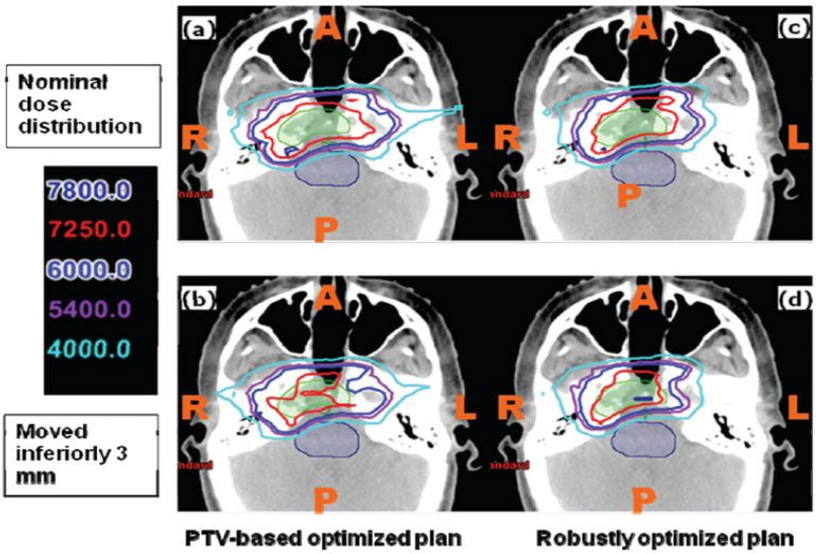

Figure 3.25: (from Liu et. al) Comparison of non-robustly optimized and robustly optimized plans in a head and neck case

The Eclipse treatment planning system uses the same pencil beam algorithm for both passive scattering and spot scanning treatment plans, with the difference occurring in the in-air fluence modeling [47]. Studies have reported that inaccuracies in the dose calculations may occur when an inhomogeneous media is placed in the beam [47, 48]. Figures 3.26a and 3.26b from Yamashita et. al compared pencil beam dose calculations to Monte Carlo calculations. Monte Carlo algorithms are considered the most accurate algorithms to compute dose.

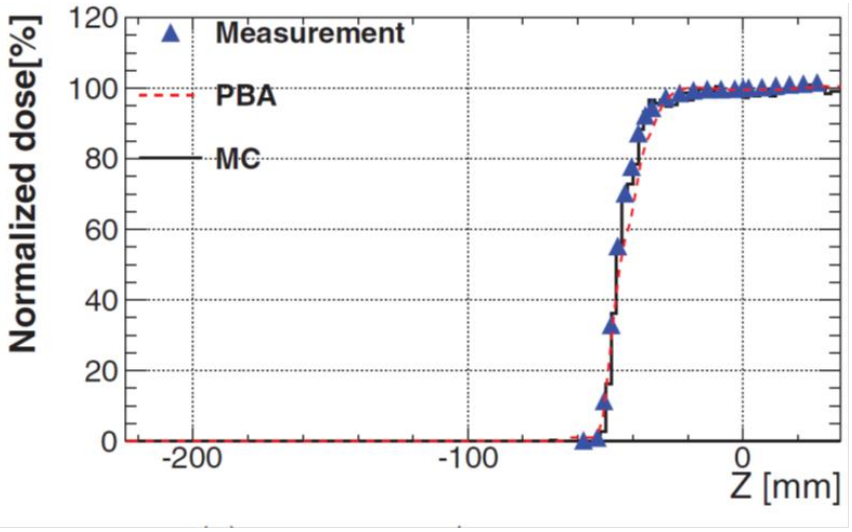

a)

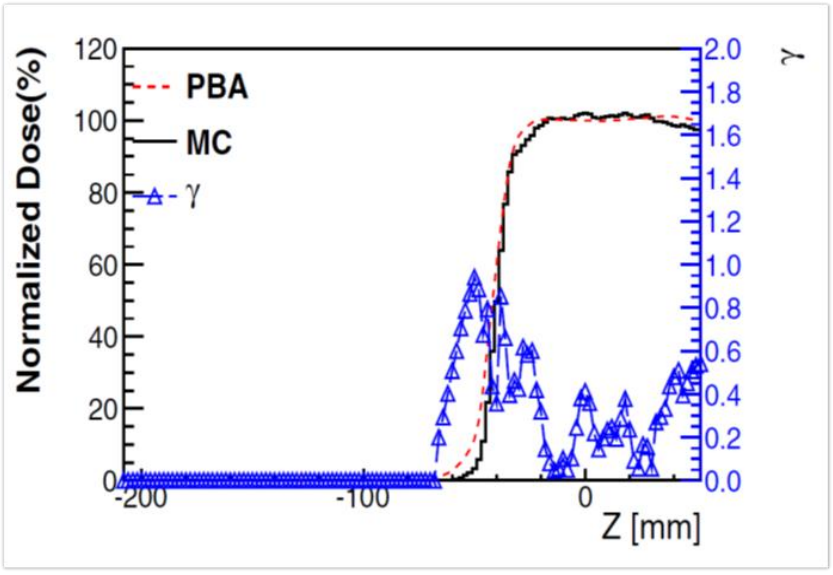

b)

Figures 3.26 (from Yamashita et. al) Comparison of the dose distributions calculated from Pencil Beam and Monte Carlo algorithms with a) measurements in a water phantom and b) the gamma index between both algorithms in the proton range axis

Shown in Figure 3.26a are measurements taken in a water phantom along the range direction compared to the dose calculated by a pencil beam algorithm and by Monte Carlo algorithm. Although all three plots relatively agree, there is some discrepancy between them in the distal fall off region. The measurements tend to have better agreement with the Monte Carlo calculation. Figure 3.26b shows the dose profile calculated between the planning system and Monte Carlo in the range direction, along with a gamma analysis comparing the two distributions. The same disagreement is shown in the distal fall off, but there is also disagreement in the tail. This difference is confirmed by the increase in the gamma values at these locations. The observed correlations in Yamashita et. al differ slightly from the observations in the profiles from this study, as this is a different planning system (XiO). However, the conclusion is there are inaccuracies in the dose calculation that may be the main reason for the mismatch between the TPS measured profiles and the film profiles.

For the phantom films, the response was up to 10% lower than the predicted TPS calculation in the SOBP, and up to 15% lower in the distal fall off region. To determine why such magnitude of variation was observed, especially with the use of a junction and multi-field optimization method, an additional single field spot scanning irradiation was performed. Plan parameters and energy were comparable to the scanning plan using the 2 field geometry. This plan was delivered and the dosimeters were evaluated in the same manner as for the 2-field spot scanning treatment plan.

The TLD results from the single field scanning delivery are shown in Table 3.14. The measured TLD dose was consistently lower than the calculated dose for both the left inferior and right superior TLD. Similar to the previous spot scanning results, the left inferior measured TLD dose was lower than its counterpart. Both TLD were within passing criteria.

T LD Location	Right Superior	Left Inferior
Measured Dose	595.6	583.9
Calculated-TPS Dose	610.1	617.9
Ratio (Measured/Calculated)	0.976	0.950

Table 3.14: Single Field Spot Scanning Irradiation TLD Results

The 2D gamma analysis was again calculated for both film planes using criteria of 5%/5mm and 5%/3mm. The gamma color maps from the coronal plane (Figure 3.27) display failure in the CTV that was observed in similar locations in the previous spot scanning gamma analysis. The coronal plane passes the 5%/5mm criteria, while failing the 5%/3mm criteria. The sagittal plane does not pass either criterion. Using the less strict criteria, there is some disagreement observed in the CTV with prominent failure at the end of the distal range. The disagreements are magnified as the criterion is tightened.

Film Plane	Coronal	Sagittal
5%/5mm Passing Percentage	88%	54%
5%/3mm Passing Percentage	84%	33%

Table 3.15: 2D Gamma Analysis Results for Single Field Spot Scanning Trial

a) 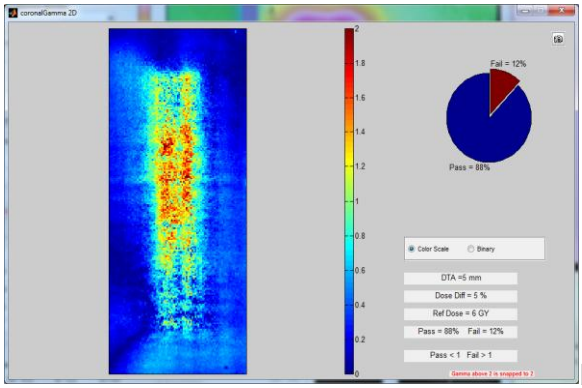

b) 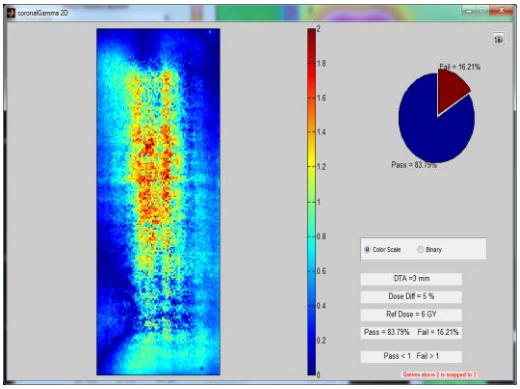

Figure 3.27: 2D Gamma Color Maps from Single Field Spot Scanning Delivery in the coronal plane using a) 5%/5mm and b)5%/3mm criteria

a) 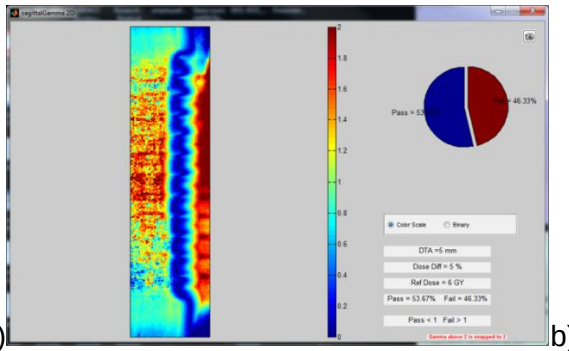 b) 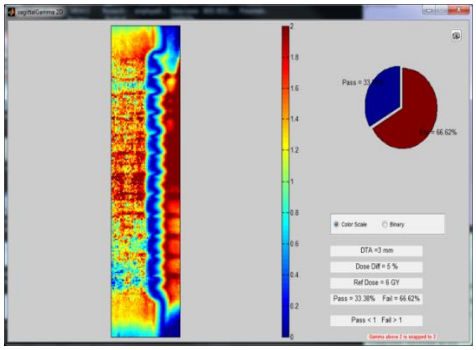

Figure 3.28: 2D Gamma Color Maps from Single Field Spot Scanning Delivery in the sagittal plane using a) 5%/5mm and b) 5%/3mm

Examining the treatment plan closely, a view of the left inferior TLD in the axial plane is shown in Figure 3.29. This view shows a hot spot in the middle of the CTV. A hot spot in this location would not be as sharp and prominent on a passive scattering plan, as the dose should scatter out of the plane. This suggests that the passive scattering deliveries are less sensitive to deficiencies in the algorithm compared to the spot scanning deliveries, due to the small differences in the dose calculation models between the two techniques.

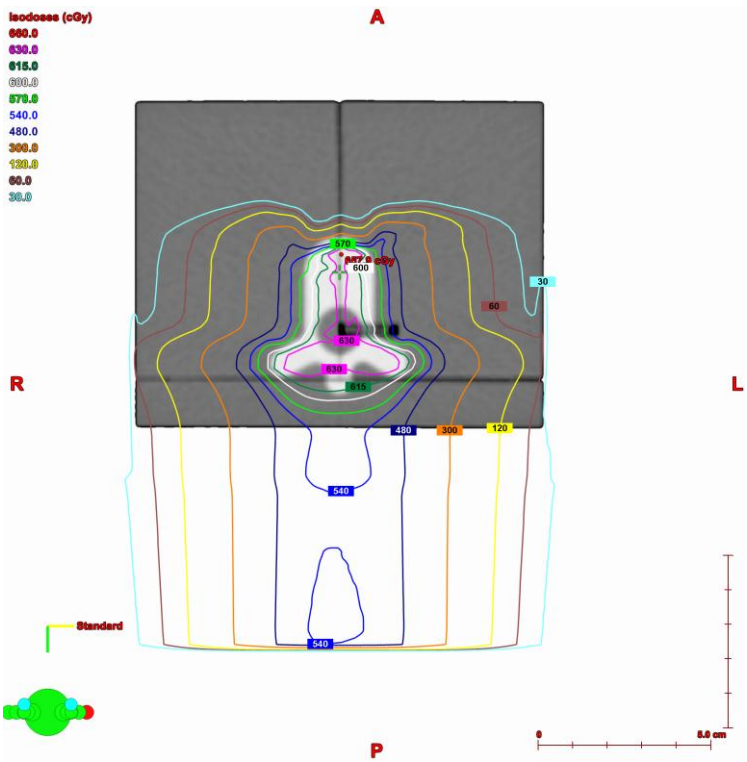

Figure 3.29 Axial View of the Left Inferior TLD in the Single Field Spot Scanning Treatment Plan

The right-left profile acquired in the superior and inferior field is shown in Figures 3.30 and 3.31, respectively. More disagreement between the TPS and film is observed on the right, consistent with the results seen from previous spot scanning irradiations. However, there is now an under response in the dose spanning the target (5-6%). A reason for this effect is due to the film normalization to TLD that were consistently lower than the dose calculated by the treatment plan.

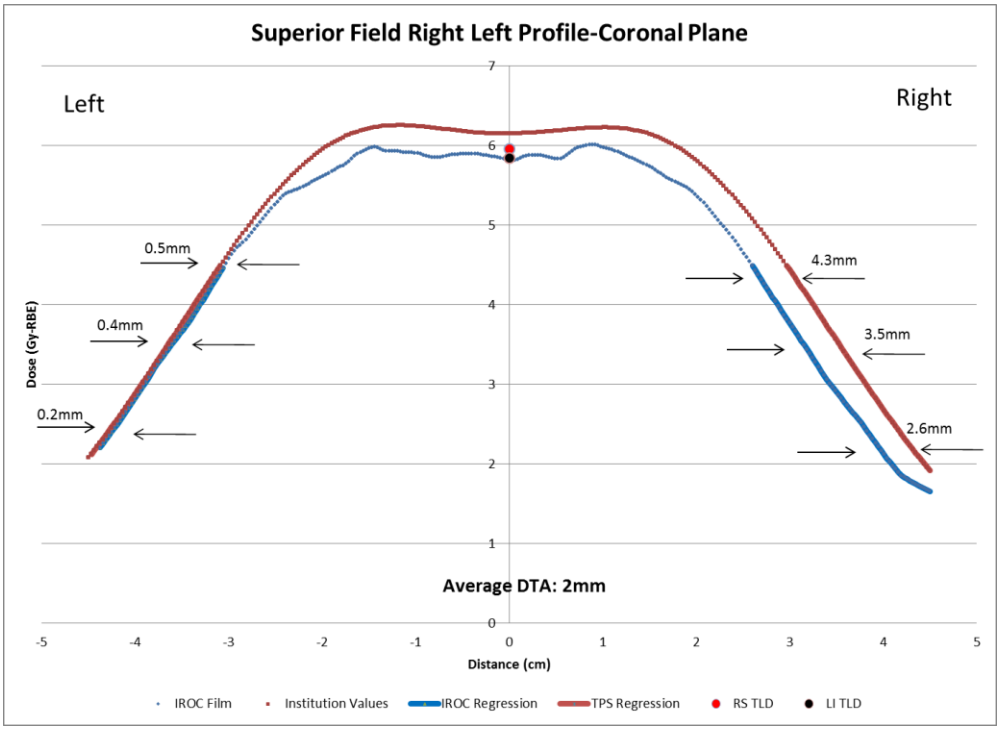

Figure 3.30: Right-left profile in the superior field for single field spot scanning trial, measured in the coronal plane

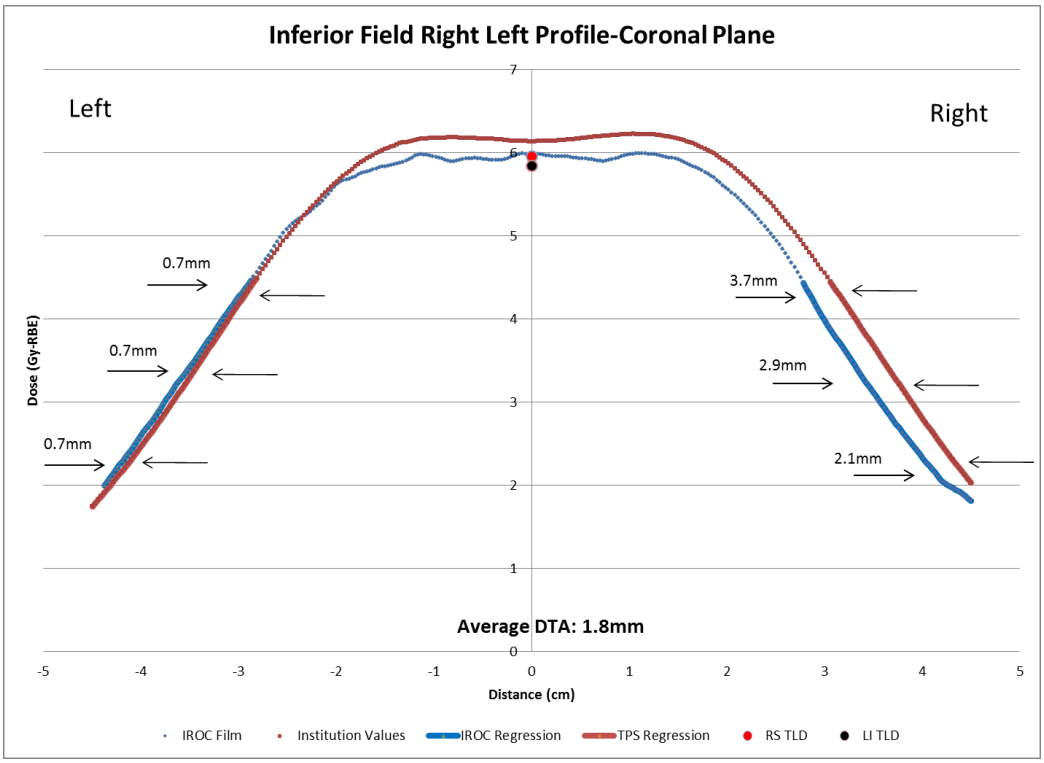

Figure 3.31: Right-left profile in the inferior field for single field spot scanning trial, measured in the coronal plane

Displayed in Figures 3.32 and 3.33 are the A-P profiles acquired through the bone and through the cartilage. An under-response of the film in still observed in the SOBP and distal fall off regions (7-8% in both profiles), along with an over-response past the end of the proton beam range (up to 1 Gy on bone profile, >1 Gy for cartilage profile). The profiles for bone are cartilage appear to display similar responses compared to the large differences observed between these two profiles in the previous scanning beam analysis.

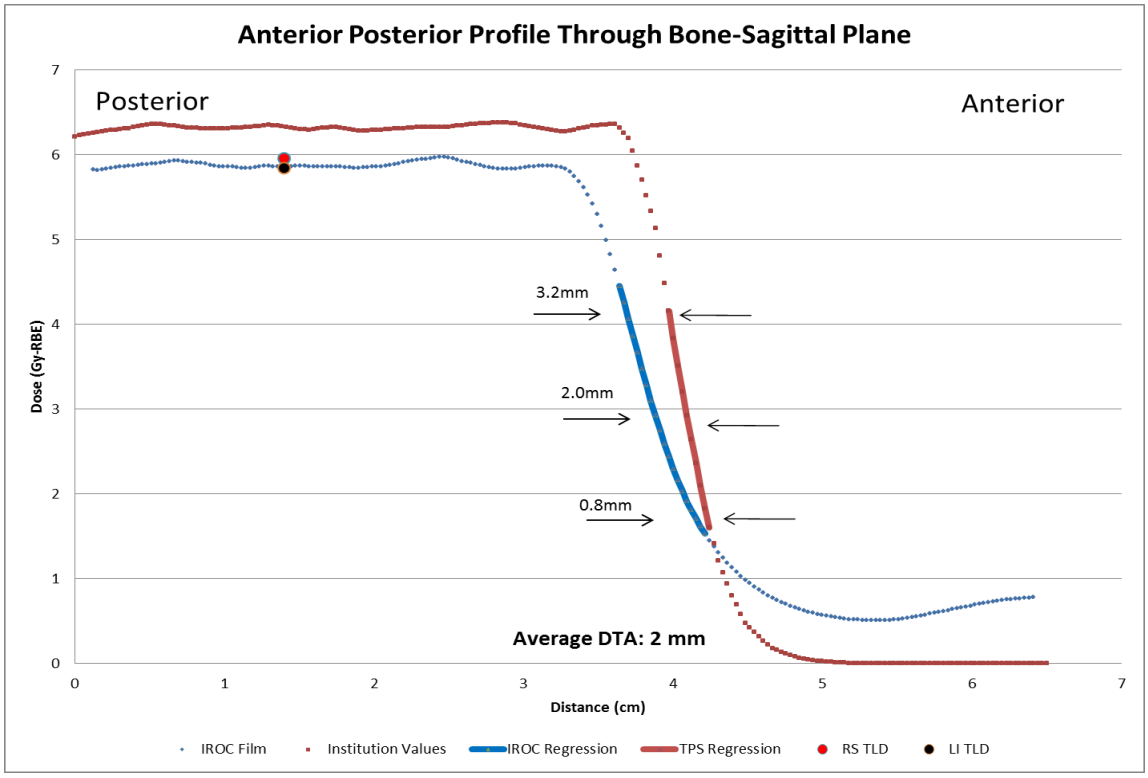

Figure 3.32: A-P Profile in the superior field through bone for Single field spot scanning trial, measured in the sagittal plane

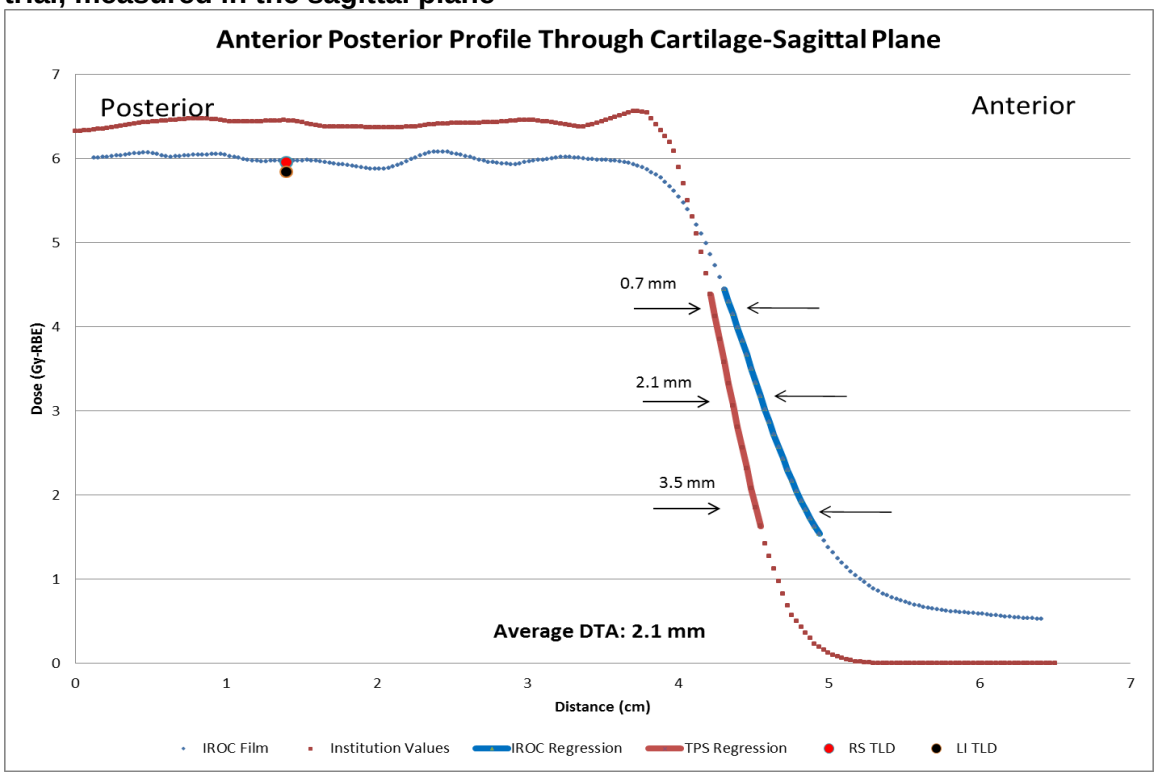

Figure 3.33: A-P Profile in the Inferior field through cartilage for Single Field Spot Scanning Trial, measured in the sagittal plane

Figures 3.34 and 3.35 show the superior-inferior profiles in the coronal and sagittal planes. The dose variation observed in the film is comparable to the dose from the treatment planning system, suggesting that the overlapping junction region may have contributed to the significant dose variation. Similar to the right-left profiles, there is an under dosing of the target (7% in the coronal plane, 10% in the sagittal plane).

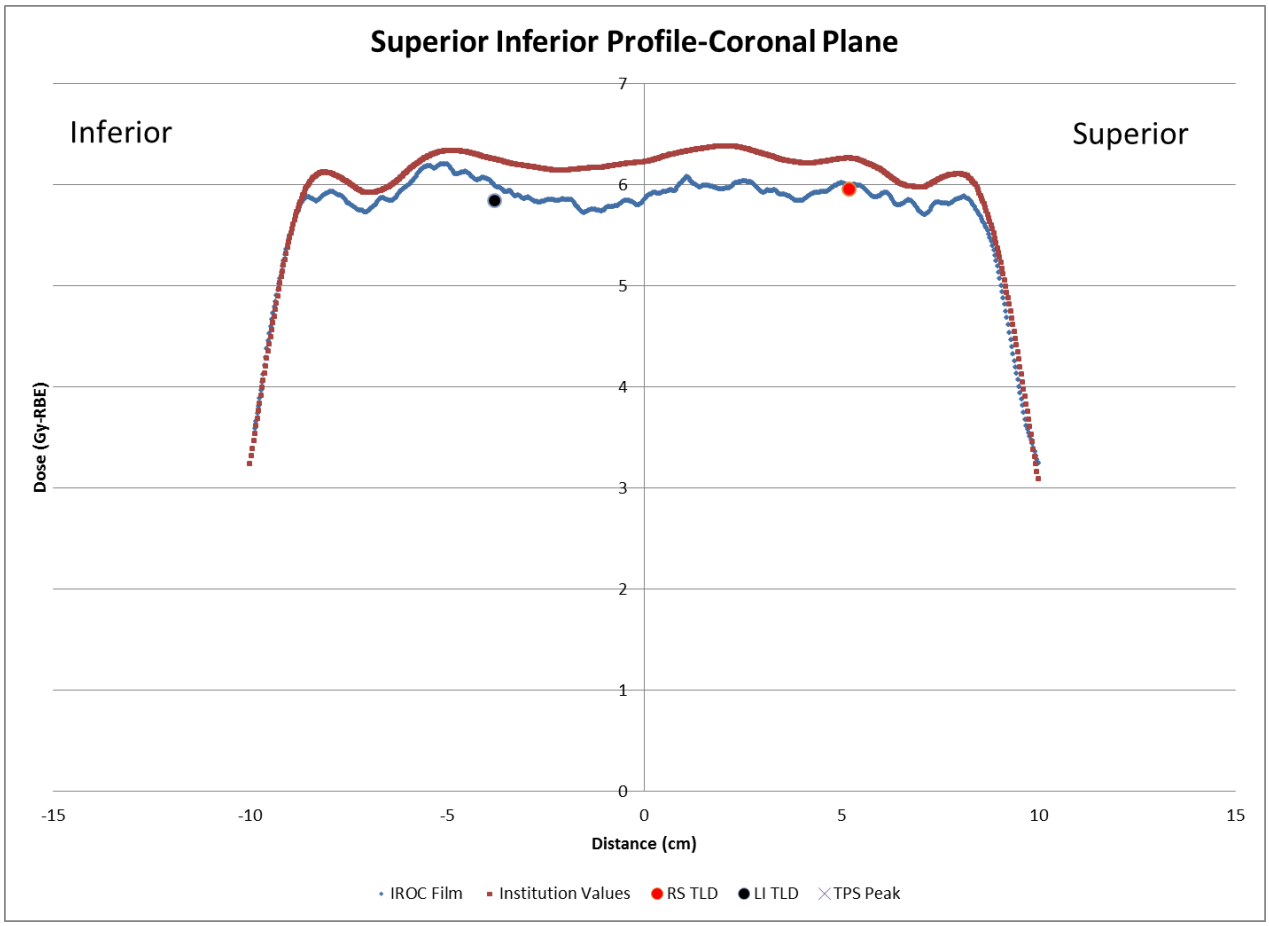

Figure 3.34: S-I Profile for Single Field Spot Scanning trial, measured in the coronal plane

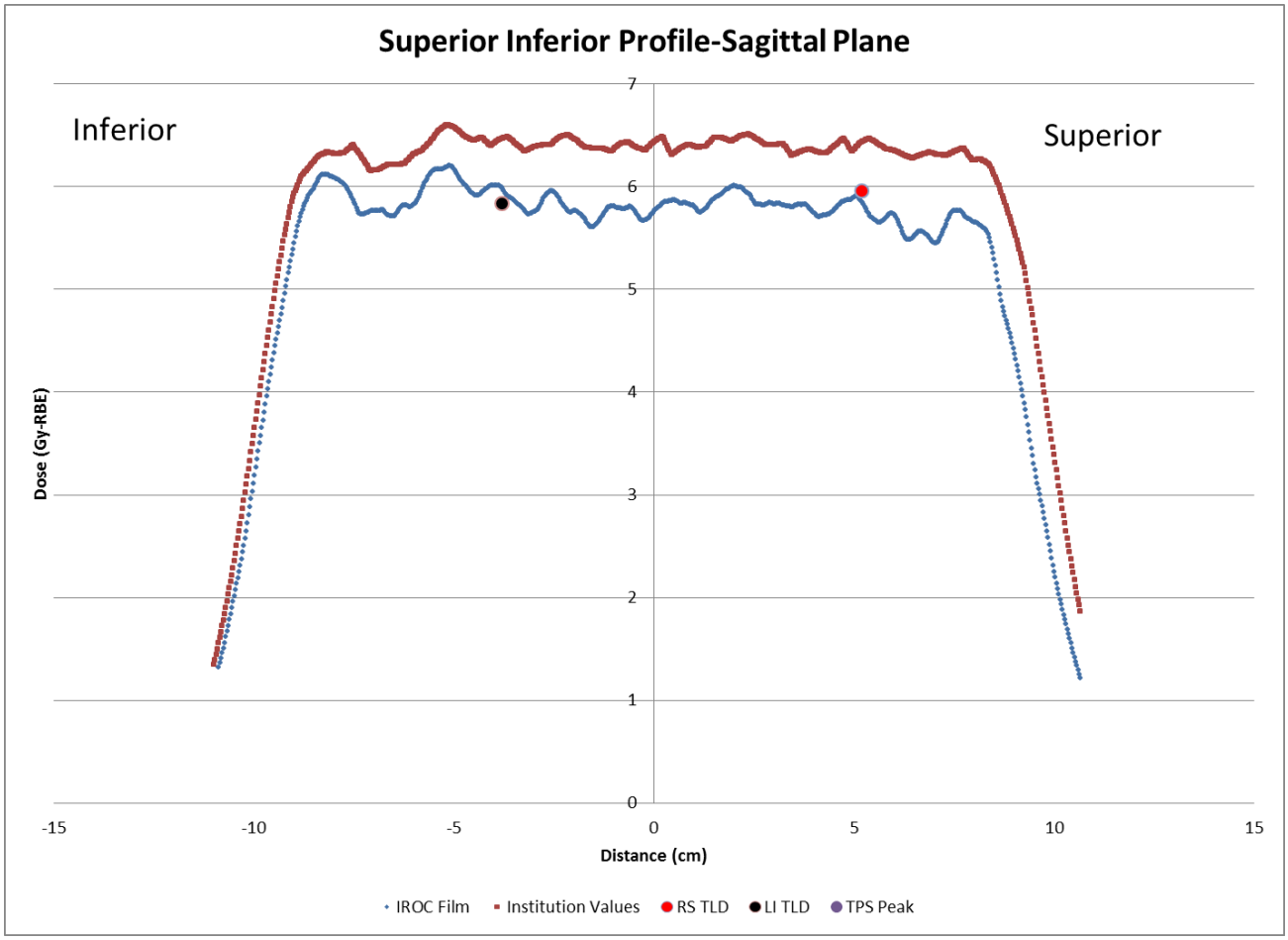

Figure 3.35: S-I Profile for Single Field Spot Scanning trial, measured in the sagittal plane

Although some differences between the dose profiles of the single field and multiple field scanning deliveries are observed, overall, the results are quite similar. The results from the single field spot scanning irradiation further suggests that problems with the scanning dose calculation algorithms and corrections to quenching in the film dosimeter should be investigated.

4 Conclusions

4.1 Meeting Specific Aims

The purpose of this study was to design an anthropomorphic pediatric spine phantom for use in the evaluation of proton therapy facilities for clinical trial participation by IROC Houston. The hypothesis states that this phantom can be designed and assures that the measured doses would agree with the calculated doses with a 5%/3mm criteria and a TLD point dose agreement within 5%.

The first specific aim was to design a phantom that accurately simulated a patient in the thoracic region of the spinal column. Potential tissue equivalent materials were evaluated by determining the HU and RSP and then comparing each to the HU-RSP calibration curve. The materials used in the phantom-Techron HPV Bearing Grade, solid water and blue water- are within 2% of the HU and RSP in the Eclipse treatment planning system used by the PTC-H. The successful determination of tissue equivalency renders this specific aim complete.

The second specific aim required imaging of the phantom and creating clinically relevant treatment plans for both irradiation techniques. The phantom was CT-scanned at the PTC-H, and these images were used to create both a passive scattering treatment plan and a spot scanning treatment plan. With the assistance of a proton dosimetrist, these plans were adjusted to a clinically acceptable level that met dose constraints outlined by a radiation oncologist. The phantom was then irradiated a total of 6 times at our institution, completing the second aim.

The third specific aim was to measure the dose distributions from the treatment deliveries using radiochromic film and TLD. Two pieces of film, one in the coronal plane and one in the sagittal plane, were used per delivery to measure the planar distributions. The batch of film was calibrated to ensure that the dose conversion was accurate. Two TL dosimeters, in the right superior and left inferior locations of the spinal canal, were used to measure the absolute dose. Relevant information from the batch previously characterized was used to

determine the measured point dose. The calibration of the film and TLD along with the proper placement of these dosimeters in the phantom completes the third aim.

The fourth specific aim required analysis of the dose distribution data to determine the accuracy of all work done in specific aims 1, 2, and 3. During the dose profile comparison of the data between the film, TLD, and TPS, the following attributes were evaluated: absolute dose agreement, distal range, field width, junction match and right/left profile alignment. The average pixel pass rate for gamma analysis of the passive scatter irradiations was 94.7% for the 5%/5mm criteria and 88.8% for the 5%/3mm criteria. The average pixel pass rate for gamma analysis of the spot scanning irradiations was 86.8% for the 5%/5mm criteria and 79.4% for the 5%/3mm criteria. The determination of the dose differences and agreement completes the last specific aim of the project.

There were some limitations seen in this study. For the passive scattering irradiation, a sum plan of 2 junction plans was delivered to the phantom. Because this approach includes feathering at the junction, the dose distribution from the hot and cold spots was smoothed out. While this technique reflected current clinical practice, it made evaluation of a single dose match point more difficult. The feathered junction approach was not used for the spot scanning plans. Due to differences at the junction region between the two delivery techniques, the spot scanning junction profiles were unable to be evaluated.

4.2 Clinical Significance

Developing a phantom that audits the accuracy of simulation, dose calculation from the treatment planning system and the treatment delivery of proton therapy is becoming increasingly more important. With the opening of more proton therapy centers, it is imperative that IROC Houston update their quality assurance tools used to credential institutions for clinical trial participation. Although IROC Houston currently has two commissioned phantoms for proton therapy, the deterioration of the spine phantom called for the development of a new

remote auditing tool. The spine phantom developed for this study proves suitable for use during the baseline proton approval process in the same manner as the phantom that contains human vertebrae. Institutions will still be required by IROC Houston to follow NCI approval guidelines and to complete a full audit before patients can be treated on protocol. Completion of the approval and credentialing process ensures that clinically comparable doses can be safely delivered to a patient and also that accurate, trustworthy clinical trial results can be obtained.

4.3 Future Directions

The outcome of this study shows that the phantom is ready for use as a quality assurance tool for passive scatter proton beams. The spot scanning irradiations should be repeated and better pass rates for all criteria should be achieved. More institutions will need to complete preliminary audits to verify our results and the feasibility of use. The phantom design can be adjusted by adding critical structures to the phantom to not only further increase the difficulty threshold of passing, but also to verify the proton range and the dose to the critical structures.

The procedure for irradiation currently only calls for imaging using CT. However, radiation oncologists at PTC-H may contour patient anatomical structures on MRI-fused images. Materials that comprise most anthropomorphic phantoms are not always distinguishable on MRI images, causing difficulty when determining the imaging procedure for this phantom. Future work includes using magnetic resonance imaging (MRI) for normal structure and lesion delineation and fused with a CT image to complete the dose calculations. Additional future work with this phantom includes a repeat phantom experiment using the spot scanning technique, the assessment of robust optimization of IMPT for use in CSI irradiations, a comparison with the dose verification of the phantom when setup in the prone position, and lastly, the testing of the film and TLD to accurately measure the dose distributions when irradiating with the oblique angles used in CSI treatments.

5 Appendix

5.1 Gamma Analysis

5.1.1 Passive Scattering Irradiations

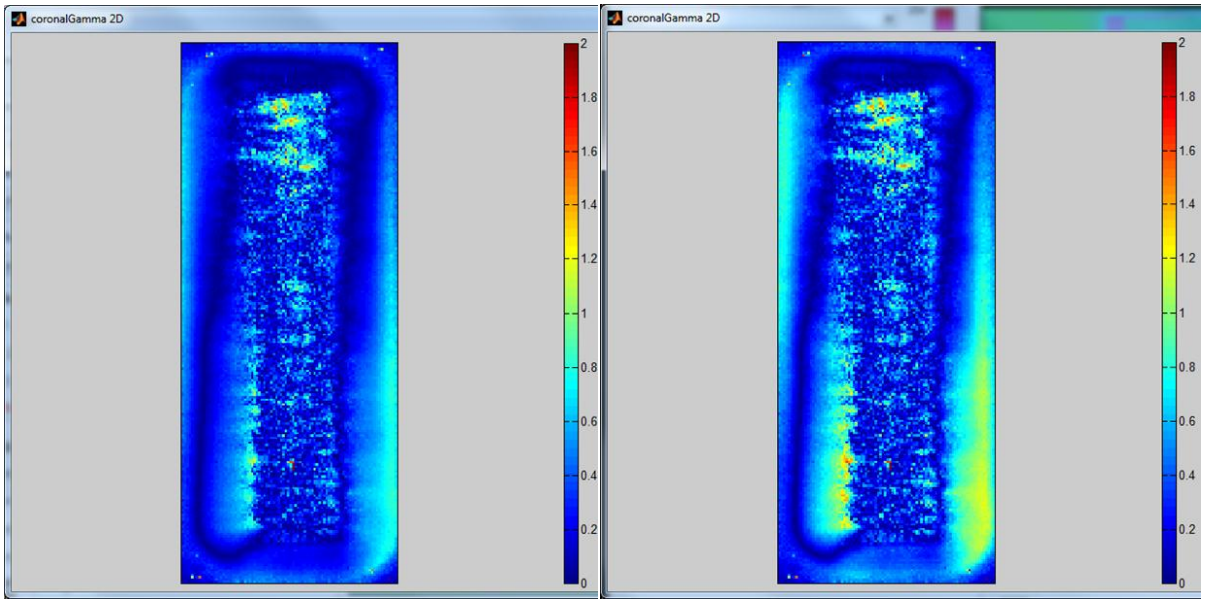

a) 5%/5mm pass rate: 99.57% b) 5%/3mm pass rate: 96.43%

Figure 5.1 Passive Scattering Trial 1 Irradiation 2D Coronal Gamma Analysis

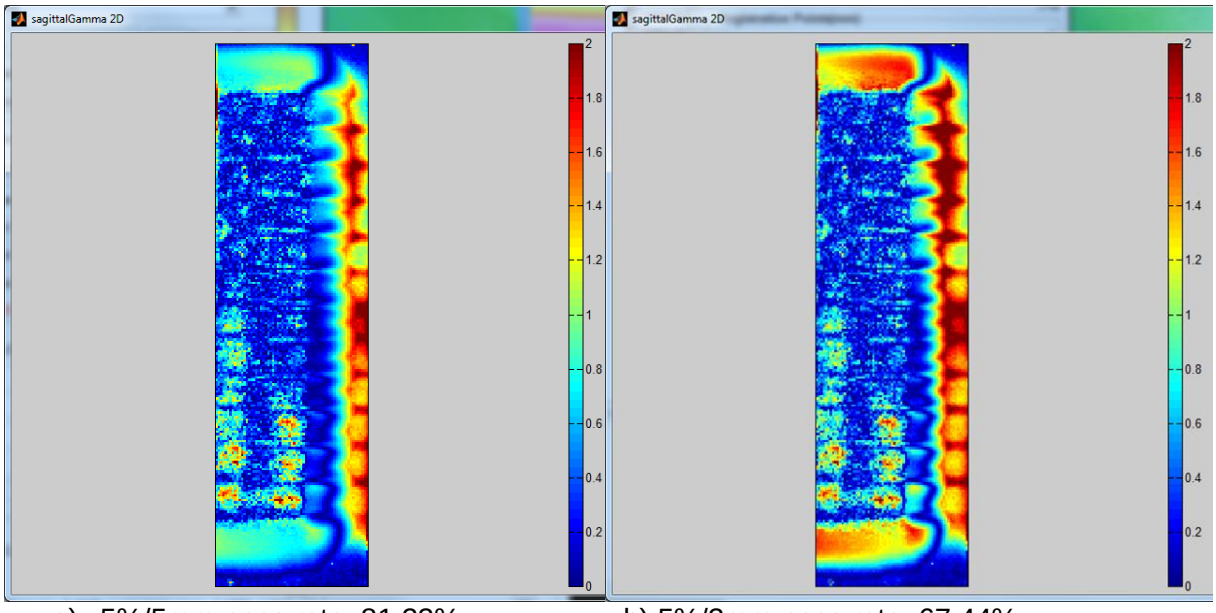

a) 5%/5mm pass rate: 81.23% b) 5%/3mm pass rate: 67.44%

Figure 5.2 Passive Scattering Trial 1 Irradiation 2D Sagittal Gamma Analysis

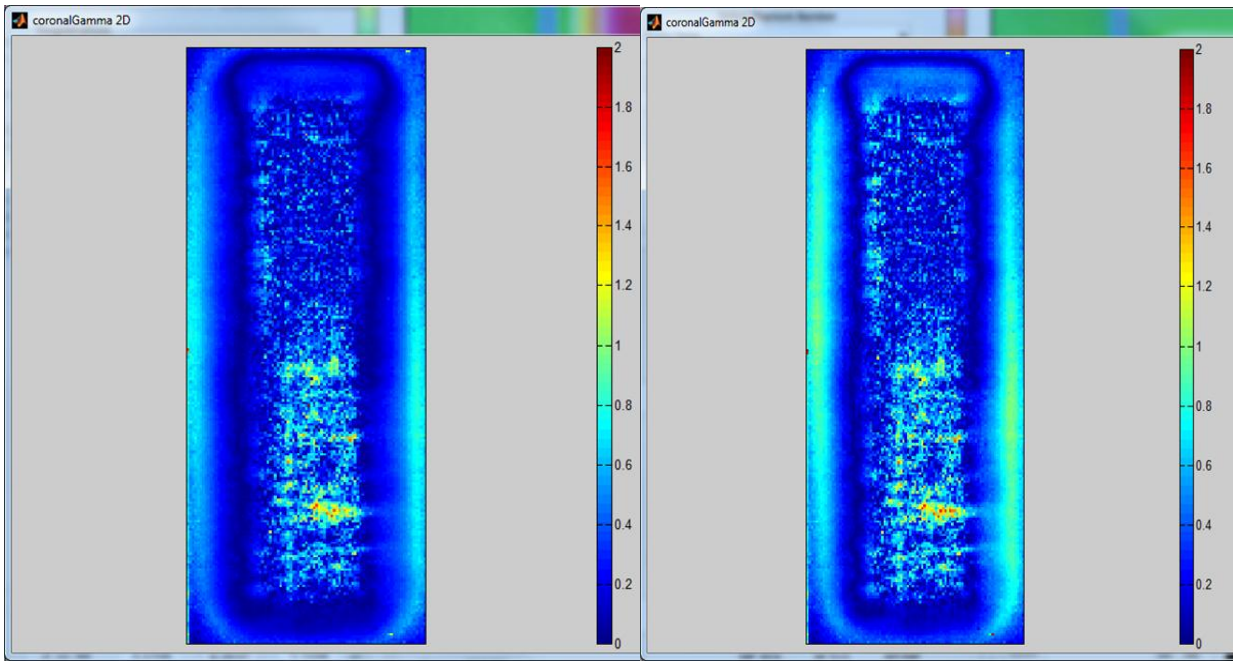

a) 5%/5mm pass rate: 99.21% b) 5%/3mm pass rate: 98.91%

Figure 5.3 Passive Scattering Trial 2 Irradiation 2D Coronal Gamma Analysis

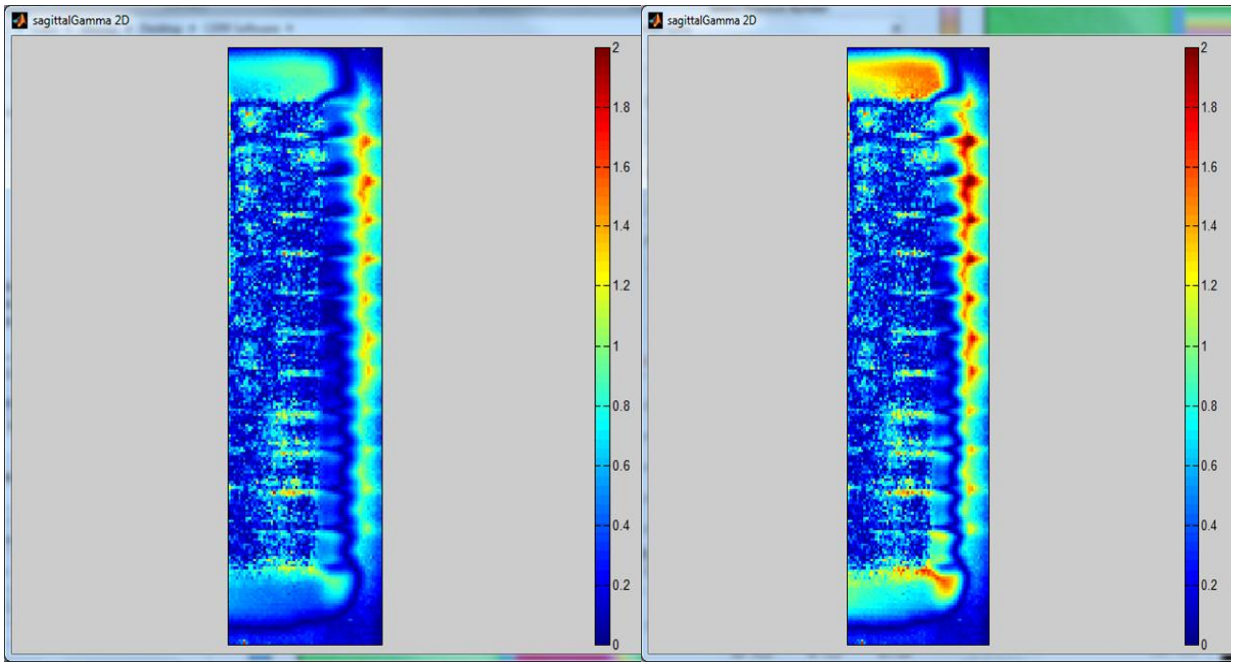

a) 5%/5mm pass rate: 94.57% b) 5%/3mm pass rate: 84.68%

Figure 5.4 Passive Scattering Trial 2 Irradiation 2D Sagittal Gamma Analysis

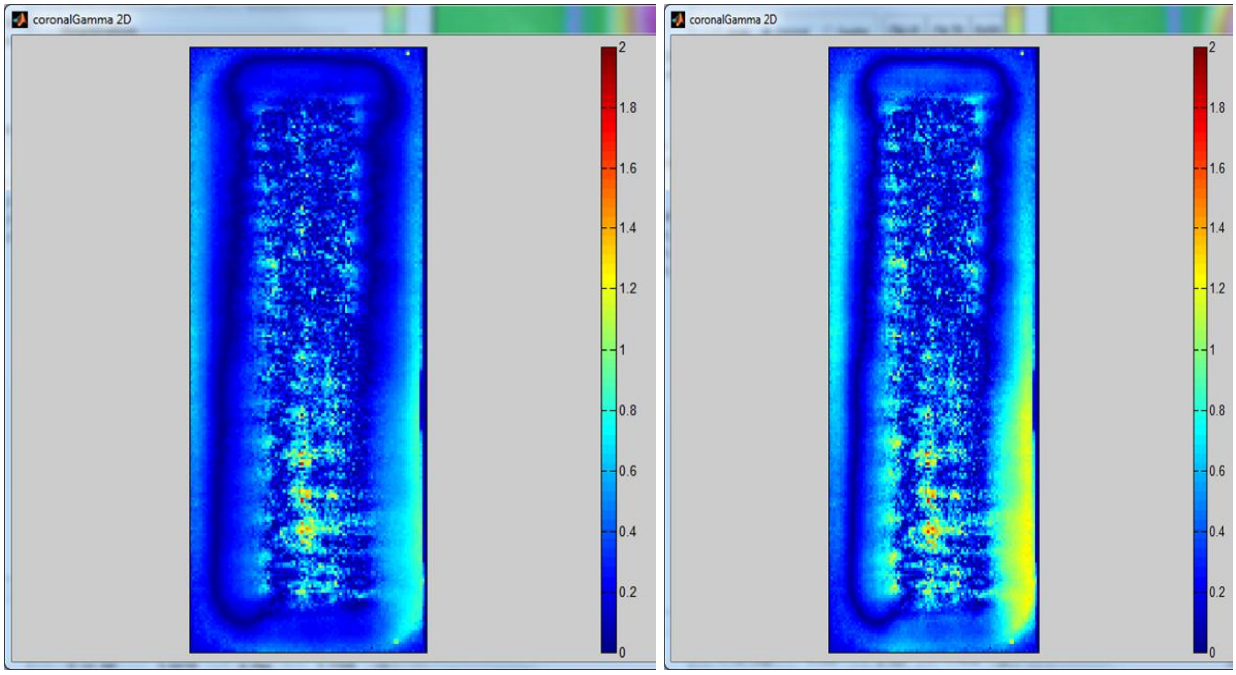

a) 5%/5mm pass rate: 99.36% b) 5%/3mm pass rate: 95.13%

Figure 5.5 Passive Scattering Trial 3 Irradiation 2D Coronal Gamma Analysis

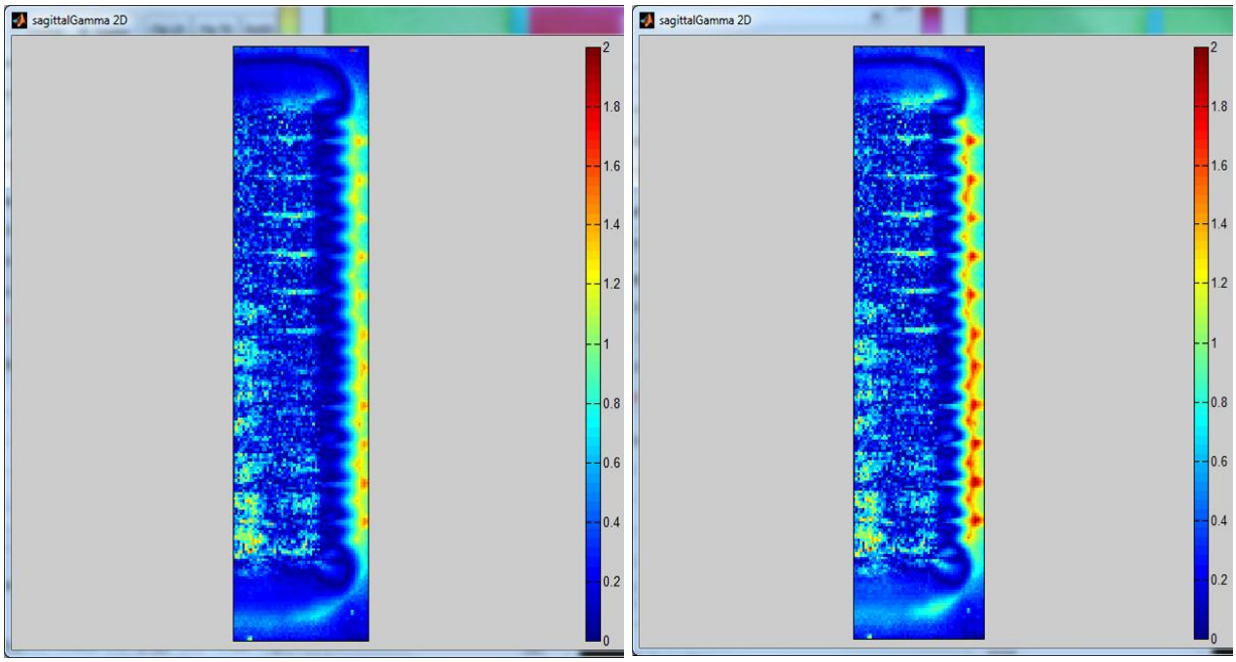

a) 5%/5mm pass rate: 94.13% b) 5%/3mm pass rate: 90.01%

Figure 5.6 Passive Scattering Trial 3 Irradiation 2D Sagittal Gamma Analysis

5.1.2 Spot Scanning Irradiations

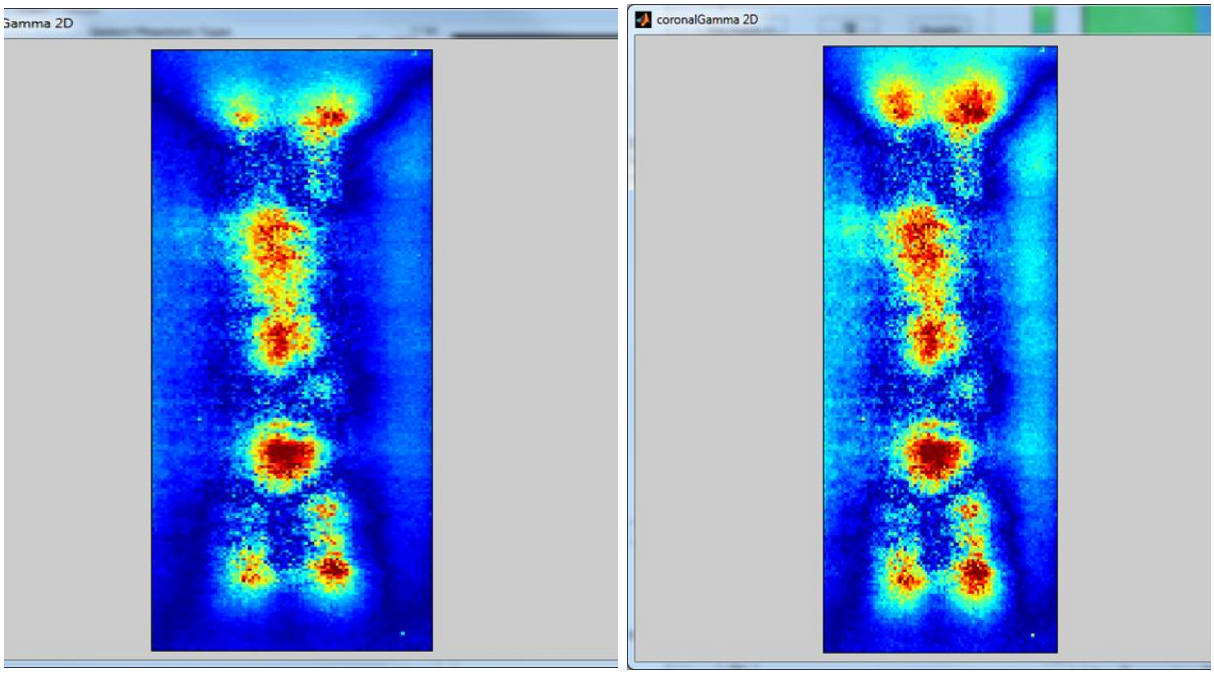

a) 5%/5mm pass rate: 90.87% b) 5%/3mm pass rate: 86.28%

Figure 5.7 Spot Scanning Trial 1 Irradiation 2D Coronal Gamma Analysis

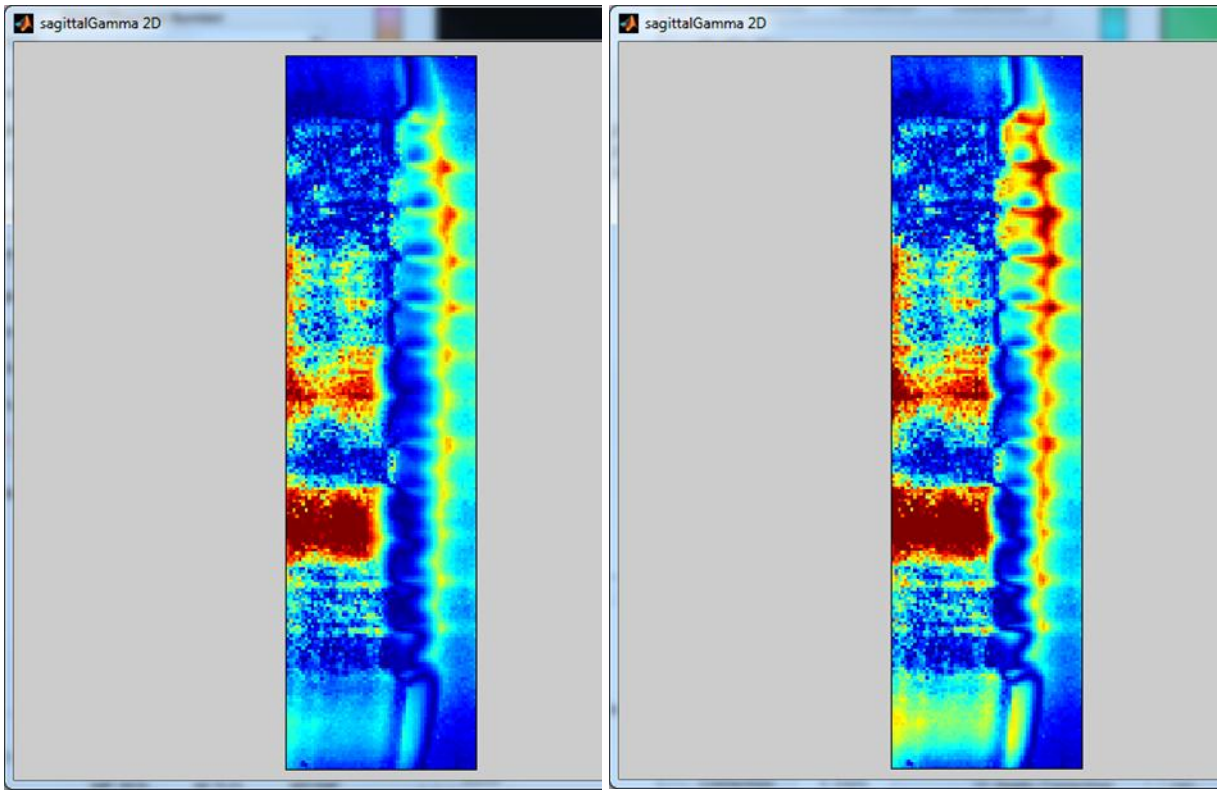

a) 5%/5mm pass rate: 81.94% b) 5%/3mm pass rate: 71.51%

Figure 5.8 Spot Scanning Trial 1 Irradiation 2D Sagittal Gamma Analysis

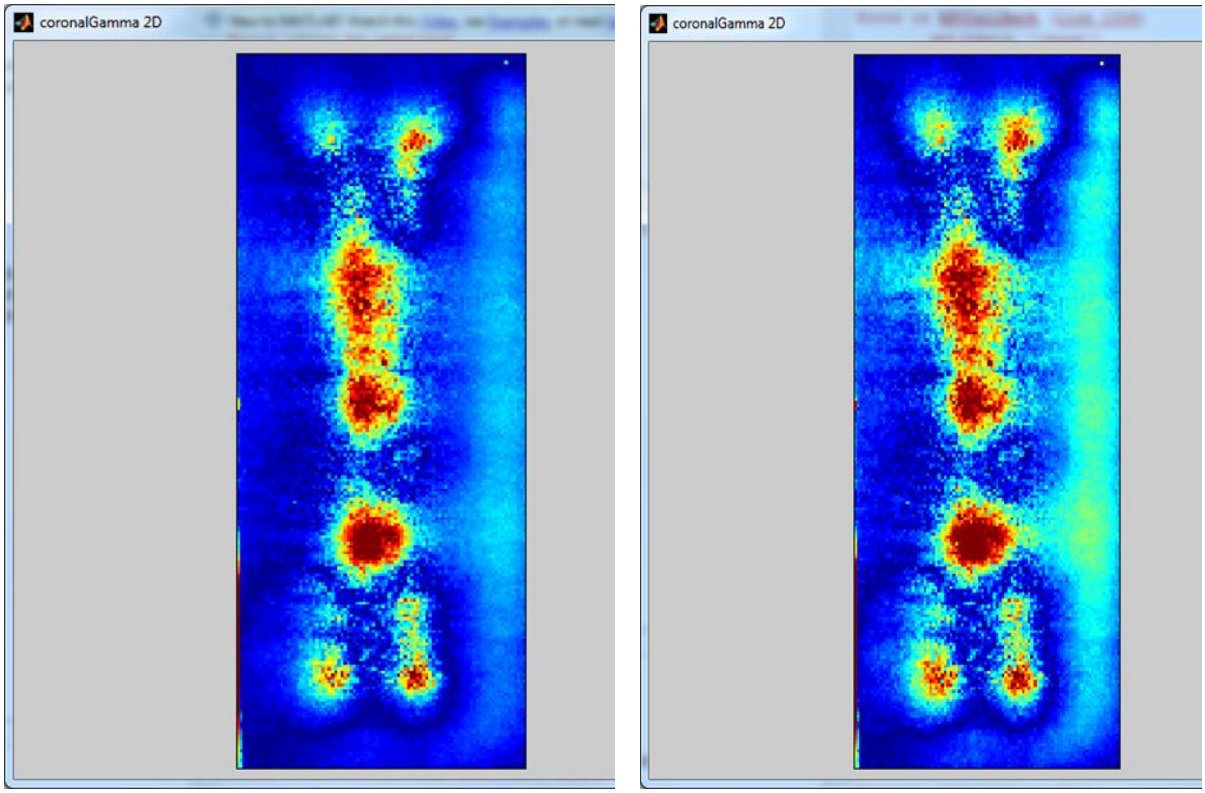

a) 5%/5mm pass rate: 90.57% b) 5%/3mm pass rate: 88.25%

Figure 5.9 Spot Scanning Trial 2 Irradiation 2D Coronal Gamma Analysis

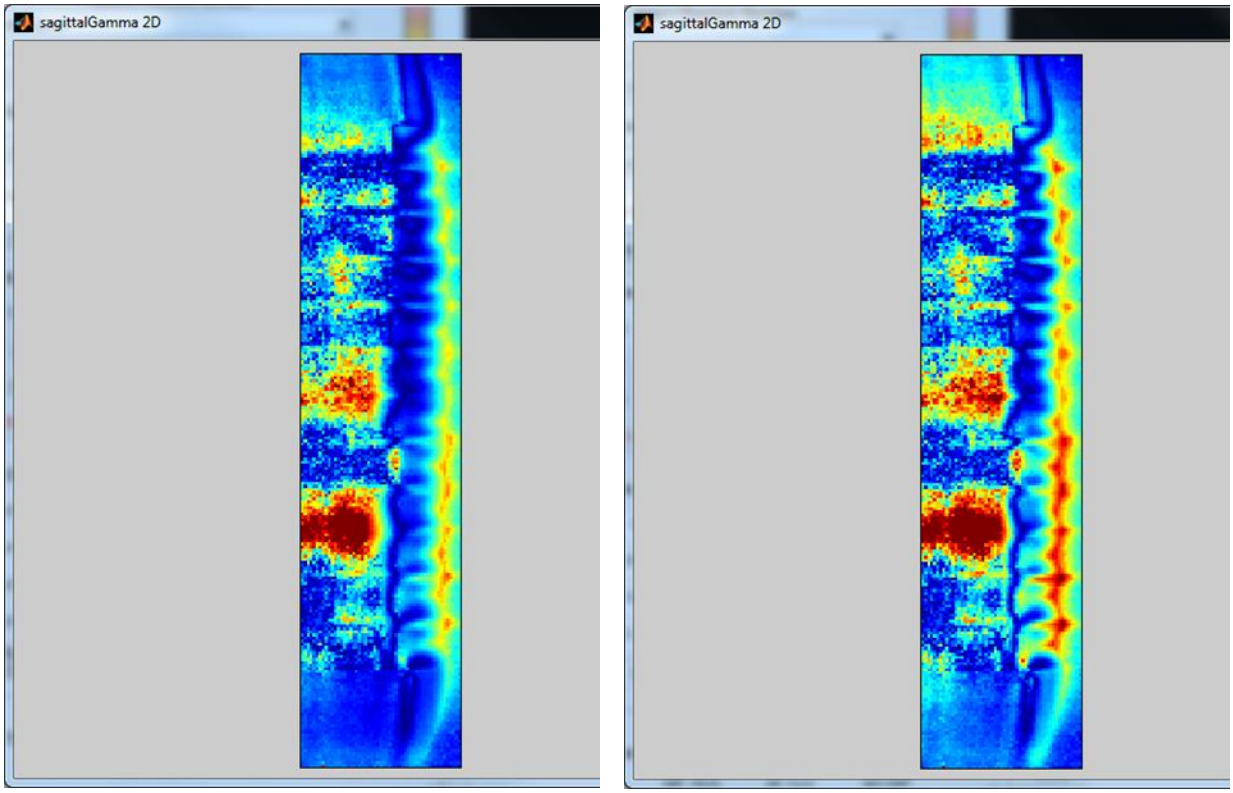

a) 5%/5mm pass rate: 82.42% b) 5%/3mm pass rate: 73.34%

Figure 5.10 Spot Scanning Trial 2 Irradiation 2D Sagittal Gamma Analysis

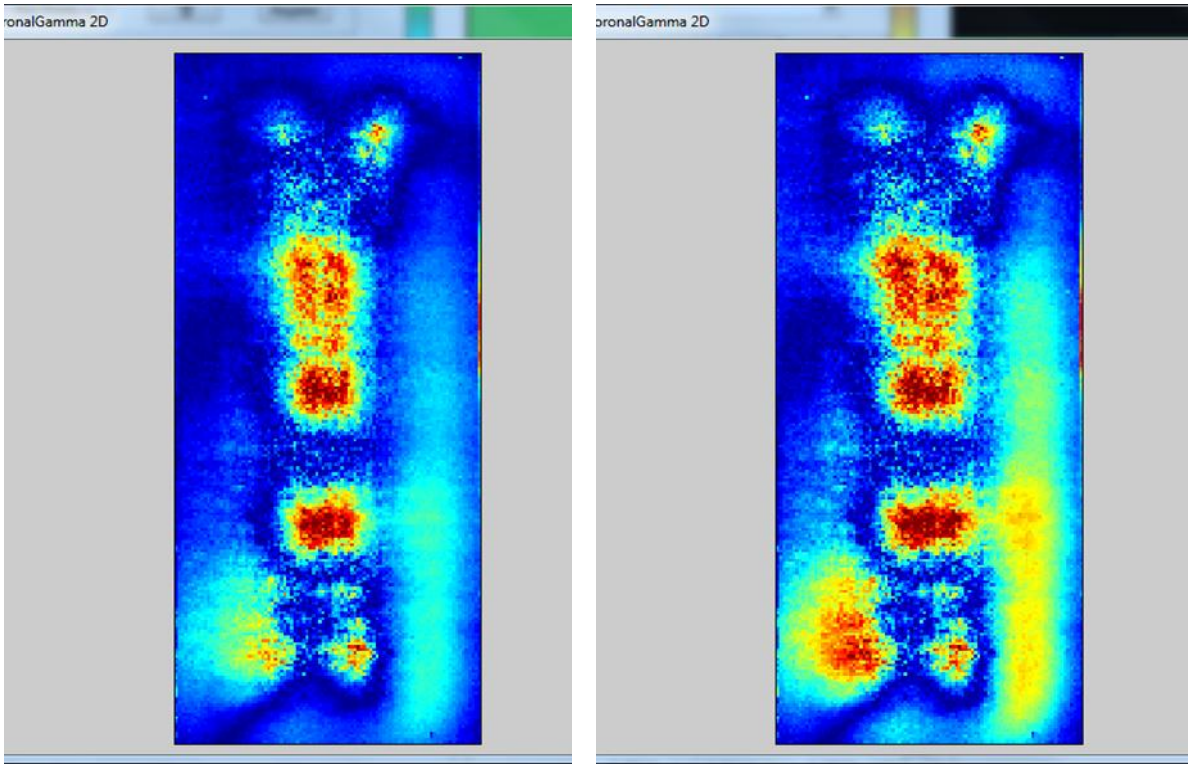

a) 5%/5mm pass rate: 91.00% b) 5%/3mm pass rate: 79.42%

Figure 5.11 Spot Scanning Trial 3 Irradiation 2D Coronal Gamma Analysis

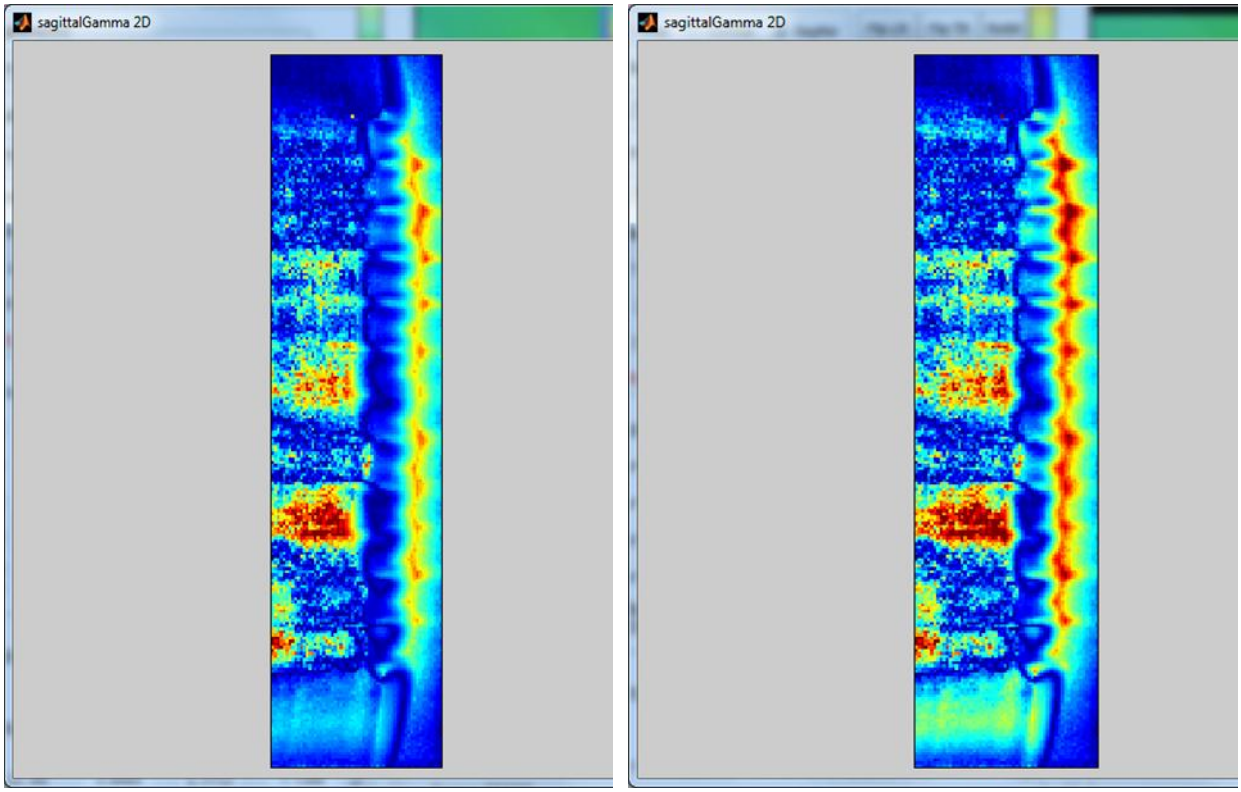

a) 5%/5mm pass rate: 84.12% b) 5%/3mm pass rate: 77.45%

Figure 5.12 Spot Scanning Trial 3 Irradiation 2D Sagittal Gamma Analysis

5.2 Dose Profiles

5.2.1 Passive Scattering Trial Comparisons

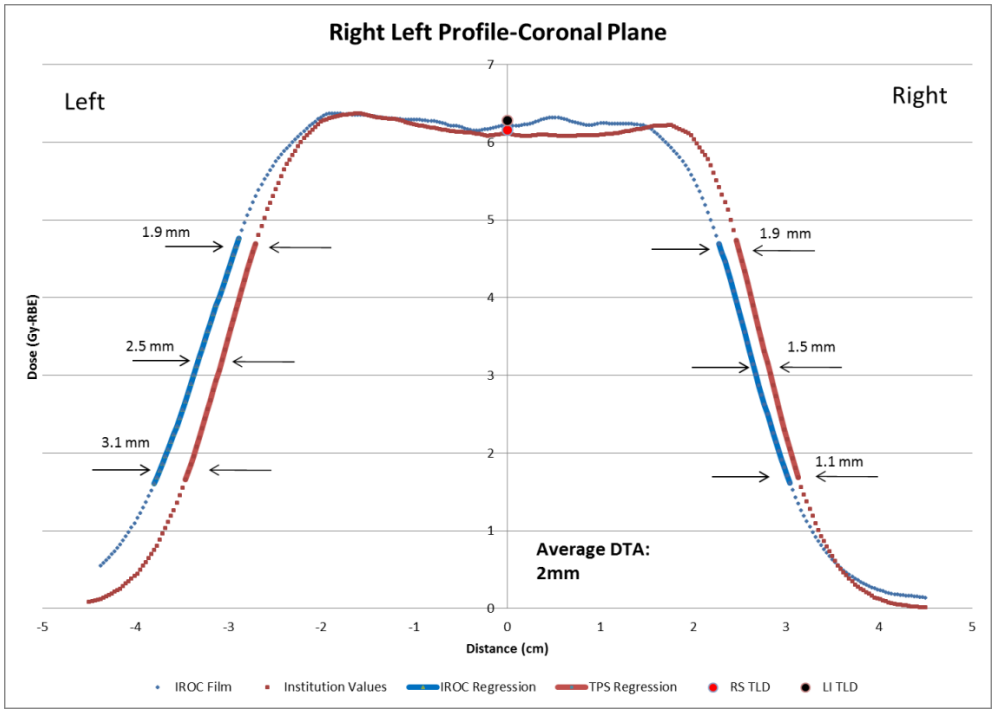

Figure 5.13 R-L Dose Profile for the passive scattering trial 1 upper spine field, measured in the coronal Plane

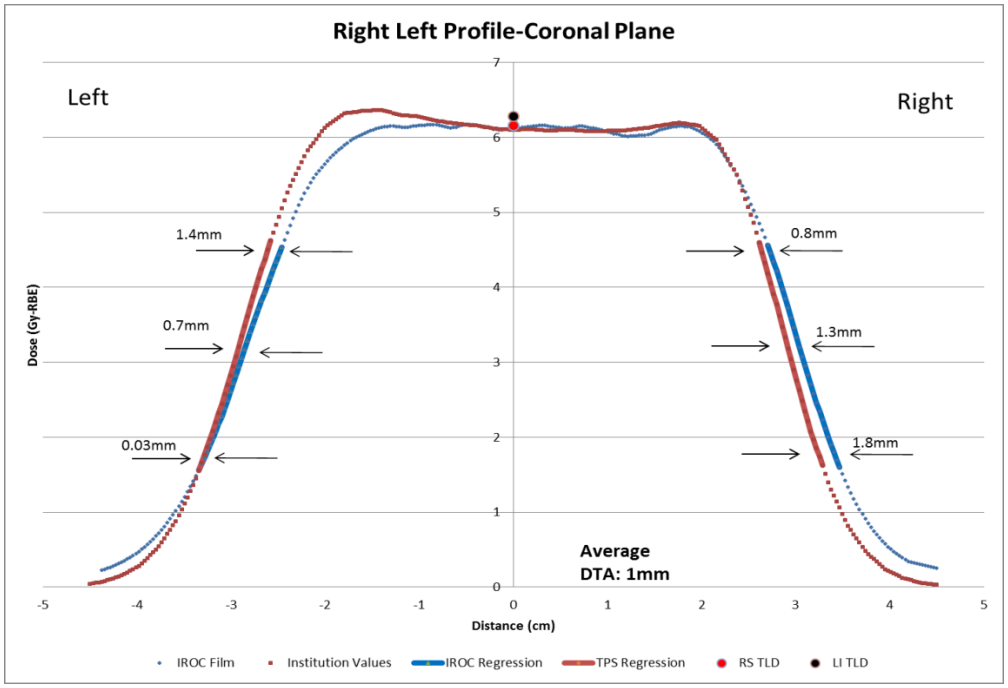

Figure 5.14 R-L Dose Profile for the passive scattering trial 1 lower spine field, measured in the coronal Plane

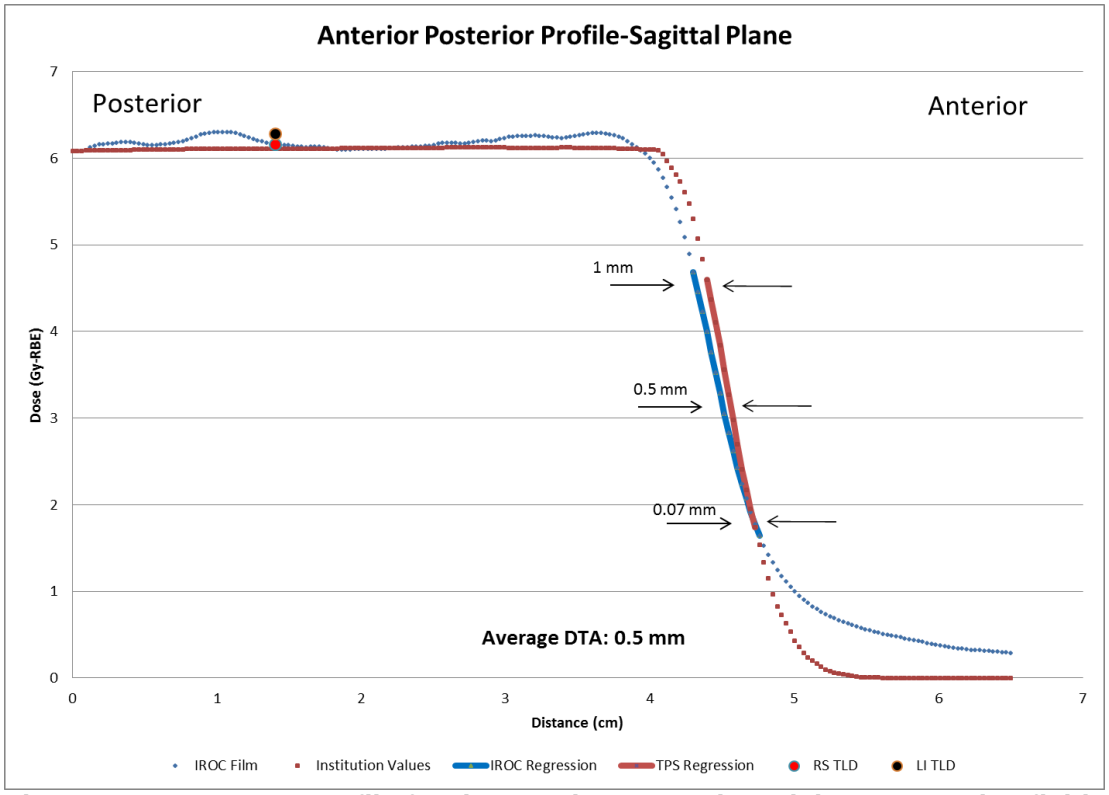

Figure 5.15 A-P Dose Profile for the passive scattering trial 1 upper spine field, measured in the Sagittal Plane

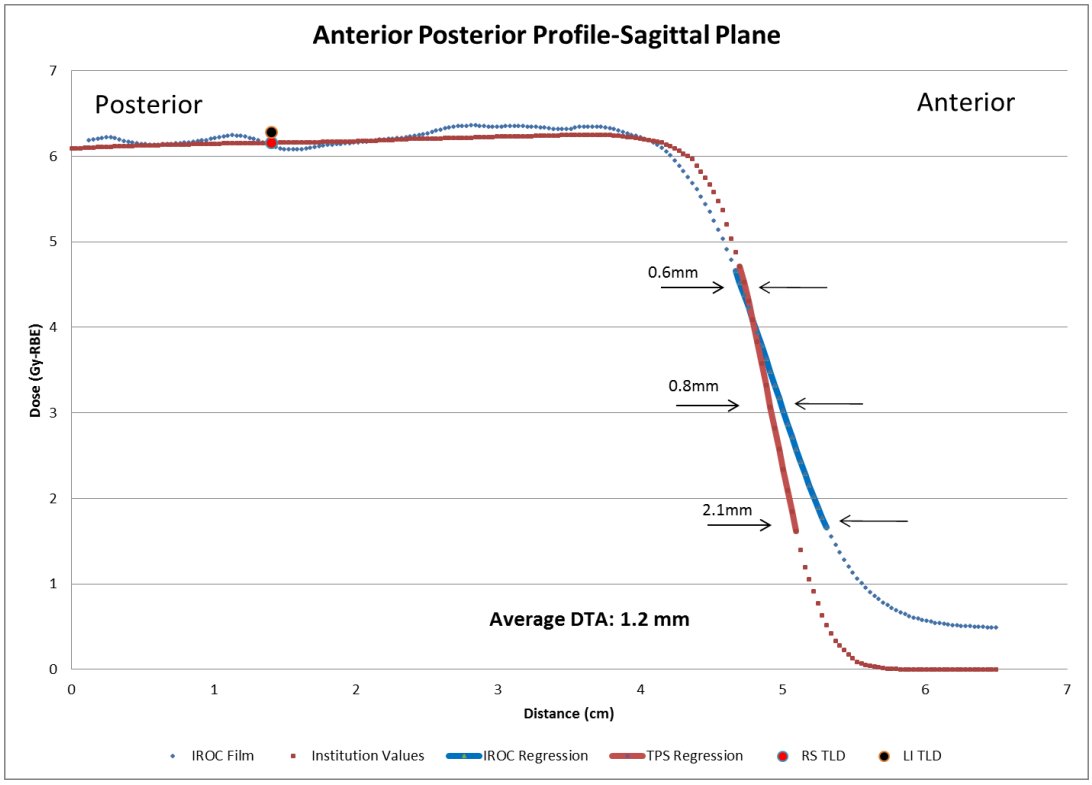

Figure 5.16 A-P Dose Profile for the passive scattering trial 1 lower spine field, measured in the sagittal Plane

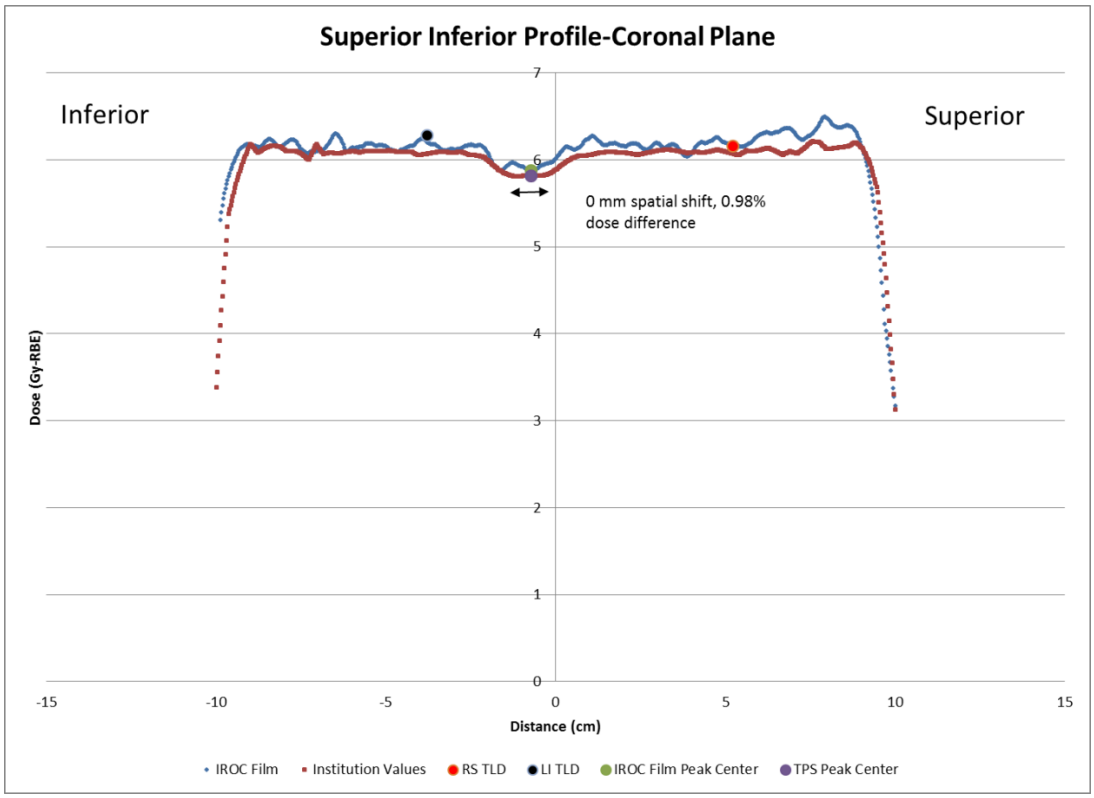

Figure 5.17 S-I Dose Profile for the passive scattering trial 1, measured in the coronal Plane

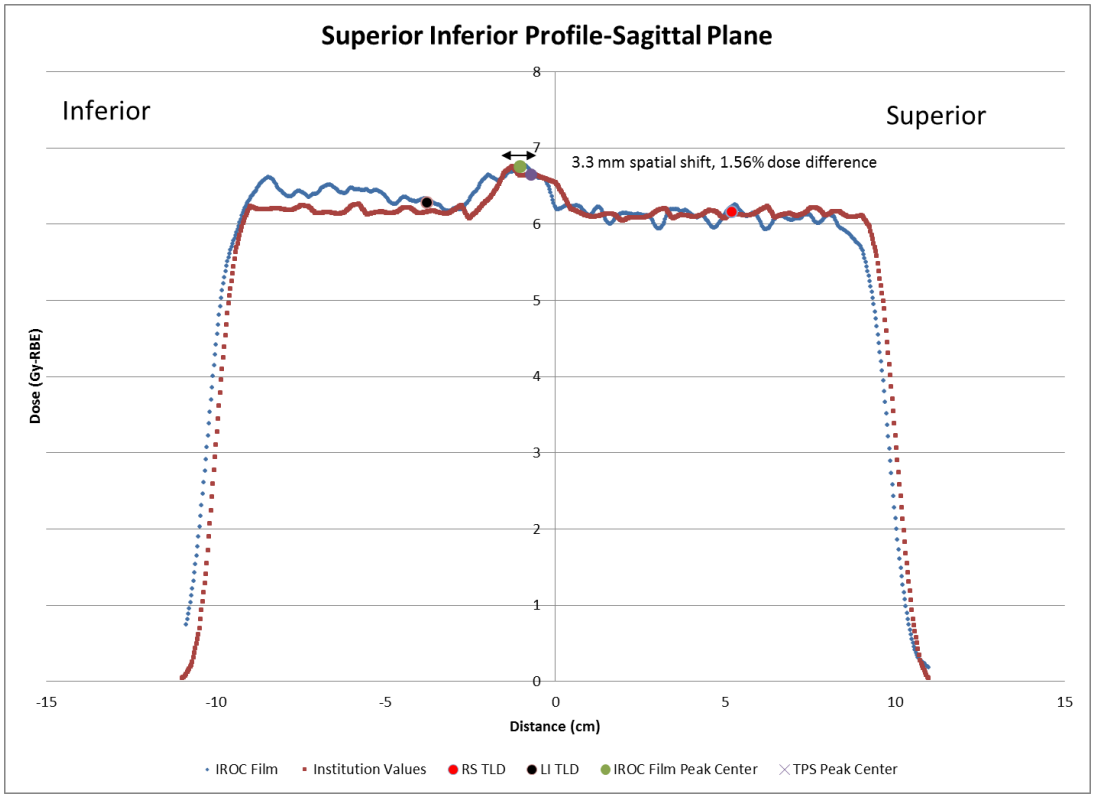

Figure 5.18 S-I Dose Profile for the passive scattering trial 1, measured in the sagittal Plane

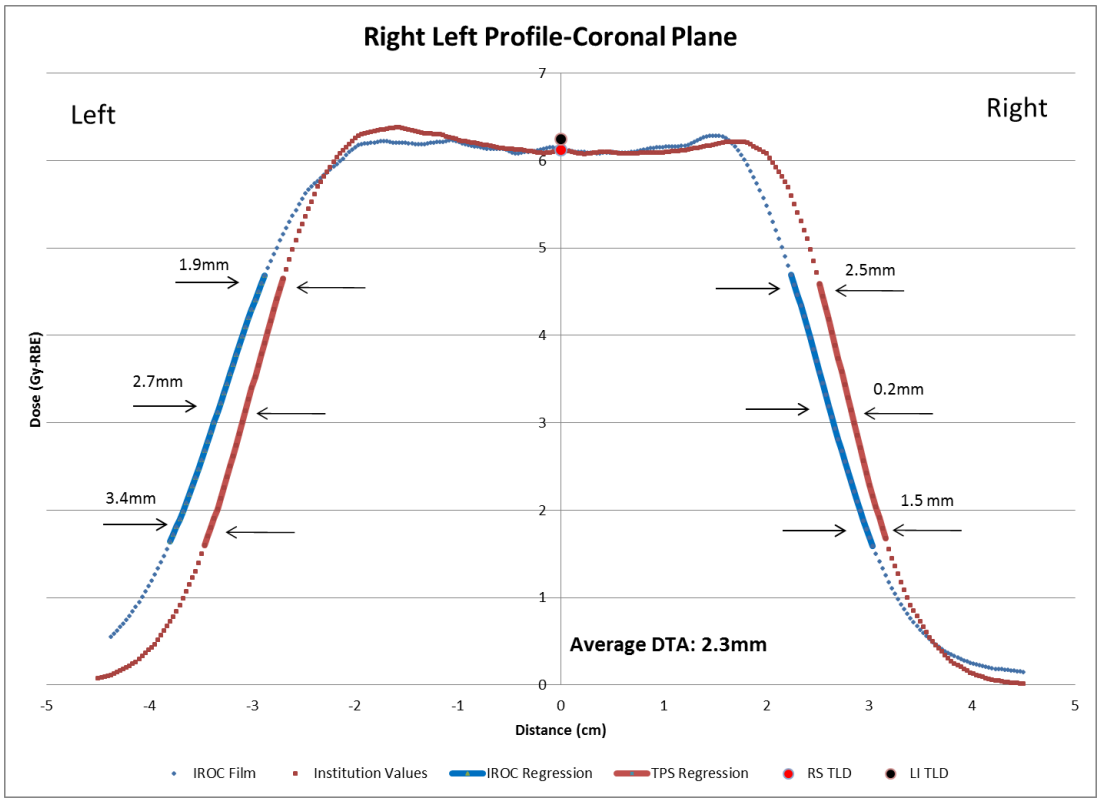

Figure 5.19 R-L Dose Profile for the passive scattering trial 2 upper spine field, measured in the coronal Plane

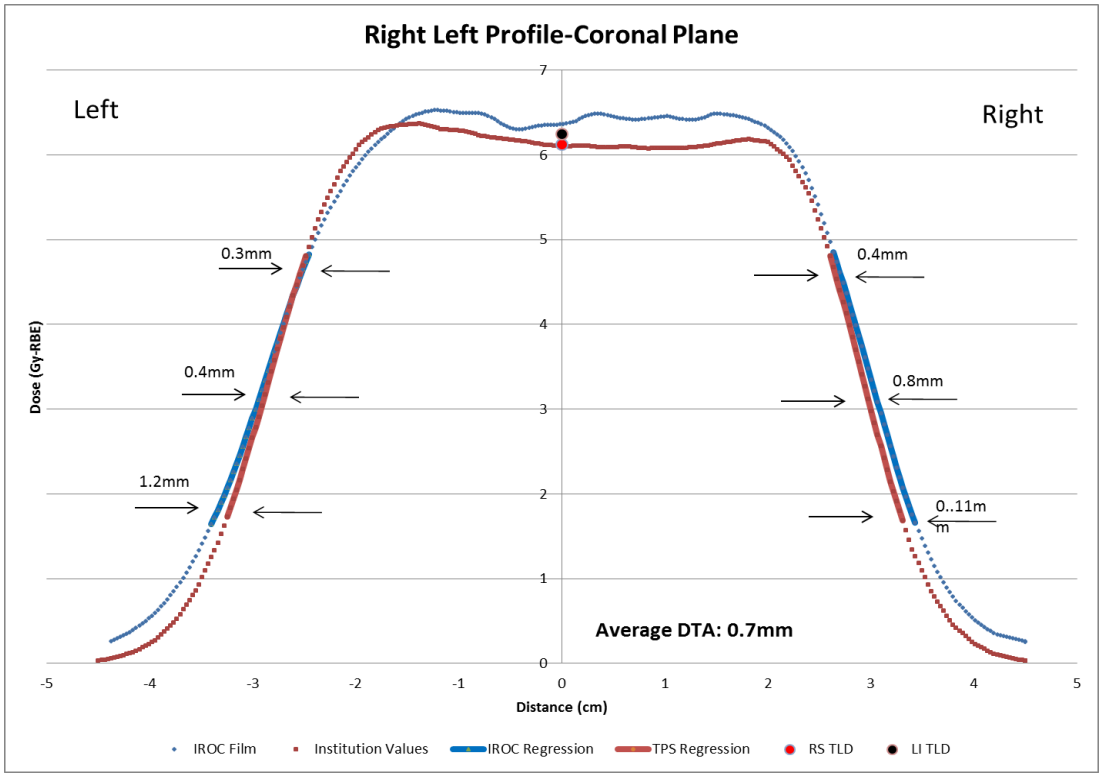

Figure 5.20 R-L Dose Profile for the passive scattering trial 2 lower spine field, measured in the coronal Plane

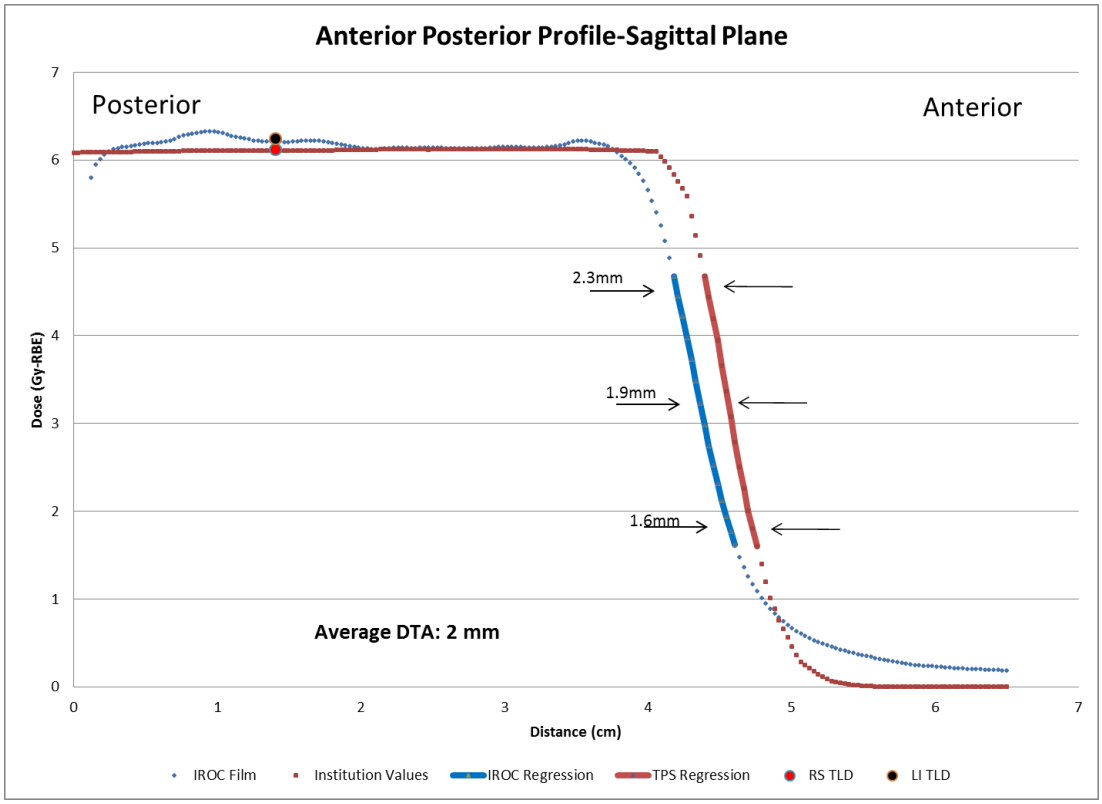

Figure 5.21 A-P Dose Profile for the passive scattering trial 2 upper spine field, measured in the Sagittal Plane

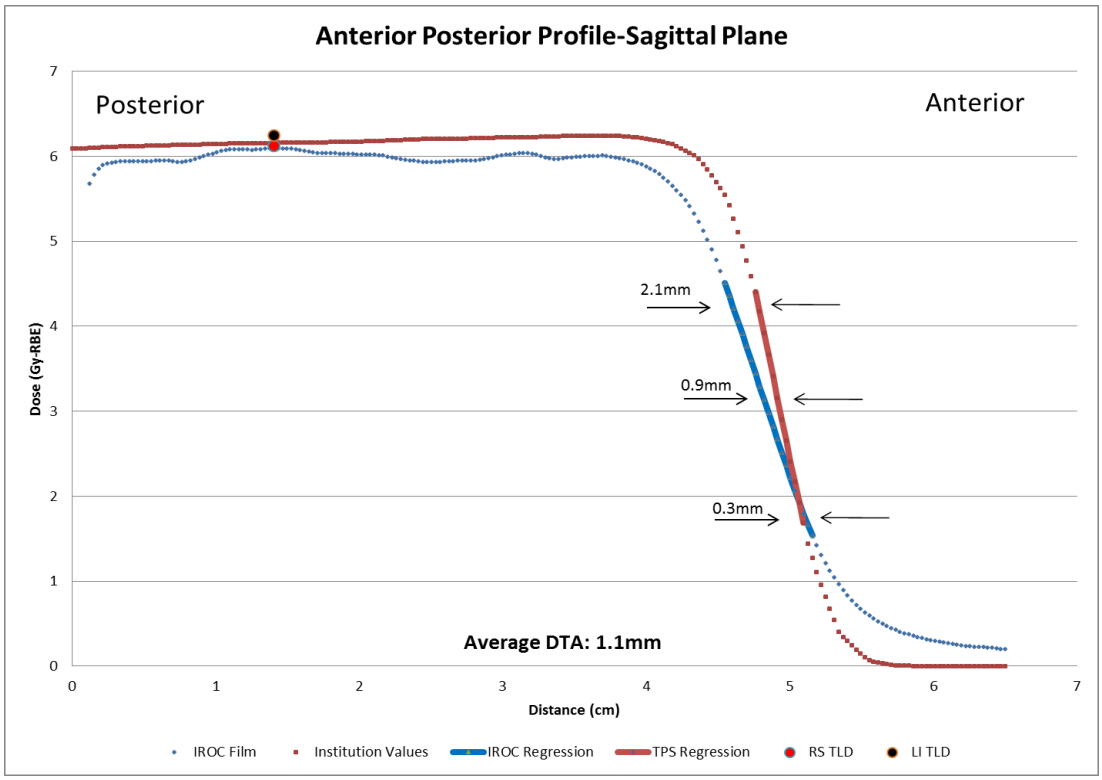

Figure 5.22 A-P Dose Profile for the passive scattering trial 2 lower spine field, measured in the sagittal Plane

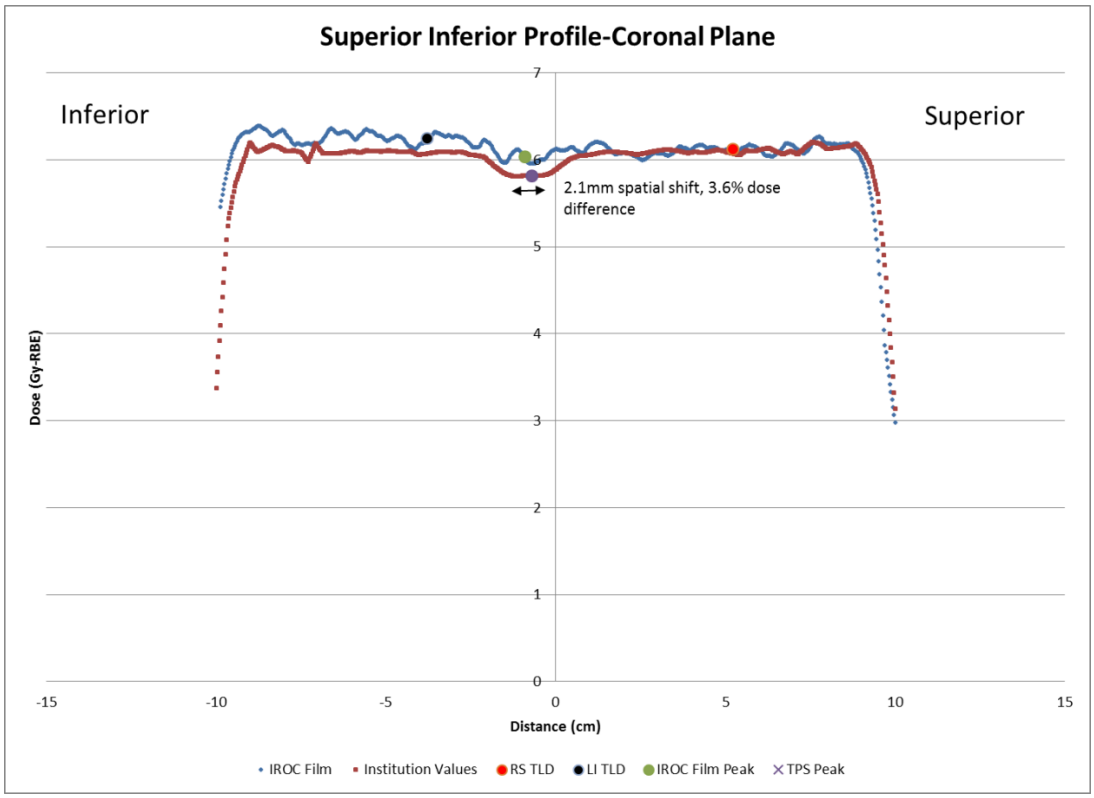

Figure 5.23 S-I Dose Profile for the passive scattering trial 2, measured in the coronal Plane

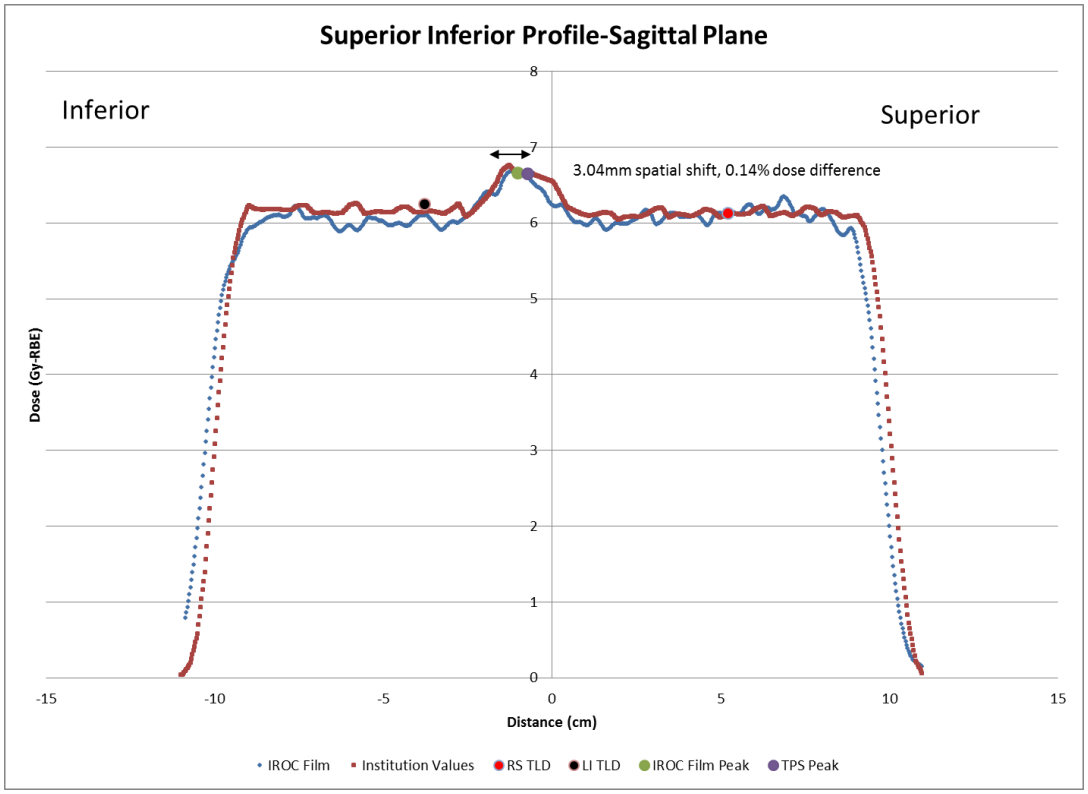

Figure 5.24 S-I Dose Profile for the passive scattering trial 2, measured in the sagittal Plane

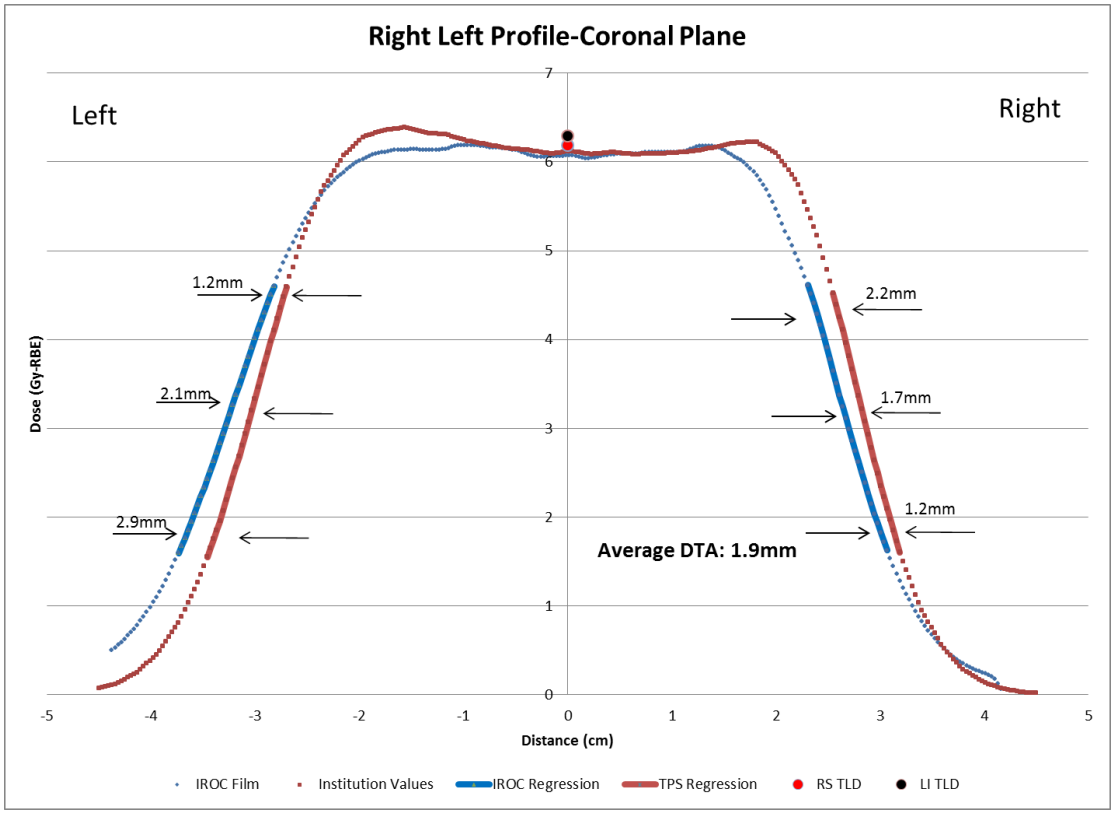

Figure 5.25 R-L Dose Profile for the passive scattering trial 3 upper spine field, measured in the coronal Plane

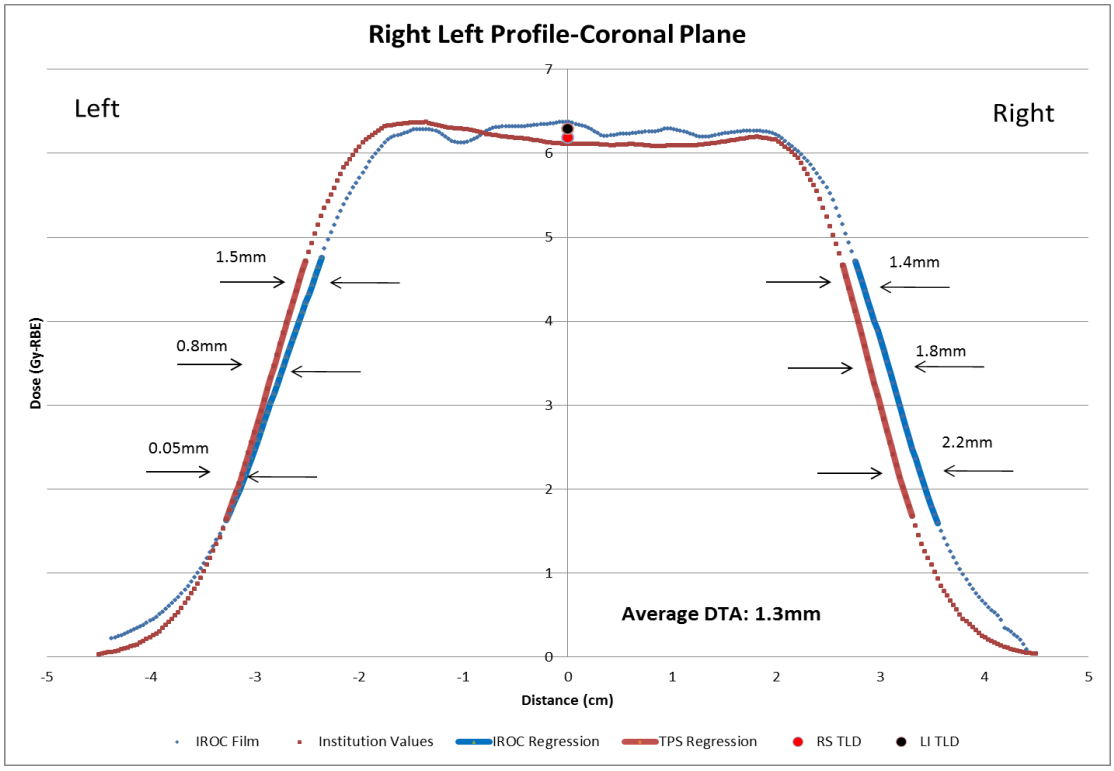

Figure 5.26 R-L Dose Profile for the passive scattering trial 3 lower spine field, measured in the coronal Plane

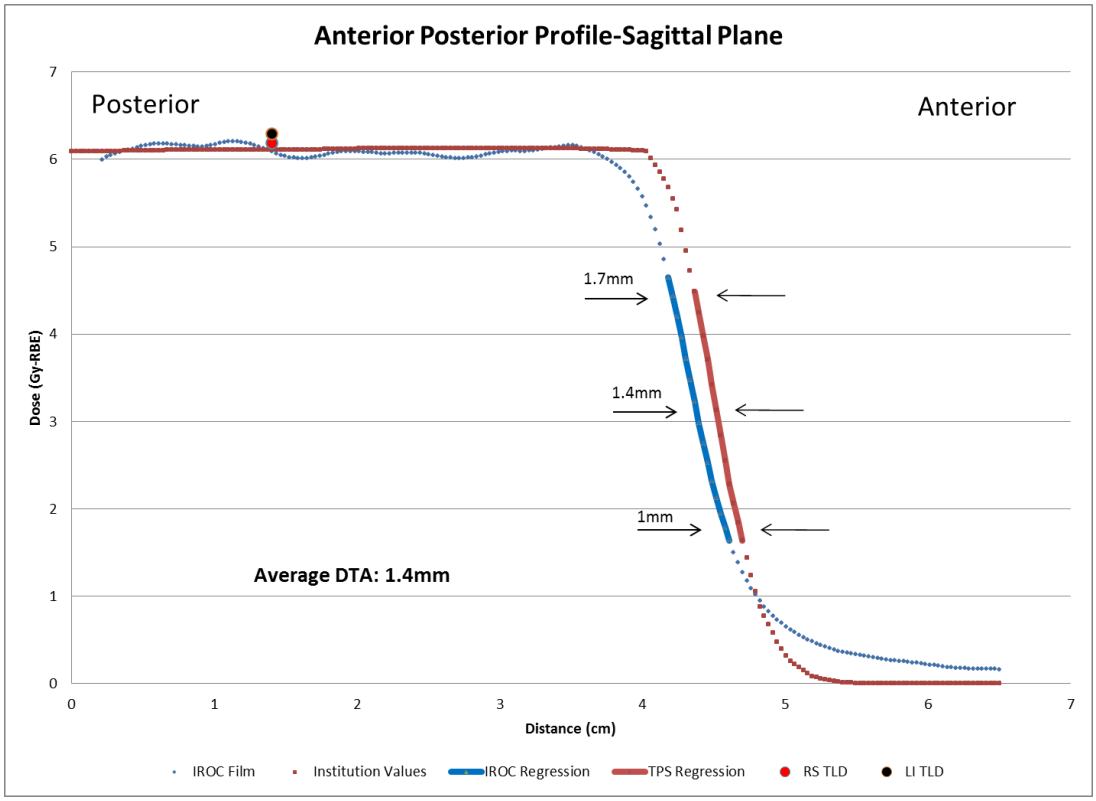

Figure 5.27 A-P Dose Profile for the passive scattering trial 3 upper spine field, measured in the Sagittal Plane

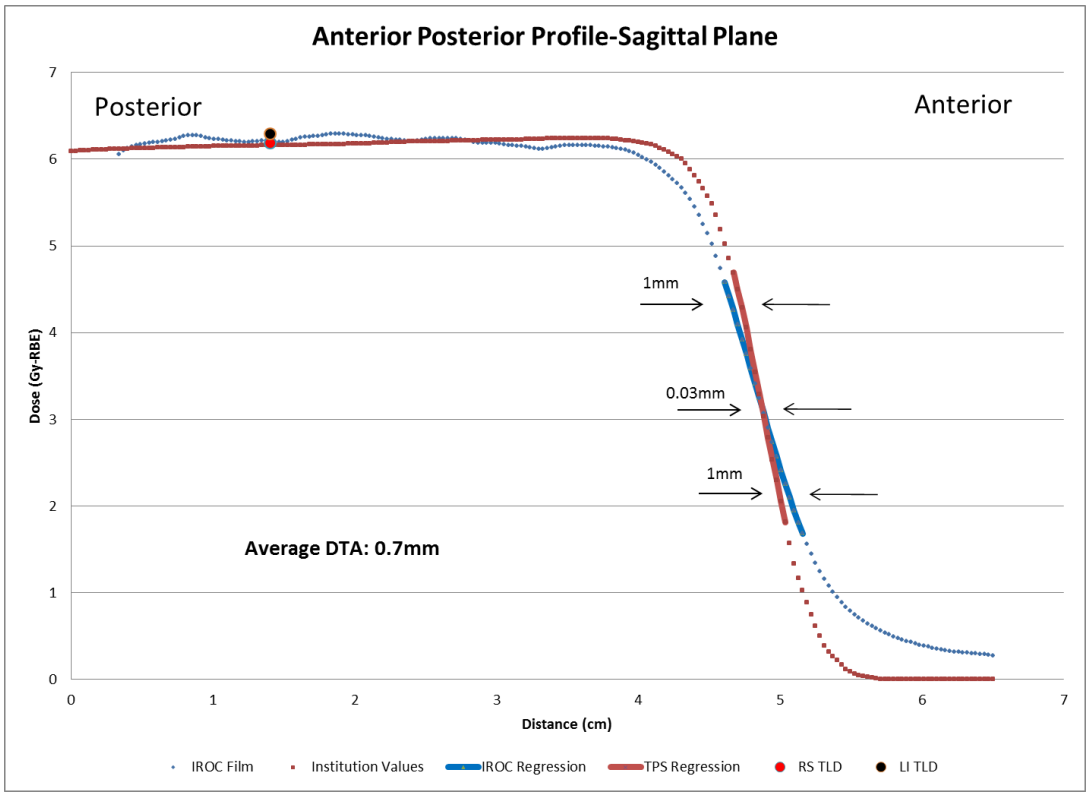

Figure 5.28 A-P Dose Profile for the passive scattering trial 3 lower spine field, measured in the sagittal Plane

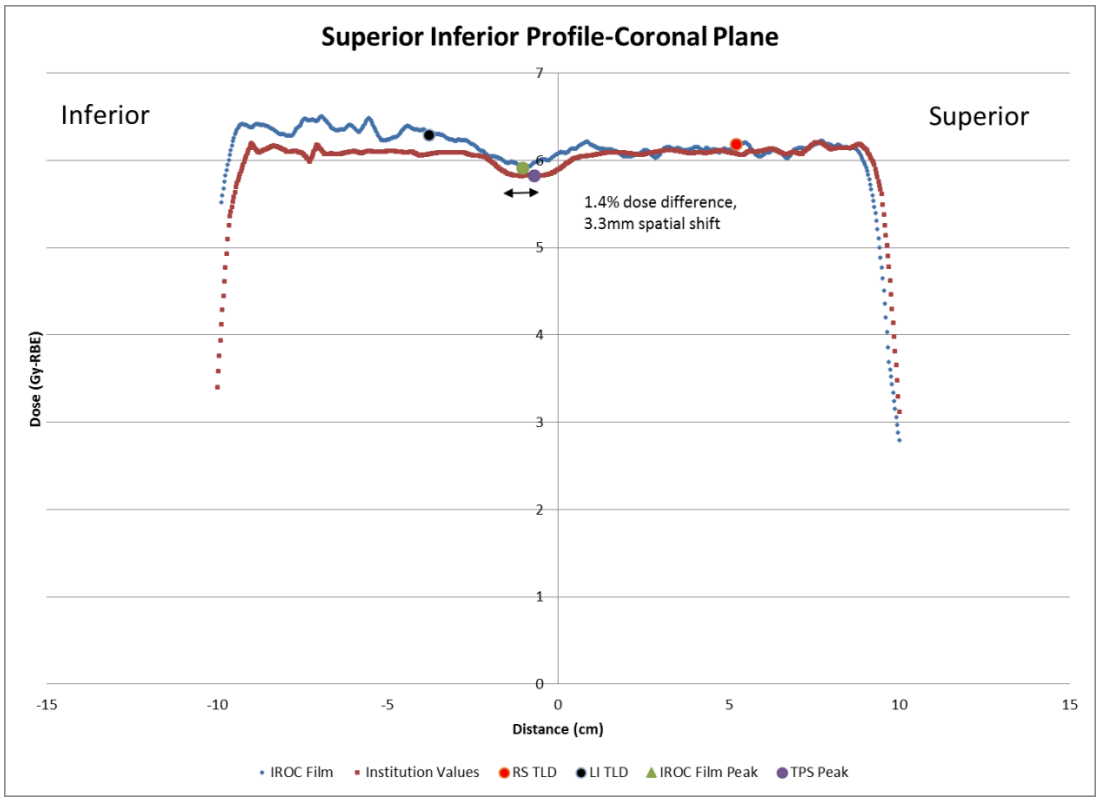

Figure 5.29 S-I Dose Profile for the passive scattering trial 3, measured in the coronal Plane

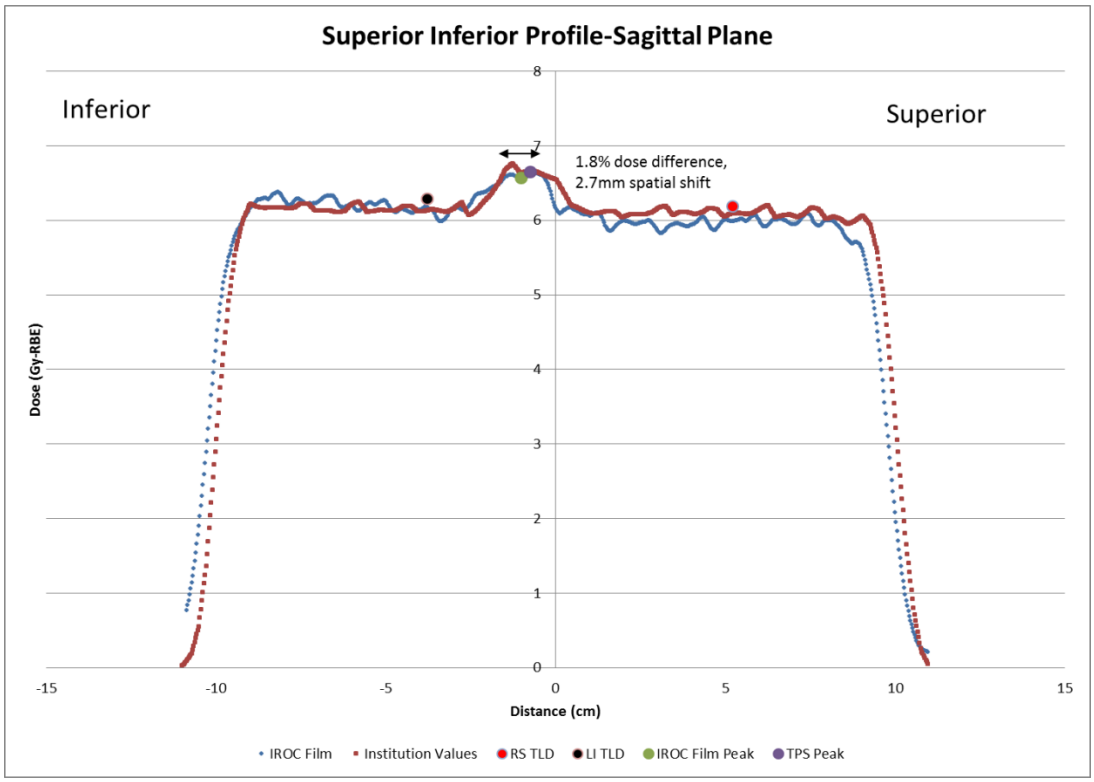

Figure 5.30 S-I Dose Profile for the passive scattering trial 3, measured in the sagittal Plane

5.2.2 Spot Scanning Trial Comparisons

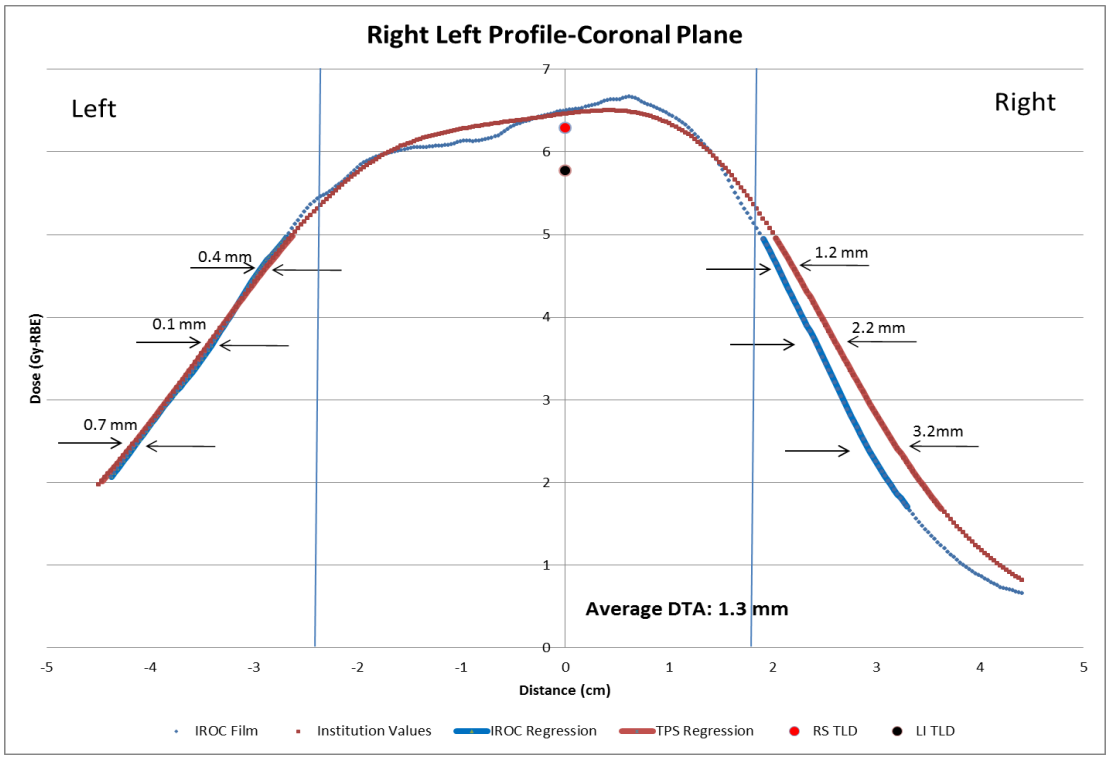

Figure 5.31 R-L Dose Profile for the Spot scanning trial 1 upper spine field, measured in the coronal Plane

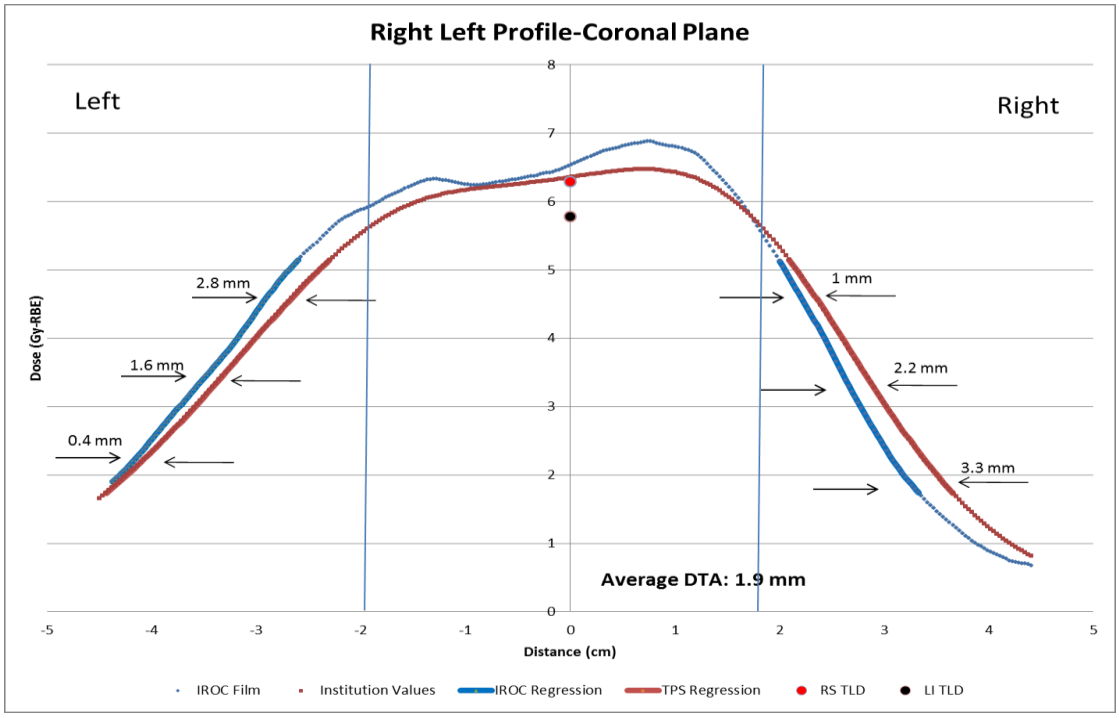

Figure 5.32 R-L Dose Profile for the Spot scanning trial 1 lower spine field, measured in the coronal Plane

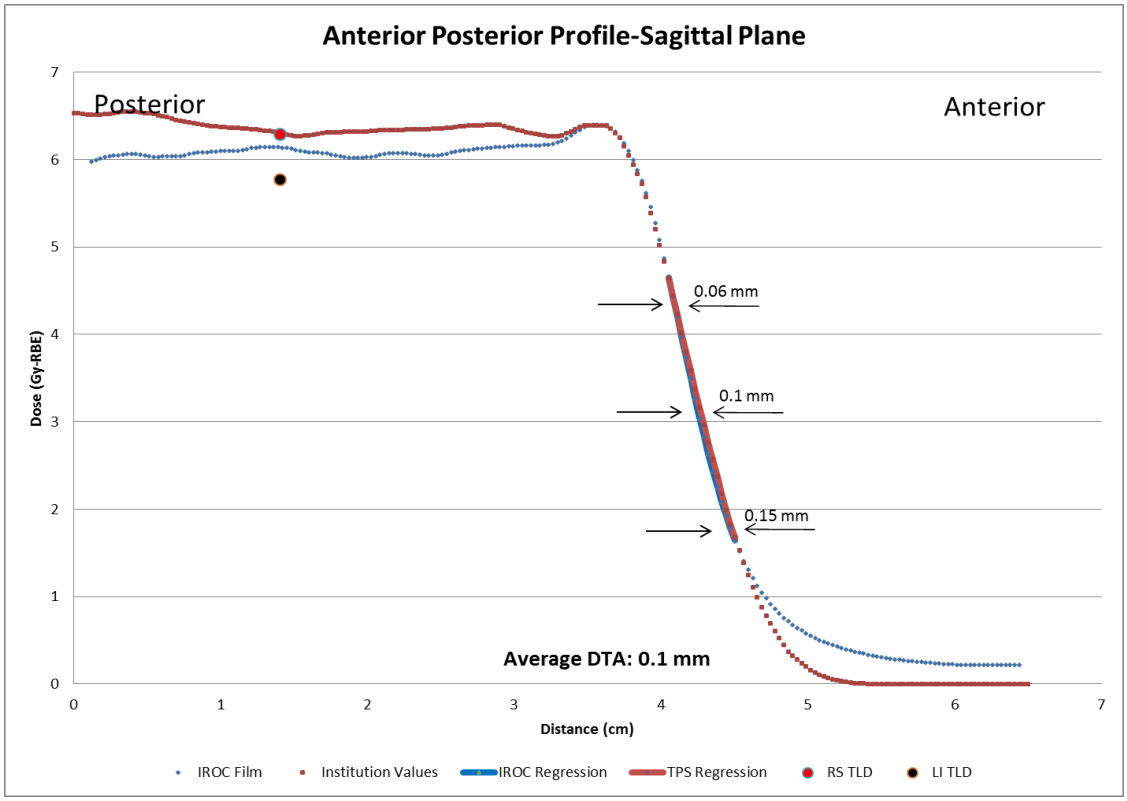

Figure 5.33 A-P Dose Profile for the Spot scanning trial 1 upper spine field, measured in the Sagittal Plane

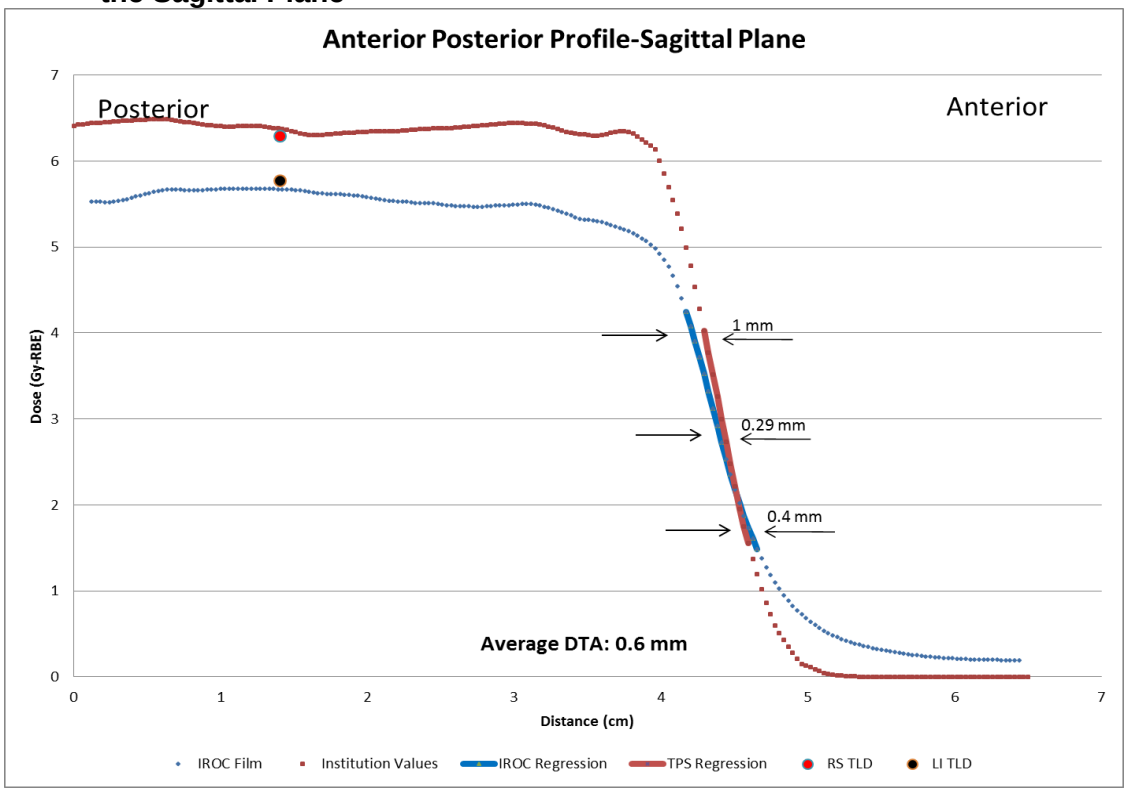

Figure 5.34 A-P Dose Profile for the Spot scanning trial 1 lower spine field, measured in the sagittal Plane

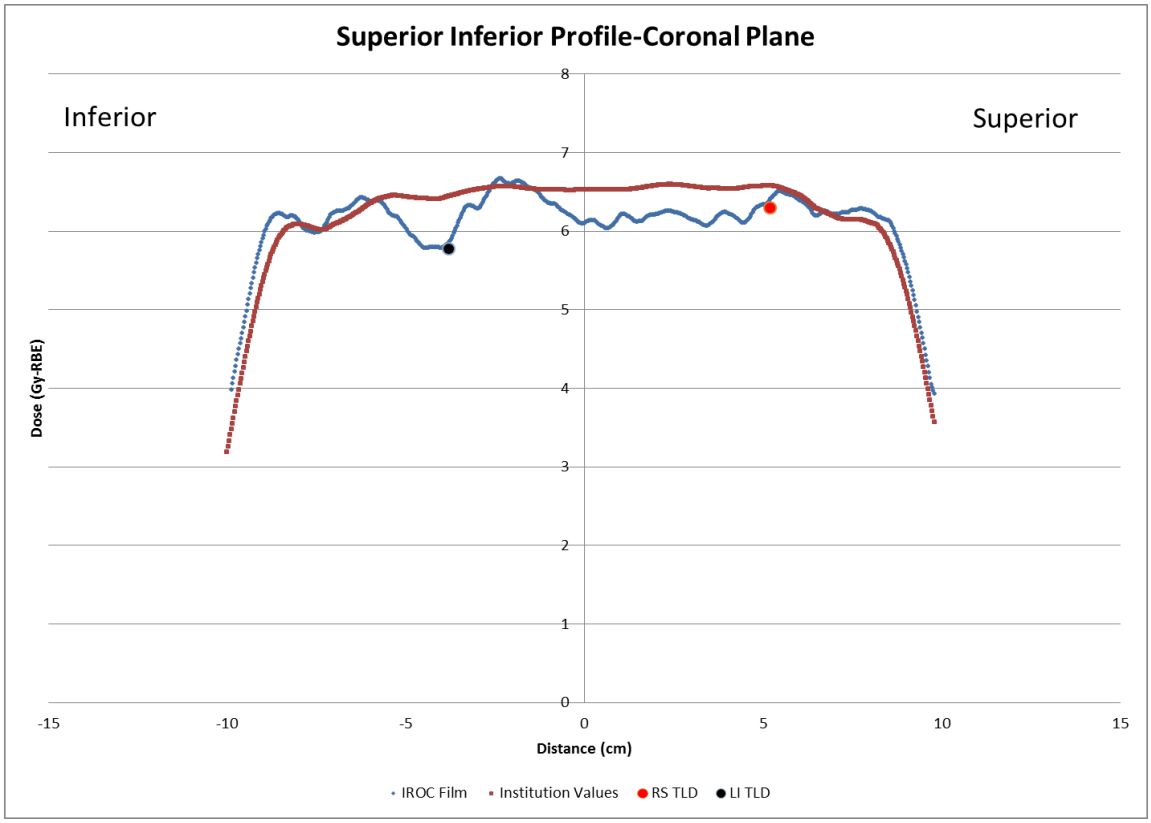

Figure 5.35 S-I Dose Profile for the Spot scanning trial 1, measured in the coronal Plane

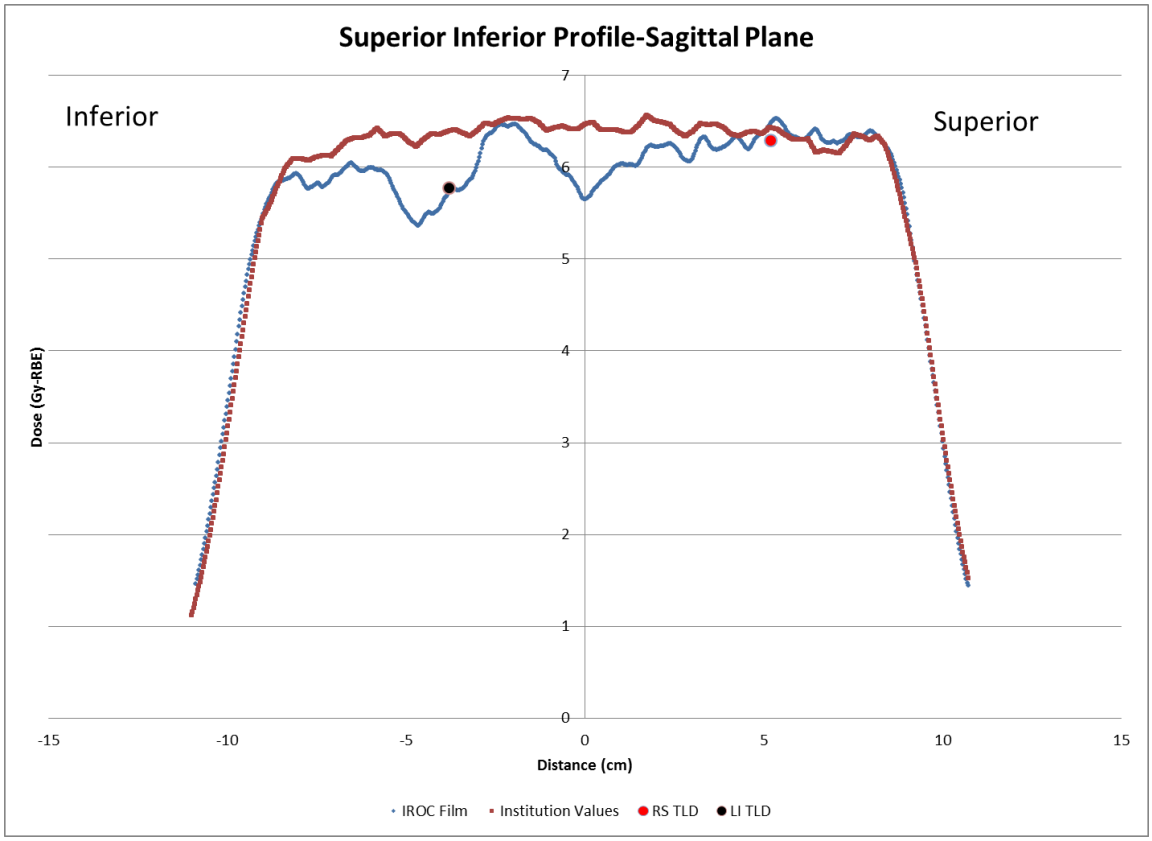

Figure 5.36 S-I Dose Profile for the Spot scanning trial 1, measured in the sagittal Plane

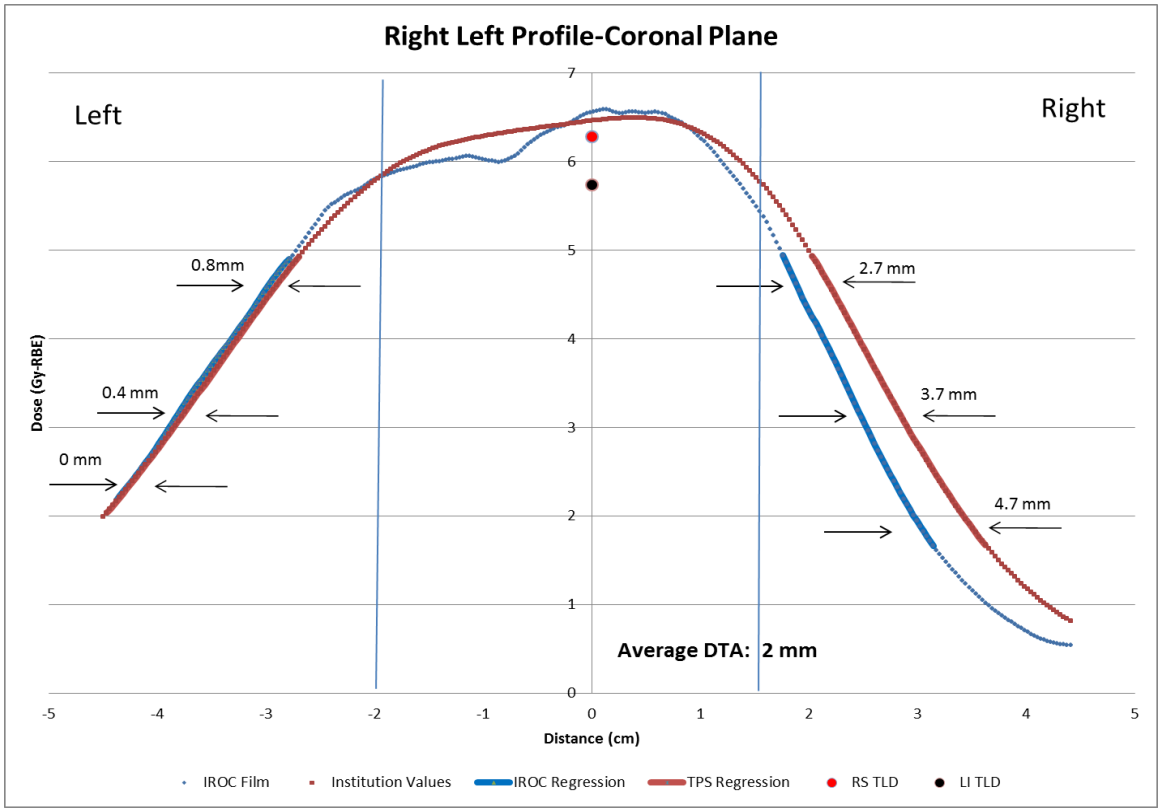

Figure 5.37 R-L Dose Profile for the Spot scanning trial 2 upper spine field, measured in the coronal Plane

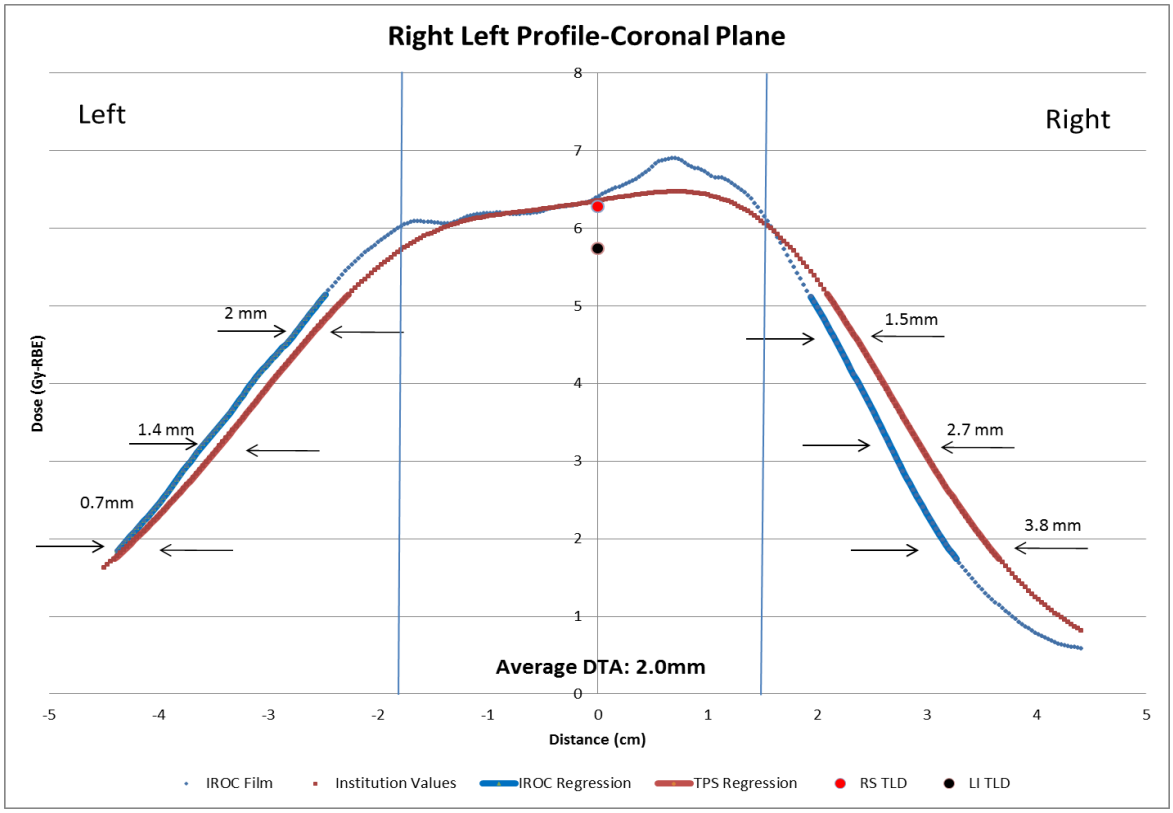

Figure 5.38 R-L Dose Profile for the Spot scanning trial 2 lower spine field, measured in the coronal Plane

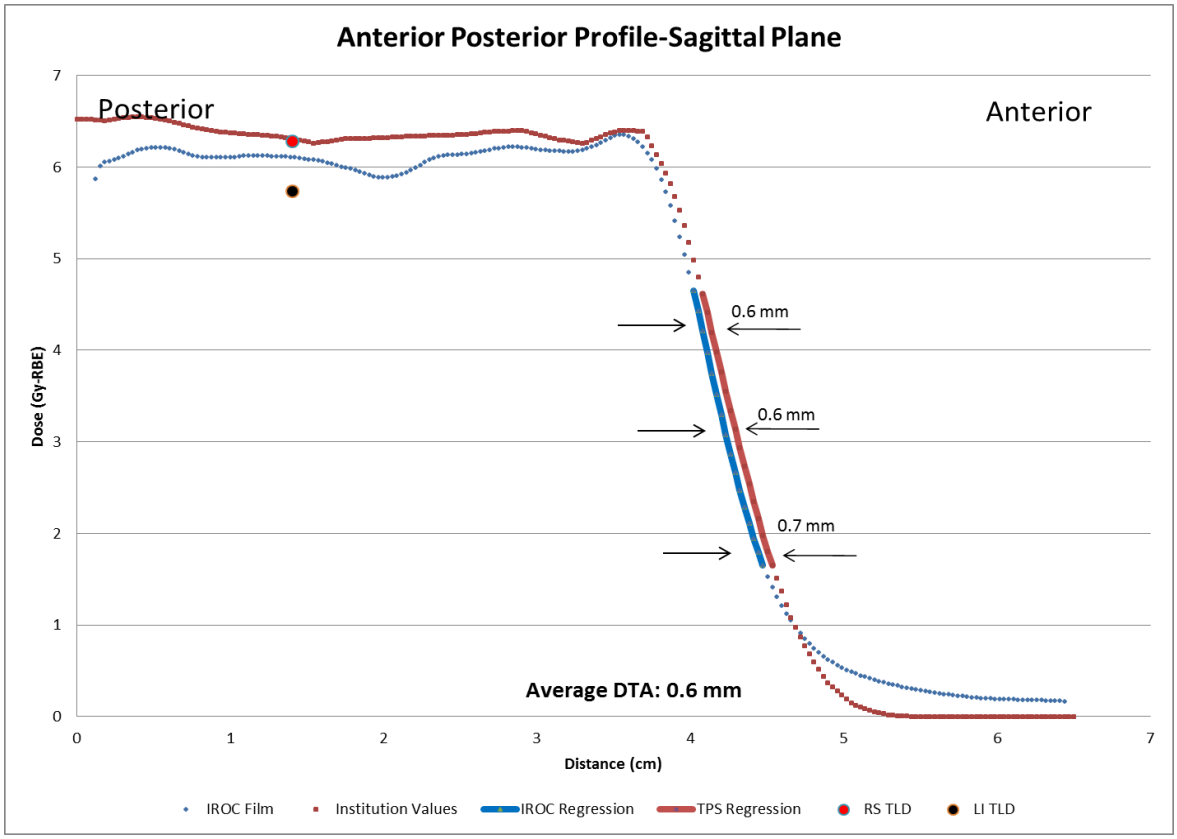

Figure 5.39 A-P Dose Profile for the Spot scanning trial 2 upper spine field, measured in the Sagittal Plane

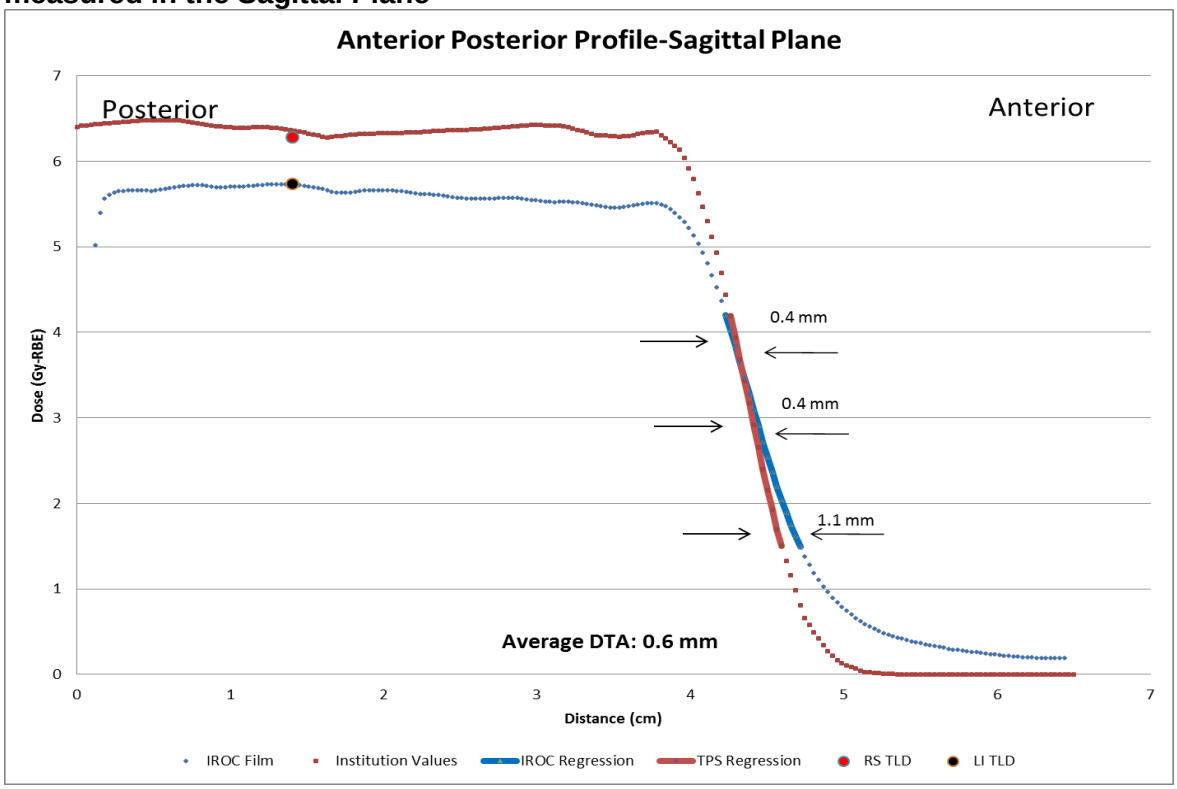

Figure 5.40 A-P Dose Profile for the Spot scanning trial 2 lower spine field, measured in the sagittal Plane

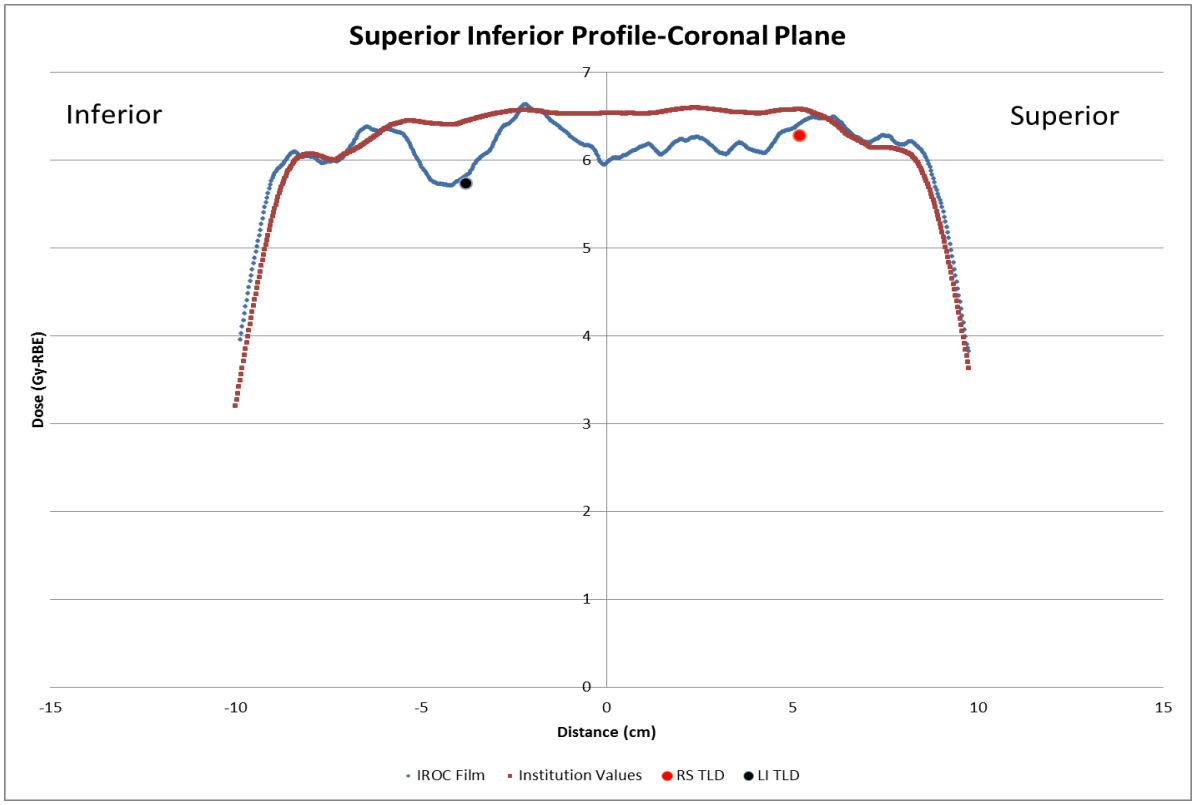

Figure 5.41 S-I Dose Profile for the Spot scanning trial 2, measured in the coronal Plane

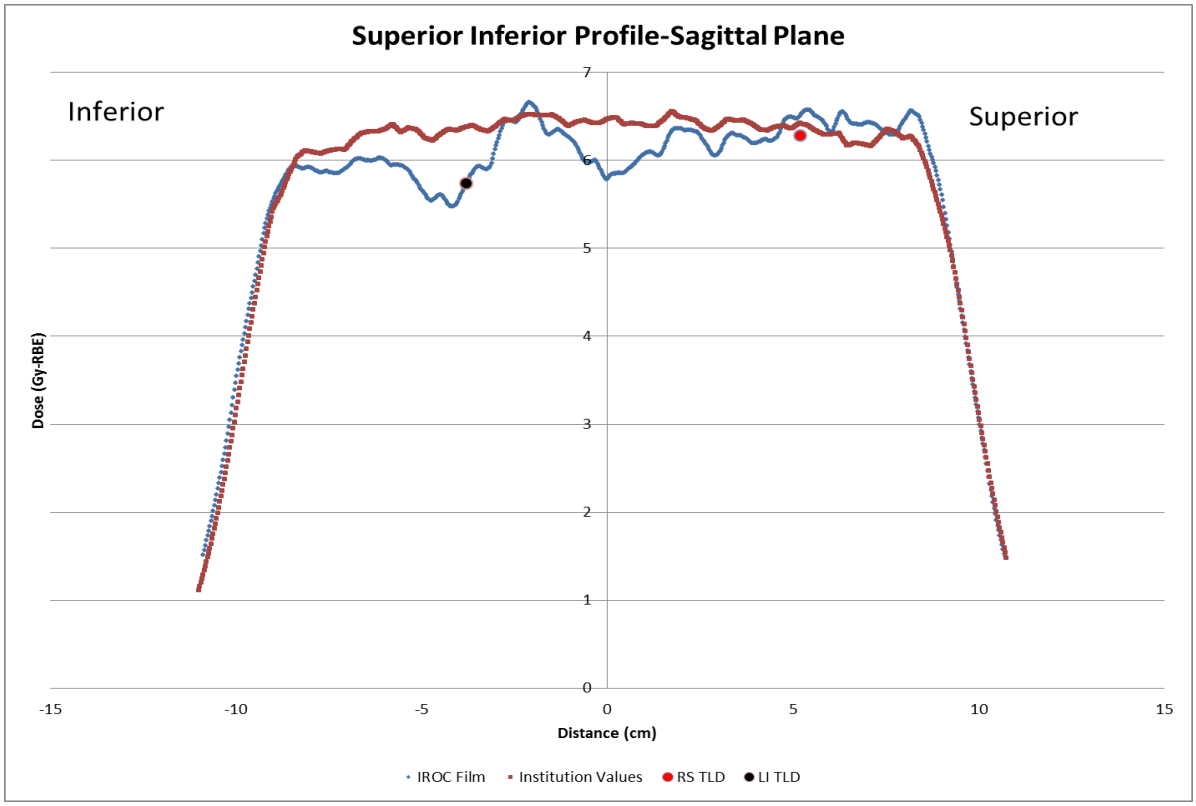

Figure 5.42 S-I Dose Profile for the Spot scanning trial 2, measured in the sagittal Plane

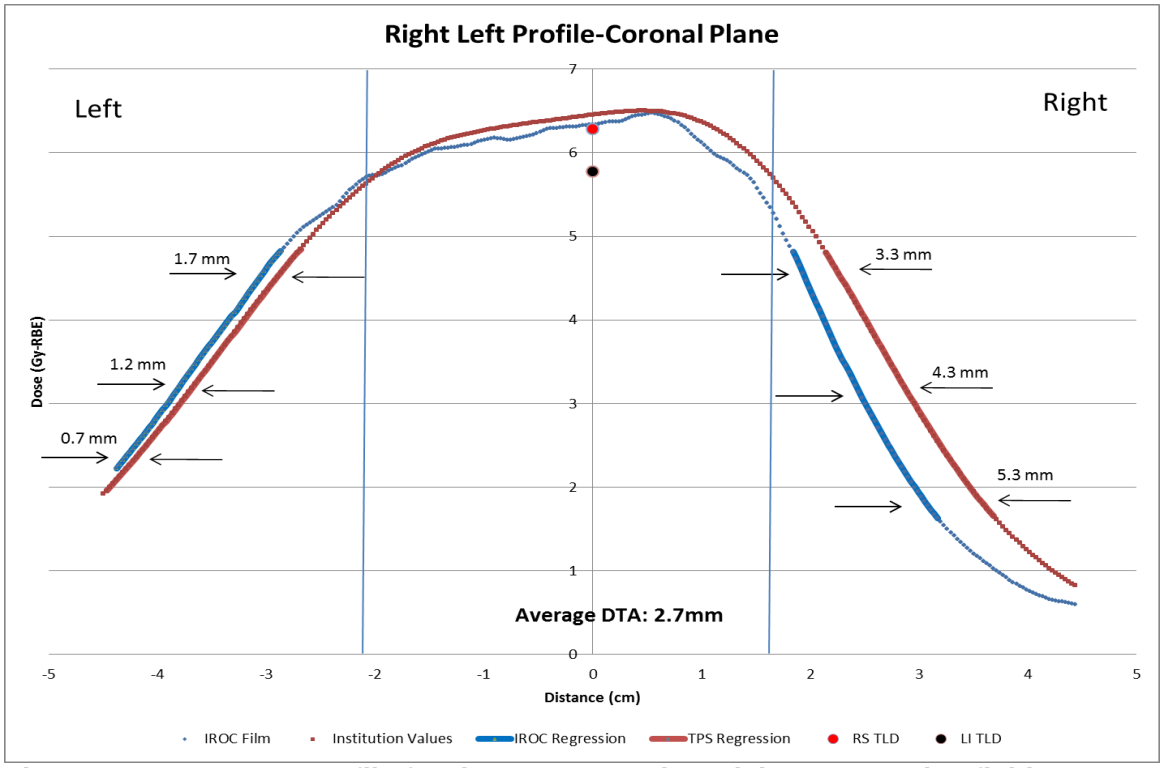

Figure 5.43 R-L Dose Profile for the Spot scanning trial 3 upper spine field, measured in the coronal Plane

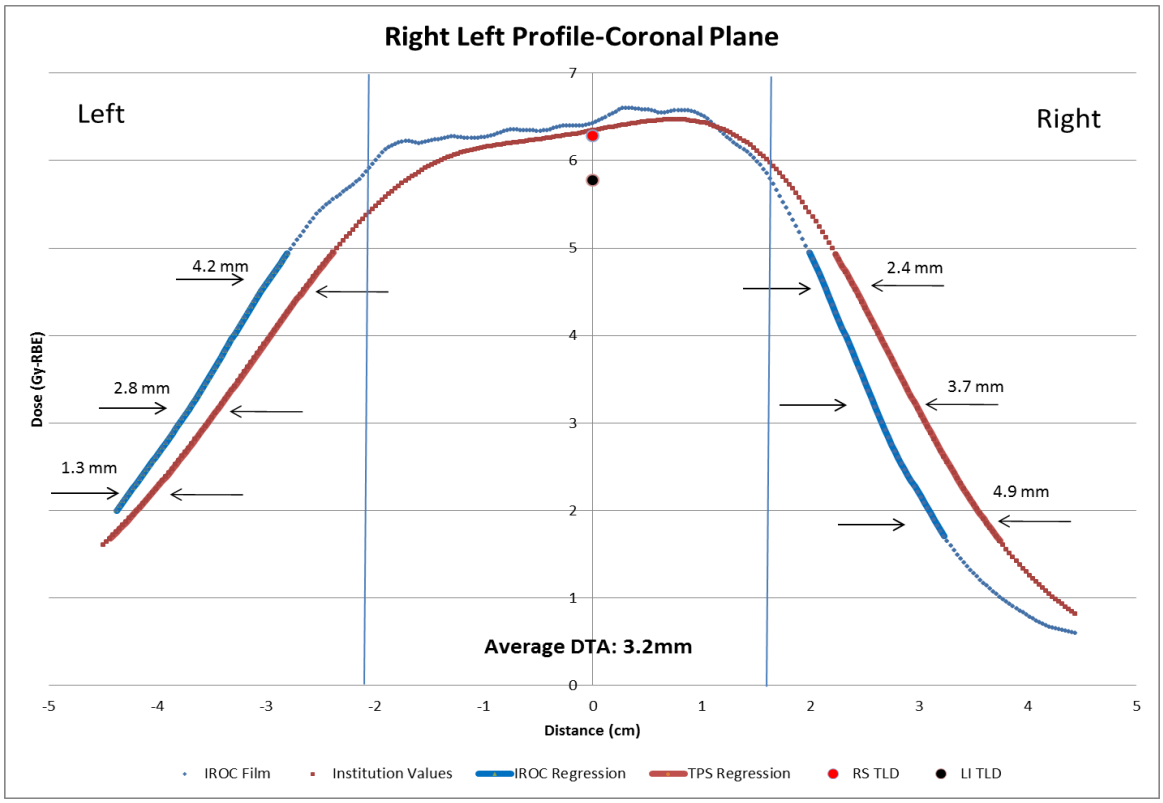

Figure 5.44 R-L Dose Profile for the Spot scanning trial 3 lower spine field, measured in the coronal Plane

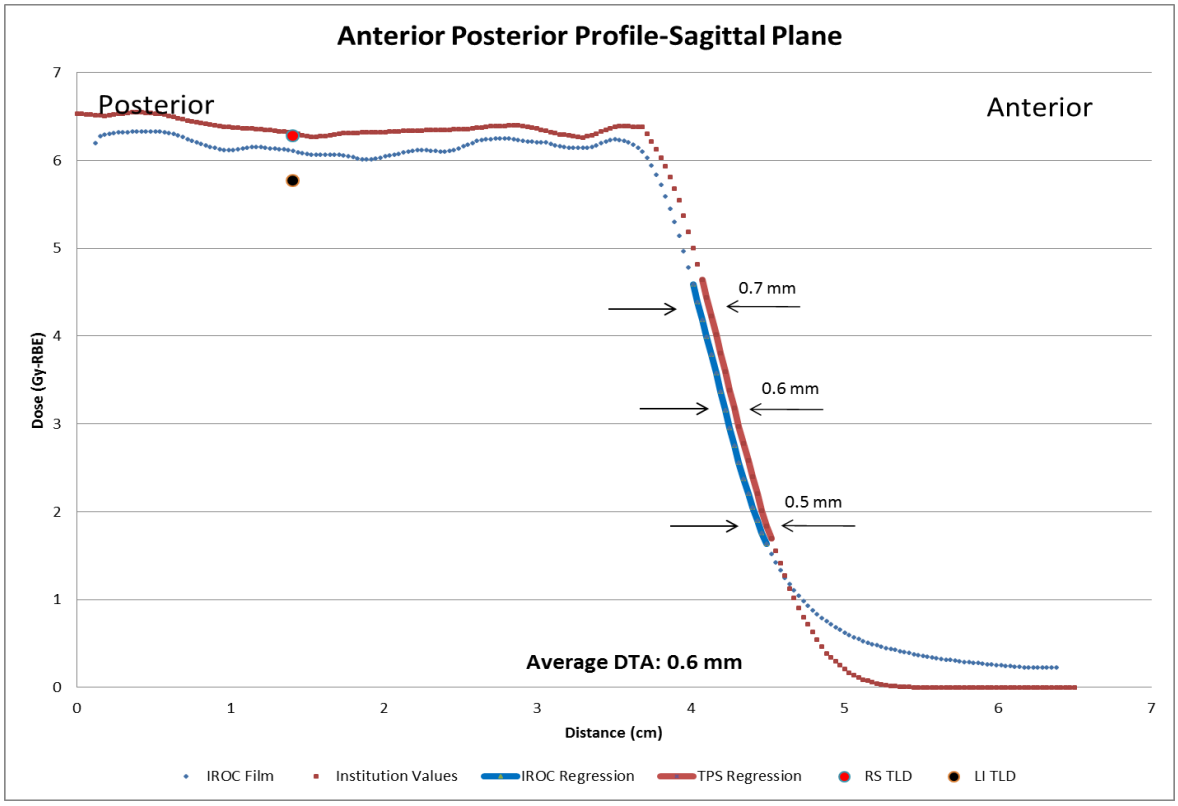

Figure 5.45 A-P Dose Profile for the Spot scanning trial 3 upper spine field, measured in the Sagittal Plane

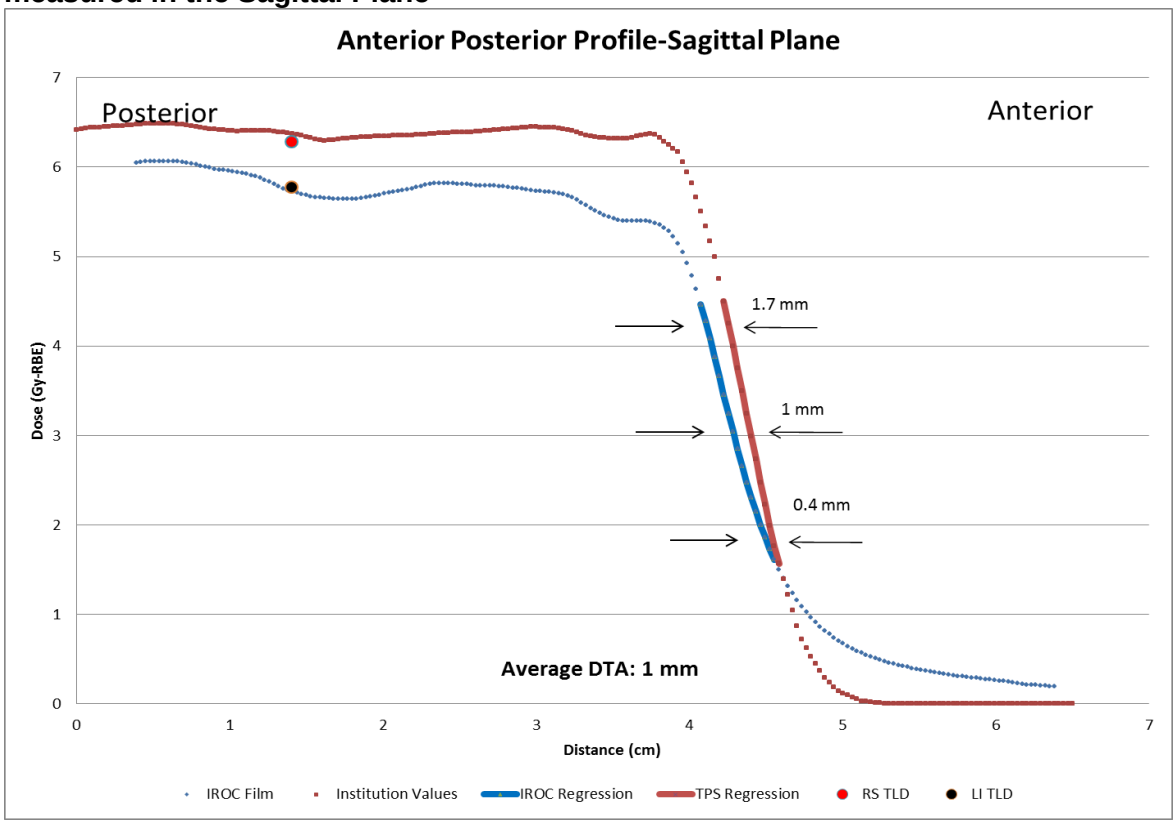

Figure 5.46 A-P Dose Profile for the Spot scanning trial 3 lower spine field, measured in the sagittal Plane

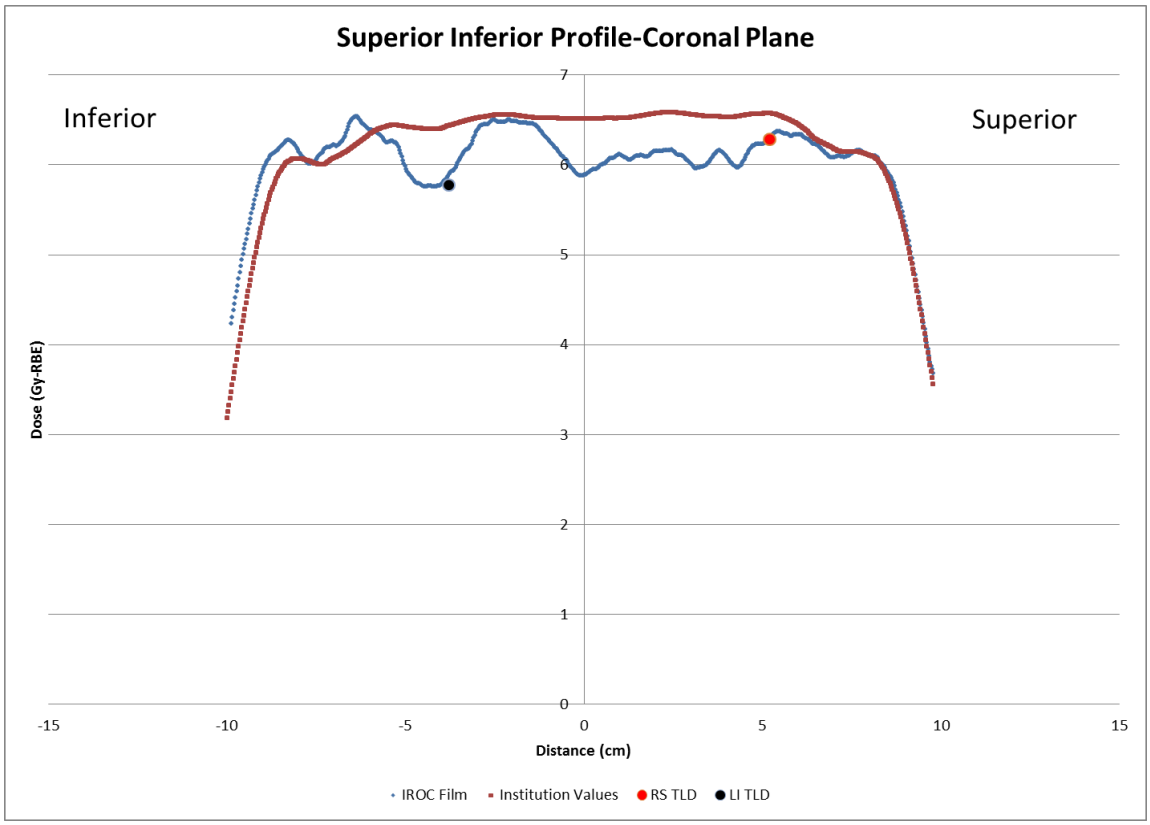

Figure 5.47 S-I Dose Profile for the Spot scanning trial 3, measured in the coronal Plane

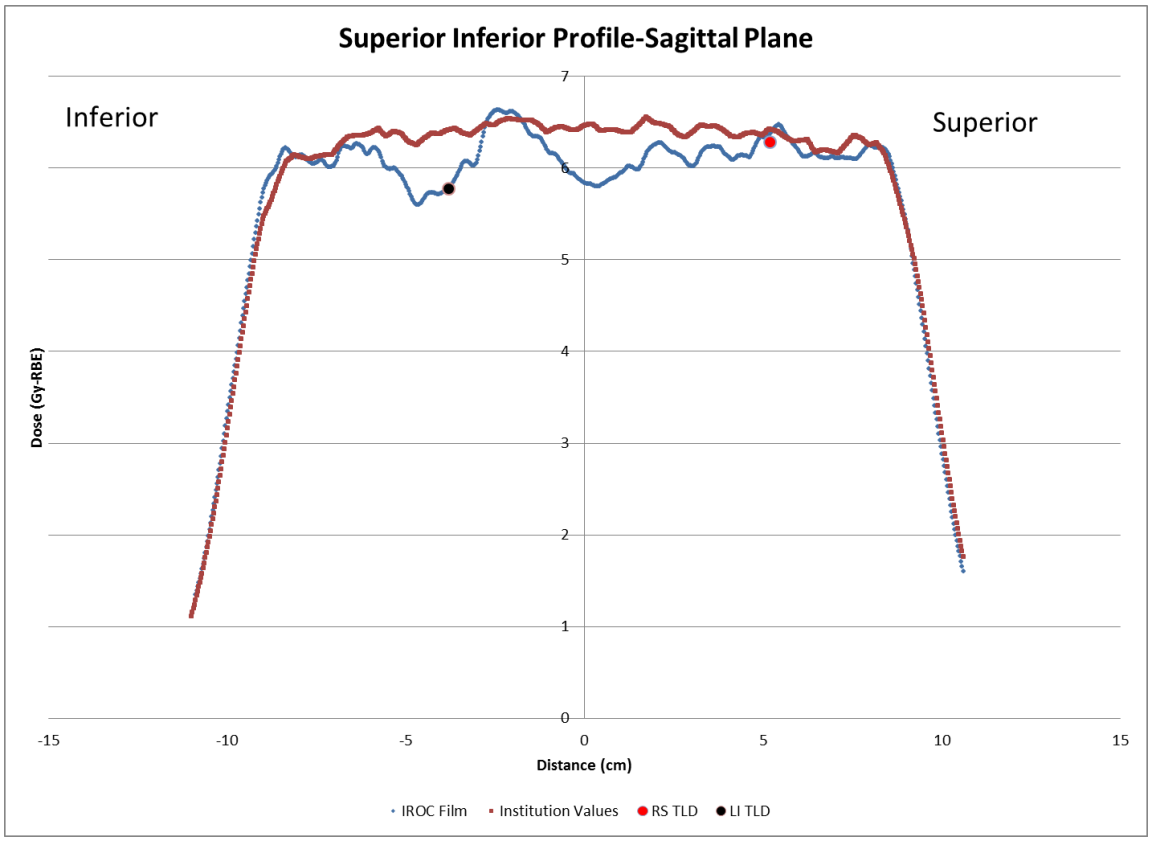

Figure 5.48 S-I Dose Profile for the Spot scanning trial 3, measured in the sagittal Plane

6 References

1. ICRU, "9 QUALITY ASSURANCE," JOURNAL OF THE ICRU, 135-139 (2007).
2. T. Pawlicki, A.J. Mundt, Quality and safety in radiotherapy. (CRC Press/Taylor & Francis, Boca Raton, 2011).
3. IROC, "Imaging and Radiation Oncology Core-IROC Website," (IROC, editor, Houston, TX, 2014).
4. D.S. Followill, D.R. Evans, C. Cherry, A. Molineu, G. Fisher, W.F. Hanson, G.S. Lbbott, "Design, development, and implementation of the Radiological Physics Center's pelvis and thorax anthropomorphic quality assurance phantoms," Medical physics 34, 2070-2076 (2007).
5. A. Molineu, D.S. Followill, P.A. Balter, W.F. Hanson, M.T. Gillin, M.S. Huq, A. Eisbruch, G.S. Ibbott, "Design and implementation of an anthropomorphic quality assurance phantom for intensity-modulated radiation therapy for the radiation therapy oncology group," International Journal of Radiation Oncology Biology Physics 63, 577-583 (2005).
6. P. Balter, W.F. Hanson, J.A. BenComo, “The Development of A Mailable Phantom for Remote Quality Audit of Stereotactic Radiosurgery,” Medical Physics, 22:979, 1995
7. P.A. Summers, D.S. Followill, N. Sahoo, S. Tucker, F. Poenisch, B. Riley, G.S. Ibbott, "An Anthropomorphic Head Phantom for Credentialing of Institutions Participating in Proton Therapy Clinical Trials," International Journal of Radiation Oncology Biology Physics 81, S882-S882 (2011).

8. J. Neihart, N. Sahoo, P. Balter, P. Summers, M. Palmer, M. Kerr, D. Followill, "Design and Verification of a Heterogeneous Proton Equivalent Thorax Phantom for Use in End-To-End Assessment of Pencil Beam Proton Therapy," Medical physics 40, 2013).
9. NAPT, "National Association for Proton Therapy-NAPT Website," (Silver Spring, Maryland, 2014).
10. NCI, "Guidelines for the Use of Proton Radiation Therapy in NCI-Sponsored Cooperative Group Clinical Trials," (National Cancer Institute, 2012).
11. W.H. St Clair, J.A. Adams, M. Bues, B.C. Fullerton, S. La Shell, H.M. Kooy, J.S. Loeffler, N.J. Tarbell, "Advantage of protons compared to conventional X-ray or IMRT in the treatment of a pediatric patient with medulloblastoma," International journal of radiation oncology, biology, physics 58, 727-734 (2004).
12. M. Yoon, D.H. Shin, J. Kim, J.W. Kim, D.W. Kim, S.Y. Park, S.B. Lee, J.Y. Kim, H.J. Park, B.K. Park, S.H. Shin, "Craniospinal irradiation techniques: a dosimetric comparison of proton beams with standard and advanced photon radiotherapy," International journal of radiation oncology, biology, physics 81, 637-646 (2011).
13. AAPM Radiation Therapy Committee. Task Group 24., AAPM Radiation Therapy Committee. Task Group 22., Physical aspects of quality assurance in radiation therapy. (Published for the American Association of Physicists in Medicine by the American Institute of Physics, New York, NY, 1984).
14. W. Bogdanich, "As Technology Surges, Radiation Safeguards Lag," in The New York Times (The New York Times, New York, NY., 2010).
15. R.R. Wilson, "Radiological use of fast protons," Radiology 47, 487-491 (1946).

16. ICRU, "1 INTRODUCTION," JOURNAL OF THE ICRU, 11-20 (2007).

17. H. Paganetti, Proton therapy physics. (Taylor & Francis, Boca Raton, 2012).

18. ICRU, "3 BEAM DELIVERY AND PROPERTIES," JOURNAL OF THE ICRU, 29-48 (2007).

19. ICRU, "2 RADIATION BIOLOGY CONSIDERATIONS," JOURNAL OF THE ICRU, 21-28 (2007).

20. ICRU, "8 ESTIMATION AND PRESENTATION OF UNCERTAINTY IN THE DELIVERED DOSE," JOURNAL OF THE ICRU, 131-134 (2007).

21. H. Paganetti, "Range uncertainties in proton therapy and the role of Monte Carlo simulations," Physics in medicine and biology 57, R99-R117 (2012).

22. A. Smith, M. Gillin, M. Bues, X.R. Zhu, K. Suzuki, R. Mohan, S. Woo, A. Lee, R. Komaki, J. Cox, K. Hiramoto, H. Akiyama, T. Ishida, T. Sasaki, K. Matsuda, "The M. D. Anderson proton therapy system," Medical physics 36, 4068-4083 (2009).

23. P.A. Johnstone, K.P. McMullen, J.C. Buchsbaum, J.G. Douglas, P. Helft, "Pediatric CSI: are protons the only ethical approach?," International journal of radiation oncology, biology, physics 87, 228-230 (2013).

24. R.M. Howell, A. Giebeler, W. Koontz-Raisig, A. Mahajan, C.J. Etzel, A.M. D'Amelio, Jr., K.L. Homann, W.D. Newhauser, "Comparison of therapeutic dosimetric data from passively scattered proton and photon craniospinal irradiations for medulloblastoma," Radiation oncology 7, 116 (2012).

25. S.L. Wolden, "Protons for craniospinal radiation: are clinical data important?," International journal of radiation oncology, biology, physics 87, 231-232 (2013).

26. Cho, J., P.A. Summers, and G.S. Ibbott, An anthropomorphic spine phantom for proton beam approval in NCI-funded trials. J Appl Clin Med Phys, 2014. 15(3): p. 4742.

27. R.L. Grant, P.A. Summers, J.L. Neihart, A.P. Blatnica, N. Sahoo, M.T. Gillin, D.S. Followill, G.S. Ibbott, "Relative stopping power measurements to aid in the design of anthropomorphic phantoms for proton radiotherapy," Journal of applied clinical medical physics / American College of Medical Physics 15, 4523 (2014)

28. NIST, "National Institute of Standards and Technology-NIST Website," (2014).

29. U. Schneider, E. Pedroni, A. Lomax, "The calibration of CT Hounsfield units for radiotherapy treatment planning," Physics in medicine and biology 41, 111-124 (1996).

30. B. Schaffner, E. Pedroni, "The precision of proton range calculations in proton radiotherapy treatment planning: experimental verification of the relation between CT-HU and proton stopping power," Physics in medicine and biology 43, 1579-1592 (1998).

31. M.F. Moyers, M. Sardesai, S. Sun, D.W. Miller, "Ion Stopping Powers and Ct Numbers," Medical Dosimetry 35, 179-194 (2010).

32. ICRU, "5 GEOMETRIC TERMS, AND DOSE AND DOSE-VOLUME DEFINITIONS," JOURNAL OF THE ICRU, 83-94 (2007).

33. R.M. Howell, A. Giebeler, W. Koontz-Raisig, A. Mahajan, C.J. Etzel, A.M. D'Amelio, Jr., K.L. Homann, W.D. Newhauser, "Comparison of therapeutic dosimetric data from passively scattered proton and photon craniospinal irradiations for medulloblastoma," Radiation oncology 7, 116 (2012).

34. G.F. Knoll, Radiation detection and measurement, 4th ed. (John Wiley, Hoboken, N.J., 2010).

35. J.R. Zullo, R.J. Kudchadker, X.R. Zhu, N. Sahoo, M.T. Gillin, "LiF TLD-100 as a dosimeter in high energy proton beam therapy--can it yield accurate results?," Medical dosimetry : official journal of the American Association of Medical Dosimetrists 35, 63-66 (2010).

36. J.F.Aguirre, R.Tailor, G. Ibbott, M. Stovall, W. Hanson, "Thermoluminescence dosimetry as a tool for the remote verification of output for radiotherapy beams: 25 years of experience," Proceedings of the International Symposium on Standards and Codes of Practice in Medical Radiation Dosimetry IAEA-CN-96/822002).

37. J. Kim, M. Yoon, S. Kim, D. Shin, S.B. Lee, Y.K. Lim, D.W. Kim, S.Y. Park, "Three-dimensional radiochromic film dosimetry of proton clinical beams using a gafchromic EBT2 film array," Radiation protection dosimetry 151, 272-277 (2012).

38. “GAFCHROMIC® EBT2 Self Developing Film for Radiotherapy Dosimetry”, Revision 1, International Specialty Products, Wayne, NJ, February 19, 2009.

39. B. Arjomandy, R. Tailor, A. Anand, N. Sahoo, M. Gillin, K. Prado, M. Vicic, "Energy dependence and dose response of Gafchromic EBT2 film over a wide range of photon, electron, and proton beam energies," Medical physics 37, 1942-1947 (2010).

40. P. Summers, "The Development and Implementation of an Anthropomorphic Head Phantom for the Assessment of Proton Therapy Treatment Procedures" (2011). UT GSBS Dissertations and Theses (Open Access). Paper 177.

41. D.A. Low, W.B. Harms, S. Mutic, J.A. Purdy, "A technique for the quantitative evaluation of dose distributions," Medical physics 25, 656-661 (1998).

42. L. Zhao, I.J. Das, "Gafchromic EBT film dosimetry in proton beams," Physics in medicine and biology 55, N291-301 (2010).

43. S.M. Vatnitsky, "Radiochromic film dosimetry for clinical proton beams," Applied radiation and isotopes: including data, instrumentation and methods for use in agriculture, industry and medicine 48, 643-651 (1997).

44. D. Kirby, S. Green, H. Palmans, R. Hugtenburg, C. Wojnecki, D. Parker, "LET dependence of GafChromic films and an ion chamber in low-energy proton dosimetry," Physics in medicine and biology 55, 417-433 (2010).

45. H. Paganetti, "Nuclear interactions in proton therapy: dose and relative biological effect distributions originating from primary and secondary particles," Physics in medicine and biology 47, 747-764 (2002).

46. W. Liu, X.D. Zhang, Y.P. Li, R. Mohan, "Robust optimization of intensity modulated proton therapy," Medical physics 39, 1079-1091 (2012).

47. X.R. Zhu, F. Poenisch, M. Lii, G.O. Sawakuchi, U. Titt, M. Bues, X. Song, X. Zhang, Y. Li, G. Ciangaru, H. Li, M.B. Taylor, K. Suzuki, R. Mohan, M.T. Gillin, N. Sahoo, "Commissioning dose computation models for spot scanning proton beams in water for a commercially available treatment planning system," Medical physics 40, 041723 (2013).

48. T. Yamashita, T. Akagi, T. Aso, A. Kimura, T. Sasaki, "Effect of inhomogeneity in a patient's body on the accuracy of the pencil beam algorithm in comparison to Monte Carlo," Physics in medicine and biology 57, 7673-7688 (2012).

Vita

Dana Jannette Lewis was born in Galveston, Texas on August 31, 1990. She is the daughter of Derryl Lewis, Dorene Biagas and K. Martin Biagas. After graduating Salutatorian of Texas City High School on May 30, 2008, she began her undergraduate studies at Louisiana State University. On May 18, 2012, Dana graduated cum laude with a Bachelor of Science degree in Physics with a concentration in Medical Physics. In August of 2012, she entered The University of Texas Graduate School of Biomedical Sciences at Houston to pursue a Master of Science degree in Medical Physics. Dana currently resides in Houston, Texas.